

MODEL-AIDED FABRICATION OF FIBER-REINFORCED  
CERAMIC COMPOSITE TUBES USING FORCED-FLOW  
CHEMICAL VAPOR INFILTRATION

By

KENT JOSEPH PROBST

A DISSERTATION PRESENTED TO THE GRADUATE SCHOOL  
OF THE UNIVERSITY OF FLORIDA IN PARTIAL FULFILLMENT  
OF THE REQUIREMENTS FOR THE DEGREE OF  
DOCTOR OF PHILOSOPHY

UNIVERSITY OF FLORIDA

2000

I would first and foremost like to thank the Lord, our God, for providing me strength to conduct all activities leading to this dissertation. I am forever indebted to my parents, William and Sandra, for continual motivation and support. I would like to thank my brother, Scott, for providing helpful advice and motivation.

## ACKNOWLEDGEMENTS

I would like to thank and acknowledge the following people who have helped me through my doctoral research at Oak Ridge: Tim Anderson for giving me the opportunity to conduct the research at Oak Ridge National Laboratory; Ted Besmann for supervising my research and for supporting conference contribution; Jerry McLaughlin, Kevin Cooley, and John Henry for technical expertise; James Klett for lending me time on the kiln for preform curing; Bill Weaver and Bob Smith for help with the preform fabrication process; Tom Starr for lending me his model, GTCVI, and for the use of the permeability experimental apparatus; Hsin Wang for performing the laser-flash thermal diffusivity measurements; Bill Ellingson, Dick Koehl, and Hueng-Rae Lee for performing the X-ray scans and for reconstructing the tomographic images; Tom Geer for preparing polished composite specimens and taking the digital images; Dave Stinton and Rick Lowden for explaining the scope of my research as it related to the Department of Energy; Becky Dearien for editing parts of the dissertation and for advice on résumé preparation.

This research was supported by the United States Department of Energy, Office of Fossil Energy, Advanced Research and Technology Development Materials under contract DE-AC05-96OR22464 with Lockheed Martin Energy Research Corporation.

## TABLE OF CONTENTS

ACKNOWLEDGEMENTS.....	iii
LIST OF TABLES.....	vii
LIST OF FIGURES.....	ix
LIST OF SYMBOLS.....	xiii
ABSTRACT.....	xv
CHAPTERS	
1 INTRODUCTION.....	1
Motivation.....	2
Ceramic Composite Processing Alternatives.....	4
2 CVI BACKGROUND AND LITERATURE REVIEW.....	6
Composite Processing Techniques.....	6
CVI Modeling Efforts.....	16
Silicon Carbide.....	24
Composite Transport Properties.....	33
3 FCVI EXPERIMENTAL METHODS.....	39
Tube Preform Fabrication.....	39
Tube Preform Assembly.....	44
FCVI Apparatus.....	47
FCVI Procedure.....	50
Post-FCVI Procedure.....	53
Preform Transport Property Measurement.....	54
Tube Density Characterization.....	59
4 CVI MODELING FUNDAMENTALS.....	66
Model Description.....	66
Model Results.....	75

5	FCVI PROCESS MODELING.....	85
	Model Description.....	85
	Gas Mixture Transport Properties.....	94
	Material Transport Properties.....	98
6	FCVI EXPERIMENTAL RESULTS.....	103
	Tube Preform Fabrication.....	103
	Tube Infiltration Results.....	105
	Tube Density Characterization.....	112
	Preform Transport Property Measurement.....	120
7	FCVI PROCESS MODEL RESULTS.....	123
	Model Input.....	123
	Model Results.....	133
8	DISCUSSION.....	150
	Tube Infiltrations.....	150
	Preform Transport Properties.....	153
	Tube Density Characterization.....	157
	GTCVI Model Results and Validation.....	161
9	SUMMARY AND CONCLUSIONS.....	167
10	FUTURE WORK.....	176
	Scale-Up Considerations.....	176
	Composite Performance.....	178
	Process Model Improvement.....	179
	Heat Exchanger Design.....	180
APPENDICES		
A	GTCVI MODEL INPUT FILE.....	181
B	GTCVI TUBE PREFORM MATERIAL FILE.....	187
C	GTCVI GAS FILE.....	192
D	SAMPLE CALCULATIONS.....	194
	Tube Peform Volume.....	194
	Tube Preform Fiber Volume.....	195
	Tube Theoretical Density.....	195

Desired Liquid MTS Feed Rate.....	196
Total Molar Flux Calculation for Model Input.....	197
E PERMEABILITY CALCULATION.....	198
F SILICON CARBIDE OVERCOAT MASS CALCULATION.....	200
Average SiC Overcoat Thickness.....	202
SiC Overcoat Volume Segment.....	202
Total SiC Overcoat Volume.....	202
G X-RAY COMPUTED TOMOGRAPHY IMAGES.....	203
H DIGITAL IMAGES.....	214
REFERENCES.....	219
BIOGRAPHICAL SKETCH.....	225

## LIST OF TABLES

<u>Table</u>	<u>Page</u>
3-1 Nextel™ 312 Fiber Composition.....	40
3-2 Tube Preform Data.....	41
3-3 Nextel™ 312 Fiber Sleeve Length Schedule.....	41
4-1 Silicon Carbide Volumetric Deposition Rate Parameters.....	70
5-1 Radii and Lengths Used in the Starr Node/Bond Model.....	102
6-1 Initial FCVI Tube Data.....	107
6-2 FCVI Tube Data for CVI 1132.....	109
6-3 FCVI Data for Tubes Infiltrated for Various Time Lengths.....	110
6-4 FCVI Tube Data with Varied Process Conditions.....	111
6-5 Grayscale Values and Fitted Linear Density Relationship for the Nextel™312 Tube Preform and the Dense Nextel™ 312/SiC Specimens.....	112
6-6 CVI 1211 Density Results from X-ray Computed Tomography.....	113
6-7 CVI 1223 Density Results from X-ray Computed Tomography.....	114
6-8 CVI 1217 Density Results from X-ray Computed Tomography.....	114
6-9 CVI 1218 Density Results from X-ray Computed Tomography.....	114
6-10 Manual and Optimas™ Percent Area Comparison (Calibration Std.).	115
6-11 Optimas Relative Errors of the Grayscale Phases at Various Magnification.....	116

6-12	CVI 1217 Fiber Volumes from Digital Image Analysis.....	118
6-13	CVI 1217 Density Results from Digital Image Analysis.....	118
6-14	CVI 1218 Fiber Volumes from Digital Image Analysis.....	119
6-15	CVI 1218 Density Results from Digital Image Analysis.....	119
6-16	Experimental Comparative Summary of Tube Fiber Volumes and Theoretical Densities.....	120
6-17	Nextel™ 312/SiC Specimen Permeabilities.....	121
6-18	Perpendicular Thermal Diffusivities of Four Nextel™ 312/SiC Specimens of Varied Theoretical Density.....	122
6-19	Parallel Thermal Diffusivities of Three Nextel™ 312/SiC Specimens of Varied Theoretical Density.....	122
7-1	GTCVI Parameter Convergence Criteria.....	124
7-2	Infrared Thermometer Measurements at the Coating Chamber.....	125
7-3	GTCVI Boundary Conditions.....	126
7-4	GTCVI Infiltration Time Interval Table.....	126
7-5	Nextel™ 312/SiC Thermal Conductivity Data.....	129
7-6	Thermal Conductivity Data for Carborundum Fiberfrax™ Polycarbon Graphite Felt, and Poco H451 Graphite.....	131
7-7	Transport Properties for Other Associated Materials.....	132
7-8	Besmann and Chiang SiC Deposition Parameters (Equation 4-4).....	139
7-9	Total Infiltration Time (Hours) Matrix with $\alpha = 4.98$ .....	148
7-10	Model/Experimental Comparative Summary of Tube Fiber Volumes and Theoretical Densities.....	149



## LIST OF FIGURES

<u>Figure</u>	<u>Page</u>
3-1 The physical characteristics of the Nextel <sup>TM</sup> 312 braided sleeve.....	41
3-2 Tube preform assembly for FCVI.....	45
3-3 Tube preform, cooling and gas injector lines, Fiberfrax <sup>TM</sup> , graphite felt, and coating chamber used in the FCVI tube preform assembly.....	46
3-4 Schematic of the FCVI tube experimental apparatus.....	48
3-5 Cylindrical graphite heating element used in the FCVI tube furnace.....	49
3-6 Cross-section of the tube preform assembly.....	50
3-7 Nextel <sup>TM</sup> 312/SiC composite specimens.....	55
4-1 Tube preform description.....	68
4-2 Experimental SiC surface deposition rate data at different temperatures for several MTS/HCl/H <sub>2</sub> mixtures (Besmann et al. 1991).....	70
4-3 The thermal conductivity function used in the one-dimensional CVI model.....	72
4-4 The specific surface function used in the one-dimensional CVI model.....	72
4-5 Reaction rate ratios with variation of preform temperature.....	77
4-6 Reaction rate ratios with variation of the total molar flux.....	78
4-7 Reaction rate ratios with variation of the preform temperature difference.....	79

4-8	Reaction rate ratios with variation of the normalized simulated MTS depletion using $\theta=0.9$ .....	80
4-9	Reaction rate ratios with variation of the normalized simulated MTS depletion using $\theta=0.85$ .....	81
4-10	Reaction rate ratios with variation of the preform thickness.....	81
4-11	Transient CVI model simulation with use of an acceptable molar flux and temperature difference.....	84
5-1	Volume element array size used in the model domain.....	90
5-2	Boundary conditions specified in GTCVI.....	91
6-1	The variation of the phenolic resin volume percent and its effect on residual carbon.....	105
6-2	X-ray tomographic images indicating delamination of concentric Nextel™ 312 fiber sleeves seen in CVI 1102 .....	106
6-3	Excess SiC overcoat observed with tube CVI 1103.....	107
6-4	Nextel™ 312 tube preform dimensions for CVI 1132.....	108
6-5	X-ray computed tomographic images of CVI 1132.....	109
6-6	Calibration standard used for the BioScan Optimas™ image analysis software.....	115
6-7	Captured digital images of the composite tube cross-section.....	117
7-1	Coating chamber temperature profiles used in GTCVI.....	125
7-2	Specific surface area functions for the Nextel™ 312 preform.....	127
7-3	Effective diffusion coefficient function used for the tube preform.....	128
7-4	Nextel™ 312/SiC preform perpendicular and parallel permeability functions.....	130
7-5	Quaternary mixture molecular diffusivities for CH <sub>4</sub> and HCl.....	132
7-6	Quaternary gas mixture viscosity, heat capacity, and thermal conductivity functions.....	133

7-7	Initial Nextel™ 312 preform temperature profile.....	135
7-8	Nextel™ 312 preform temperature profile at 28 hours of infiltration.....	135
7-9	Variation of the radial temperature difference along the preform length initially and at 28 hours of infiltration.....	136
7-10	Transient preform radial temperature difference curves of the Nextel™ 312 preform with variation of the total flow.....	137
7-11	Transient average theoretical density curves for the Nextel™ 312 preform using the three different specific surface area functions.....	138
7-12	Transient average density curves using the SiC deposition parameters provided by Chiang (1999) and Besmann et al. (1991).	140
7-13	Nextel™ 312 theoretical density profile at six hours of infiltration.....	141
7-14	Nextel™ 312 theoretical density profile at 12 hours of infiltration.....	141
7-15	Nextel™ 312 theoretical density profile at 24 hours of infiltration.....	142
7-16	Nextel™ 312 theoretical density profile at 28 hours of infiltration.....	142
7-17	Transient average radial deposition rates in the Nextel™ 312 preform.....	143
7-18	Transient average theoretical density curves for the Nextel™ 312 preform with variation of the coating chamber mid-line temperature.....	144
7-19	Transient average theoretical density curves for the Nextel™ 312 preform with variation of $\alpha$ .....	145
7-20	Transient average theoretical density profiles for the Nextel™ 312 preform with variation of the total flow.....	145
7-21	Gas flow vector profile at the start of infiltration.....	146
7-22	Gas flow vector profile near the end of infiltration (28 Hours).....	147
7-23	Nextel™ 312 preform theoretical density profile at 15 hours of infiltration with the FCVI process conditions resulting in the lowest process time (1244°C, 18 slm, $\alpha=4.98$ ).....	148

E-1	Microsoft™ Excel98 spreadsheet used to determine the specimen permeability from least-squares regression analysis of the pressure drop and flow rate data.....	199
F-1	Diagram demonstrating circumferential positions where the SiC overcoat is measured for each X-ray tomographic image.....	200
F-2	Diagrams of the SiC overcoat volumes.....	201
G-1	Diagram of the tube preform indicating the axial positions where the X-ray tomographic images were taken.....	203
G-2	X-ray computed tomographic images for the Nextel™ 312 tube preform and the dense Nextel™ 312/SiC composite specimens.....	204
G-3	X-ray computed tomographic images for tube CVI 1211.....	206
G-4	X-ray computed tomographic images for tube CVI 1223.....	208
G-5	X-ray computed tomographic images for tube CVI 1217.....	210
G-6	X-ray computed tomographic images for tube CVI 1218.....	212
H-1	Digital image locations.....	214
H-2	Digital images taken from tube CVI 1217.....	215
H-3	Digital images taken from tube CVI 1218.....	217

## LIST OF SYMBOLS

$A_{CS}$	Area, cross-section [ $\text{cm}^2$ ]
$C$	Total molar concentration [ $\text{mol}/\text{cm}^3$ ]
$C$	Species concentration [ $\text{mol}/\text{cm}^3$ ]
$C_{p_i}$	Species gas heat capacity [ $\text{J}/\text{mol K}$ ]
$C_{p_{\text{Mix}}}$	Mixture gas heat capacity [ $\text{J}/\text{mol K}$ ]
$D_{i,j}$	Binary molecular diffusivity [ $\text{cm}^2/\text{sec}$ ]
$D_i^{\text{eff}}$	Species effective mixture diffusivity [ $\text{cm}^2/\text{sec}$ ]
$E_{af}$	Forward activation energy [ $\text{J}/\text{mol}$ ]
$E_{ar}$	Reverse activation energy [ $\text{J}/\text{mol}$ ]
$F$	Gas flow rate, Appendix E [ $\text{sccm}$ ]
$F_{\text{Total}}$	Total Flow Rate [ $\text{slm}$ ]
$GS$	Grayscale value [Dimensionless]
$ID_{\text{Average}}$	Average preform inside diameter [ $\text{cm}$ ]
$K_{fo}$	Forward deposition rate constant [ $\text{mol}/\text{cm}^2 \text{ sec}$ ]
$K_{ro}$	Reverse deposition rate constant [Dimensionless]
$L_{\text{Preform}}$	Preform Length [ $\text{cm}$ ]
$M_{AB}$	Binary molecular weight function [ $\text{mol}/\text{g}$ ]
$M_{\text{Composite}}$	Composite mass [ $\text{g}$ ]
$M_{\text{Preform}}$	Preform mass [ $\text{g}$ ]
$MW_i$	Species molecular weight [ $\text{g}/\text{mol}$ ]
$N$	Total molar flux [ $\text{mol}/\text{cm}^2 \text{ sec}$ ]
$N$	Axial node, Chapter 7
$N_i$	Species molar flux [ $\text{mol}/\text{cm}^2 \text{ sec}$ ]
$OD_{\text{Average}}$	Average preform outside diameter [ $\text{cm}$ ]
$P$	Pressure [ $\text{kPa}$ ]
$q$	Radial energy flux [ $\text{W}/\text{cm}^2$ ]
$R$	Universal gas constant [ $\text{J}/\text{mol K}$ ]
$R_s$	SiC surface deposition rate [ $\text{mol}/\text{cm}^2 \text{ sec}$ ]
$R_v$	SiC volumetric deposition rate [ $\text{mol}/\text{cm}^3 \text{ sec}$ ]
$r^*$	Radial distance [Dimensionless]
$S_e$	Specific surface area [ $\text{cm}^{-1}$ ]
$S_{\text{Radiation}}$	Volumetric radiation energy flux [ $\text{W}/\text{cm}^3$ ]
$T$	Temperature [Celsius or Kelvin]
$T_{\text{Exterior}}$	Preform exterior temperature
$T_i$	Temperature at given time step, Chapter 5
$T_{\text{Interior}}$	Preform interior temperature
$t$	Time [Sec or Hours]

$t_{1/2}$	Half-rise time [sec]
$u$	Average gas velocity [cm/sec]
$V_{\text{Fiber}}$	Fiber volume [g/cm <sup>3</sup> ]
$V_{\text{Matrix}}$	Matrix volume [g/cm <sup>3</sup> ]
$V_{\text{OC}}$	SiC overcoat volume [cm <sup>3</sup> ]
$V_{\text{OC}}^{\text{Segment}}$	SiC overcoat volume segment [cm <sup>3</sup> ]
$V_{\text{Preform}}$	Preform volume [cm <sup>3</sup> ]
$y_i$	Species mole fraction [Dimensionless]
$y_{\text{MTS}}^{\text{Feed}}$	MTS molar feed fraction [Dimensionless]
$\alpha$	Thermal diffusivity [cm <sup>2</sup> /sec], Chapter 3
$\alpha$	Hydrogen/MTS molar feed ratio [Dimensionless], Chapter 5
$\beta$	Permeability [cm <sup>2</sup> ], Chapter 3
$\beta$	Normalized MTS simulated depletion, Chapter 4
$\Delta T$	Radial temperature difference [Celsius]
$\delta_{\text{OC}}$	SiC overcoat thickness [ $\mu\text{m}$ ]
$\delta_{\text{OC}}^{\text{Average}}$	Average SiC overcoat thickness [ $\mu\text{m}$ ]
$\varepsilon$	Material emissivity, Chapter 5 [Dimensionless]
$\varepsilon_p$	Percolation threshold, Chapter 4 [Dimensionless]
$\eta_i$	Normalized reaction coordinate [Dimensionless]
$\theta$	Dimensionless temperature difference, Chapter 4
$\lambda_i$	Species thermal conductivity [W/cm K]
$\lambda_{\text{Mix}}$	Mixture thermal conductivity [W/cm K]
$\mu_i$	Species gas viscosity [g/cm sec]
$\mu_{\text{Mix}}$	Mixture gas viscosity [g/cm sec]
$v_i$	Species stoichiometric coefficient [Dimensionless]
$\rho$	Theoretical density [%]
$\rho_i$	Species absolute density [g/cm <sup>3</sup> ]
$\rho C_p$	Composite heat capacitive function [J/cm <sup>3</sup> K]
$\rho C_{p_i}$	Species heat capacitive function [J/cm <sup>3</sup> K]
$\sigma$	Stefan-Boltzmann constant, Chapter 5 [W/cm <sup>2</sup> K <sup>4</sup> ]
$\sigma_{ij}$	Binary collision diameter [ $\text{\AA}$ ]
$\sigma_i$	Species collision diameter [ $\text{\AA}$ ]
$\tau_{\text{Preform}}$	Preform thickness [cm]
$\tau_{\text{Specimen}}$	Specimen thickness [cm]
$\phi_{ij}$	Binary interaction parameter [Dimensionless]
$\Omega_D$	Stockmayer diffusivity collision integral, Chapter 5 [Dimensionless]
$\Omega_V$	Stockmayer viscosity collision integral, Chapter 5 [Dimensionless]

Abstract of Dissertation Presented to the Graduate School  
of the University of Florida in Partial Fulfillment of the  
Requirements for the Degree of Doctor of Philosophy

MODEL-AIDED FABRICATION OF FIBER-REINFORCED  
CERAMIC COMPOSITE TUBES USING FORCED-FLOW  
CHEMICAL VAPOR INFILTRATION

By

KENT JOSEPH PROBST

May 2000

Chairman: Timothy Anderson  
Major Department: Chemical Engineering

Fiber-reinforced ceramic composites possess high thermal conductivity, high fracture toughness, and corrosion resistance, having potential for use in fossil-energy steam plants, where corrosive environments at high temperature and pressure exist. The utilization of fiber-reinforced ceramic composite tubes may enable plant operation at higher temperatures, and may extend the lifetime of specific plant operations, improving overall efficiencies and reducing downtime.

Dense, fiber-reinforced ceramic composite tubes were fabricated using forced-flow, chemical vapor infiltration. This process involved gaseous ceramic precursor infiltration throughout a fibrous preform, where a temperature gradient was applied and a ceramic precursor was forced through its surface at lower temperature. The application of a suitable temperature gradient and total flow

enabled the ceramic matrix deposition to preferentially translate from the preform hot-surface to the cold-surface, resulting in a dense, ceramic composite in a reasonable total process time.

Fibrous tube preforms were fabricated with Nextel™ 312 fiber. Silicon carbide was the reinforced ceramic matrix, which was deposited throughout the tube preform using methyltrichlorosilane. A standard set of process conditions was attempted to evaluate the feasibility in achieving dense composites. Tube preform infiltrations with variation in temperature and total flow were performed to determine effects on final density and total process time.

Density characterization was performed on tube preforms infiltrated with the same process conditions for various time lengths to study the transient tube densification. Tube density profiles were characterized using X-ray computed tomography and digital image analysis, and the results from both were compared for their effectiveness in the prediction of the transient tube densification.

A comprehensive process model simulated the transient tube infiltration using multiple, steady-state intervals. Transport properties were input into the model and were determined either by experiment or by calculation using a descriptive model. The model prediction was validated to experimental tube density results by the adjustment of model parameters. The model was then used to determine minimum process times that yielded acceptable tube density, while these times were compared to those seen in experiment. The model density profiles were compared to those found with the density characterization methods to evaluate the process simulation.



## CHAPTER 1 INTRODUCTION

This dissertation presents research involving the fabrication of fiber-reinforced ceramic composite tubes using forced-flow, chemical vapor infiltration (FCVI). Experimental methods were developed to fabricate fibrous tube preforms, 5 cm in ID, 6.4 mm in thickness, and 30 cm in length, with suitable fiber volume. The experimental results of the ceramic composite tube fabrication using the FCVI process were evaluated for the successful achievement of acceptable tube density, density uniformity, and total process time. Density characterization was done on tube preforms infiltrated with the same process conditions for various time lengths to study the transient behavior of the tube densification.

A comprehensive FCVI model was used to simulate the FCVI of tube preforms, where process parameters were varied to evaluate effects on the densification rate and total process time. The model was made to reasonably predict the experimental tube infiltrations through appropriate tuning of the model parameters, and the model results were compared to the experimental tube infiltration results to evaluate model predictability of the FCVI of tube preforms.

## Motivation

The United States Department of Energy is currently searching for new technologies that improve overall efficiencies of fossil-energy steam plants. Current overall fossil-energy steam plant efficiencies are between 25-30% (12<sup>th</sup> Annual Conference on Fossil Energy Materials, Knoxville, TN, 1998). The improvement of plant efficiencies to 40-50% is the desired goal established by the Department of Energy by the year 2010.

Fossil-energy steam plant efficiencies today are limited by the plant operation temperature and by the lifetime of the construction materials at the operation temperature. The flue gas, from coal combustion, is at high temperature (1500°C) and is highly corrosive. A proposed solution to the improvement in plant efficiency is the direct heat exchange of the high-temperature flue gas with a working fluid, which is subsequently fed to turbines for power generation. The desired heat exchanger design calls for the shell-and-tube type involving multiple tube passes. In a given tube pass, the working fluid would flow through the tube interior while the combustion flue gas would flow over the tube exterior.

The proposed dimensions of the fiber-reinforced ceramic composite tubes in the heat exchanger design are 5 cm in ID, 6.4 mm in thickness, and 120 cm in length. The ceramic composite tubes only need to be used for the tube passes near the flue gas inlet and the working fluid outlet, where the higher temperatures exist (~1100°C). Traditional construction materials for the heat exchanger tube

passes, including metal alloys and aluminides, may be used downstream in the combustor flue pass in the heat exchanger, where the fluid temperatures are lower.

Monolithic silicon carbide was suggested as a construction material for the heat exchanger tubes (Iwamoto 1991). Silicon carbide (SiC) is a promising candidate for heat exchange, for it has reasonable thermal conductivity (20 W/m K at 1000°C), low absolute density (3.2 g/cm<sup>3</sup>) and excellent corrosion resistance (Schlichting 1980).

Monolithic SiC has acceptable thermal conductivity, but possesses catastrophic, brittle behavior at high, applied loads, invoked by high temperature (1100°C) and pressure (10-20 MPa). Reinforcement of the monolithic SiC with continuous ceramic fiber improves fracture toughness and creep resistance, yet retains the thermal conductivity necessary for sufficient heat exchange (Lowden et al. 1987). The use of SiC is also desirable for its corrosion resistance by the formation of a SiO<sub>2</sub> layer at its surface (Schlichting 1980).

The implementation of the fiber-reinforced ceramic composite tubes in a workable, heat exchanger design would increase the initial capital investment in the heat exchanger development and construction. However, the composite tubes would improve the lifetime of the heat exchanger and enable operation at higher temperatures, making the higher initial capital investment worthwhile in the long-term.

## **Ceramic Composite Processing Alternatives**

The fabrication of fiber-reinforced ceramic composites involves the addition of a suitable ceramic matrix throughout a porous preform of continuous ceramic fibers. The ceramic matrix deposits on the fiber surface and consumes the preform porosity that surrounds the fibers, and can be incorporated into the fibrous preform with either a liquid-phase route or a gas-phase route.

Ceramic composite fabrication with ceramic matrix consolidation by use of a liquid-phase includes hot pressing and sintering techniques. A disadvantage that is prevalent with both processes is their high processing temperature (1200-1400°C) and pressure (30-50 MPa). This demanding, process environment damages the fibers, thus destroying the load-carrying capabilities of the ceramic composite.

Ceramic composite fabrication with ceramic matrix consolidation by a gas phase is known as chemical vapor infiltration (CVI). In CVI, ceramic precursors in the gas phase infiltrate through the fibrous preform and deposit ceramic matrix at the fiber surface by heterogeneous reaction. The lower temperatures and pressures used in CVI (1000-1200°C, 1-100 kPa) neither thermally nor mechanically degrade the fiber, while the matrix deposit places little mechanical stress on the fiber upon deposition.

The first developed CVI method involves ceramic precursor infiltration of fibrous preforms at constant temperature and pressure (ICVI). Ceramic precursor transports through the preform primarily by diffusion. The slow,

reactant transport by diffusion limits thorough deposition throughout the preform thickness, with the highest matrix deposition rates seen at the preform exterior surface. This ICVI process is successful for fabrication of thin-walled ( $<3$  mm) composites with total process times on the order of 1000 hours.

A viable alternate process for the fabrication of fiber-reinforced composites is forced-flow, thermal gradient, chemical vapor infiltration (FCVI). The use of a forced-flow enhances ceramic precursor transport through the preform by application of a pressure gradient. A temperature gradient is also placed across the preform thickness against the pressure gradient, with the ceramic precursor forced at the preform surface at lower temperature. The higher preform temperature competes with the ceramic precursor depletion in the ceramic matrix deposition rate, as the ceramic precursor infiltrates from the cold-surface to the hot-surface. A suitable temperature gradient and total flow may be applied such that ceramic matrix deposition preferentially translates from the preform-hot surface to the cool surface, resulting in a final uniform preform density.

The FCVI process has been used to fabricate dense, fiber-reinforced ceramic composites on the order of 24 hours (Stinton et al. 1986), which is significantly lower than the process times seen with ICVI ( $\sim 1000$  hours). Both the reduction in process time and the densification of near-net shape preforms make the FCVI process an attractive method for fabrication of fiber-reinforced ceramic composite tubes.

## CHAPTER 2

### CVI BACKGROUND AND LITERATURE REVIEW

This chapter reviews the existing literature and background on ceramic composite processing, which includes extensive experimentation and modeling efforts of the chemical vapor infiltration (CVI) process. Various studies of the SiC deposition kinetics from methyltrichlorosilane (MTS) are reviewed along with the required process conditions for a stoichiometric, single-phase SiC deposit and the dominant intermediate species that result from MTS thermal decomposition. Developed models and experimental methods are reviewed for their prediction and evaluation of the pertinent composite transport properties.

#### **Composite Processing Techniques**

The techniques used for ceramic composite processing involve the incorporation of the ceramic matrix to the fibrous preform by either a liquid phase or a gas phase-route. Chemical vapor infiltration (CVI), which incorporates a ceramic matrix throughout a fibrous preform by a gas-phase route, is reviewed in detail. Several developed CVI methods are described and compared for their feasibility in fabricating composites of uniform density and their required total process times.

## Liquid-Phase Composite Processing

Fiber-reinforced ceramic composite fabrication that uses a liquid phase-method involves hot pressing (Ezis 1991) and sintering (Coblentz 1991) methods. The fibrous preform is impregnated with a ceramic powder, which is suspended with a suitable liquid. The liquid-impregnated preforms are pressed and sintered at pressures between 30-50 MPa and at temperatures between 1200-1400°C. A disadvantage that these methods have is that the high operation temperature and pressure causes crystallization of the amorphous phase that constitutes the bulk of most fibers and mechanical damage to the brittle fibers.

Another liquid-phase process used in fiber-reinforced ceramic composite fabrication is one that involves polymer impregnation and pyrolysis (PIP). The PIP process involves the impregnation of a fibrous preform with a thermosetting organometallic polymer. Typical organometallic polymers that are used for SiC matrix incorporation are polycarbosilanes of the general form,  $R_2SiCl_{4-z}$ . The polymer-impregnated preforms are typically pyrolyzed at 1000°C under vacuum. Preform shrinkage is observed during the pyrolysis while many impregnation/pyrolysis cycles must be performed to achieve final composite theoretical densities between 90% and 95%. The numerous impregnation and pyrolysis cycles resulted in rather long process times (~100 hours) (Interrante et al. 1995).

Fabrication of fiber-reinforced ceramic composites by a reactive melt infiltration involves ceramic matrix consolidation by the reaction between the fibrous preform and a liquid phase containing the desired matrix constituent.

Hillig (1974) impregnated carbon particulate-containing preforms with liquid silicon to form a SiC/Si composite system by conversion of the carbon particulates to SiC by reaction with the liquid silicon melt. Typical temperatures of the melt infiltration process are necessarily high (1600°C).

### **Gas-Phase Composite Processing**

The process used to deposit ceramic matrix throughout a fibrous preform by use of a gas phase is chemical vapor infiltration. In chemical vapor infiltration (CVI), a ceramic precursor in the gaseous phase infiltrates through the thickness of the fibrous preform and deposits on the fiber surface by heterogeneous reaction, with the incorporated ceramic matrix consuming the porous microstructure. Chemical vapor infiltration is performed at low to atmospheric pressure (5-100 kPa) and moderate temperatures (1000-1200°C), where these conditions do not promote substantial thermal and mechanical damage to the fiber. Several CVI methods have been developed and evaluated in efforts to fabricate fiber-reinforced ceramic composites of various shapes and thickness while achieving uniform density with reasonable total process times.

#### **Isothermal, Isobaric CVI (ICVI)**

The first CVI process utilized in fiber-reinforced composite fabrication is the isothermal, isobaric chemical vapor infiltration (ICVI). In ICVI, the ceramic precursor is introduced to the isothermal preform exterior and is transported through the porous preform thickness primarily by diffusion. The slow precursor



transport by diffusion limits the penetration of the precursor, with preferential matrix deposition occurring at the preform exterior surface. As the gas diffuses through the preform thickness, the precursor concentration decreases and gaseous, reaction by-product increases leading to lower matrix deposition rates. The continued high matrix deposition at the preform exterior results in the formation of an impermeable matrix layer, preventing further precursor infiltration through the preform thickness. Bickerdike et al. (1962) was the first referenced investigator to utilize the ICVI process by densifying porous graphite with carbon matrix.

The ICVI process must be halted periodically to machine the impermeable matrix deposit on the preform exterior, which re-opens the accessible preform pores to further precursor infiltration. The uniformity in the matrix deposition improves by lowering both temperature and pressure. The lower temperature and pressure increases precursor transport through the preform, but decreases the matrix deposition rate. This results in excessive infiltration times (~1000 hours) required for densification of thin-walled preforms (<3 mm).

Although the total infiltration times with ICVI are excessive, many preforms of any particular shape can be infiltrated in the same batch environment. Several investigators used the ICVI process to fabricate C/C and SiC/SiC composite systems (Naslain et al. 1981, Fitzer and Gadow 1986, Xu and Zhang 1997). High composite theoretical densities (~90%) were achieved in process times from 2-6 weeks. Allied Signal (Newark, DE) and SNECMA (Bordeaux, France)

have implemented the ICVI process for the fabrication of C/C and C/SiC composites at the commercial level.

### **Thermal Gradient, Isobaric CVI**

The application of a temperature gradient to the isobaric CVI process prevents preferential matrix deposition at the preform exterior. The temperature gradient is applied by heating one preform surface and cooling the other surface either directly or indirectly. The ceramic precursor diffuses into the preform from the cold-surface. At the preform cold-surface, lower matrix deposition is observed due to the lower temperature, for the matrix deposition rate has an exponential Arrhenius temperature dependence. As the precursor diffuses towards the preform hot-surface, matrix deposition increases due to higher temperature.

The preferred matrix deposition at the preform hot-surface enhances the thermal conductivity in this preform region, which subsequently conducts heat to the preform cold-surface, increasing its temperature, which supports higher deposition rates with greater available surface area and precursor concentration. Therefore, the matrix deposition advances from the preform hot-surface to the preform cold-surface.

Streckert et al. (1996) densified filament wound-tubes of Nicalon™ fiber (Nippon Corporation, Tokyo Japan) with SiC matrix for design in fusion reactor applications by the use of inductive preform heating (1100°C) and MTS precursor. Pressurized composite tube-leak rates were less than  $10^{-5}$  cm<sup>3</sup>/sec

using 15 MPa helium at 1000°C indicating suitable application performance. Golecki (1996) densified carbon fiber preforms with carbon matrix at 1200°C using liquid  $C_5H_{10}$  as a carbon precursor. He used radio frequency (RF) heating and external cooling to establish the temperature gradient across the carbon fiber preform. Carbon annular disk preforms were fabricated in 26 hours realizing 30% reagent efficiency and composite densities of  $1.8 \text{ g/cm}^3$ .

### **Isothermal, Forced-Flow CVI**

An isothermal, forced-flow CVI process enhances precursor transport through the preform thickness by the application of a pressure gradient (viscous flow). The concept of a forced flow was proposed to increase the precursor pore penetration depth and to reduce the total infiltration time. Both Kotlensky (1973) and Rudolph et al. (1996) fabricated C/C composite systems by this method. Infiltration times were reduced with the forced flow, however density gradients were still apparent in the carbon fiber preforms. Roman (1995) densified carbon and Nicalon™ preforms with SiC matrix with infiltration times much lower than those seen with ICVI (~50 times lower) and observed a trade-off between infiltration time and density uniformity, where shorter infiltration times lead to a higher degree of density nonuniformity and vice-versa.

### **Forced-Flow, Thermal Gradient CVI (FCVI)**

The forced-flow, thermal gradient chemical vapor infiltration (FCVI) process was developed by researchers at Oak Ridge National Laboratory (Oak

Ridge, TN) to drastically reduce process time while achieving uniform preform density with the enhancement of ceramic precursor transport and the prevention of premature preform sealing (Caputo and Lackey 1984). Temperature and pressure gradients are involved in the process, with the pressure gradient placed against the temperature gradient across the preform thickness.

Similar to the thermal gradient, isobaric CVI process, the temperature gradient is placed across the preform thickness by heating one surface and cooling the other surface either directly or indirectly. The pressure gradient developed from the viscous flow is also placed across the preform thickness, with the precursor entering the preform at its surface at lower temperature.

At the preform cold surface, ceramic matrix deposition is low due to the low temperature. As the ceramic precursor infiltrates through the preform, the precursor concentration is lowered due to depletion, but the local preform temperature is higher. The increase in temperature counterbalances the precursor depletion in the ceramic matrix deposition rate.

A suitable temperature and pressure gradient may be applied to the preform such that the ceramic matrix deposition advances preferentially from the preform hot-surface to the cold-surface, resulting in a more uniform composite density with a significant reduction in process time. Total infiltration times on the order of 24 hours were realized using the FCVI process achieving final composite theoretical densities between 80-90% with Nicalon™/SiC composites (Stinton et al. 1986).

Several investigators have used the FCVI process to densify either carbon or SiC fibrous preforms, of various shapes, with SiC matrix. Mühlratzer et al. (1996), of MAN Technologie (Germany), fabricated complex, carbon fiber/SiC matrix composite components for assembly of a hypersonic vehicle air intake ramp. Composite component theoretical densities of 90% were realized, having acceptable mechanical properties at high temperature and having lower densities than typical metal alloy counterparts normally used in the ramp assembly. MAN Technologie was the first company to commercialize the FCVI process with the fabrication of integrated composite structures from composite component parts.

Matlin (1995) used the FCVI process to densify Nicalon™ cloth lay-ups with SiC matrix using a two-step sequence. Two sequential temperature gradients with a 1200°C preform hot-surface temperature were utilized (220°C and 450°C) to promote uniform matrix consolidation in the intrabundle porosity and in the porosity throughout the interstitial channels and the interlaminar porosity. Stinton et al. (1992) also attempted to densify filament-wound, three-dimensional, and cloth-wrapped Nicalon™ tubular preforms with SiC matrix. High Nicalon™/SiC composite theoretical densities were achieved with the filament-wound preforms (~90%) while lower densities were achieved with the three-dimensional and cloth-wrapped preforms (70%-80%) due to the uninfiltreated large voids in their porous microstructure. Lauten (1998) fabricated SiC/Si<sub>3</sub>N<sub>4</sub> composites of high theoretical density (>80%) and complex geometry for application in aerospace design.

Vaidyaraman et al. (1996) densified carbon cloth preforms with carbon matrix, using either  $\text{CH}_4$  or  $\text{C}_3\text{H}_6$  precursor and hydrogen diluent, at preform hot-surface temperatures between 1100-1400°C. Composite theoretical densities as high as 93% were achieved in 8-12 hours of process time. Average deposition rates as high as 3  $\mu\text{m}/\text{hour}$  were achieved, indicating an increase of an order of magnitude to deposition rates achieved with the isobaric, isothermal CVI process.

### **Pressure-Pulse CVI**

Pulsed chemical vapor infiltration (PCVI) involves rapid pressurization and depressurization of the fibrous preform with the ceramic precursor. This alternate CVI method was proposed to rapidly transport precursor into the preform volume and to eliminate the inhibition of matrix deposition incurred by precursor by-product. Most carbide precursors that were utilized were chlorosilanes, which produce  $\text{HCl}$  upon decomposition and reaction, which inhibits matrix deposition. Evacuation of the precursor by-product and the refilling of fresh precursor, with proper selection of the pressurization and depressurization cycle hold times, can reduce the  $\text{HCl}$  residence time inside the preform and achieve significant weight gains with many consecutive cycles (~10000).

Ohzawa et al. (1996) applied the pressure pulse CVI method to densify chopped cotton fiber preforms of low fiber volume (~10%) with  $\text{SiC}$  matrix. Increase in theoretical density to 20% was realized after 15000 pulses at 1150°C.

Beatty and Kiplinger (1970) densified porous graphite with carbon using pressurization and depressurization cycles at 240 kPa and 0.03 kPa respectively. Increase of the graphite substrate weight by 8% was achieved in approximately 3000 cycles. A trade-off was realized between infiltration temperature and total infiltration time, with the use of lower temperatures resulting in higher weight gain and longer infiltration time.

### **Alternating Flow CVI**

The alternating flow CVI method involves periodic reversal of precursor infiltration through an isothermal preform. The flow alternation is performed in an attempt to eliminate density gradients in the final composite. Chiang (1999) attempted to densify Nicalon™ cloth lay-up disk preforms with SiC matrix using a 1200°C preform temperature and various total flows (300-900 slm). Although the total process times were short (8-12 hours), 70% theoretical densities with density gradients were still apparent in the infiltrated composites.

The review of the experimental CVI work indicates that application of a temperature gradient and the enhancement of precursor transport can lead to uniform, acceptable ceramic composite densities in reasonable total process time. The FCVI process has the potential to fabricate dense, thick-walled ceramic composites with relatively short process times (~24 hours), and may be extended to the fabrication of preform geometries of higher complexity. However, specific preform fixturing is required to establish the forced flow and the temperature gradient across the preform thickness.

## **CVI Modeling Efforts**

Modeling of the CVI processes can provide insight into the many phenomena that occur, including heat and mass transport, chemical reaction, and evolving transport properties of the preform. The ultimate goal in CVI is the fabrication of a dense composite with high density and minimum density gradient and total process time. The selected CVI method depends on the preform geometry, thickness, and the precursor that is utilized. Application of a suitable CVI model can help determine the necessary process parameters for successful matrix consolidation without excessive experimentation.

### **Isothermal, Isobaric CVI (ICVI) Modeling**

Initial modeling efforts of the ICVI process were based on the solution of the diffusion/reaction problem in simplified pore geometries. The investigators that attempted to model the ICVI process differed in their respective models by their definition and description of the evolving, preform pore geometry. This summary of modeling work includes the assumption of first-order reaction kinetics and the use of a parallel diffusivity combination that considers both molecular and Knudsen contributions (large and small molecular mean free paths respectively). The deposition thickness along the pore length depends on the Thiele modulus (Satterfield et al. 1963), a dimensionless ratio comparing contributions from diffusion and chemical reaction. A low Thiele modulus ( $<1$ ) represents a reaction limited-regime while a high Thiele modulus ( $>10$ )



represents a diffusion limited-regime. A low Thiele modulus favors greater deposition uniformity along the preform thickness.

Fitzer and Gadow (1986) modeled SiC precursor diffusion and SiC matrix consolidation in a single cylindrical pore while Rossingnol et al. (1984) modeled TiC precursor diffusion and TiC consolidation in a structured array of unidirectional cylindrical pores. Tai and Chou (1989) used an array of random, non-intersecting unidirectional cylinders to model the porous microstructure consolidated with  $\text{Al}_2\text{O}_3$  from  $\text{AlCl}_3$ ,  $\text{CO}_2$ , and  $\text{H}_2$  precursors. Starr (1991) and Melkote and Jensen (1989) modeled SiC matrix deposition within an isotropic, three-dimensional, intersecting cylindrical pore network. Gupte and Tsamopolous (1990) modeled SiC deposition throughout a simulated pore network defined by a Bethe lattice (Stauffer and Aharony 1992) of given coordination number, where the coordination number translates to the pore connectivity. Sheldon and Besmann (1990) and Currier (1990) modeled matrix consolidation within a pore microstructure of a fiber bundle using an analytical expression for impinging fiber surfaces.

Chung and McCoy (1991) modeled the multi-modal preform pore network in a three-step sequence. The intrabundle porosity was assumed to densify first with subsequent deposition in the interstitial channels and the interlaminar porosity. The use of the pore idealization was justified realizing that the actual preform porosity consisted of small micropores ( $\sim 10 \mu\text{m}$ ) between contiguous fibers and larger macropores ( $\sim 1 \text{ mm}$ ) at the interstitial channels and in between adjacent fiber layers.

Griffiths and Nilson (1998) modeled the ICVI process for application of BN fiber coating throughout a fibrous preform. Boron nitride was deposited from  $\text{BCl}_3$  and  $\text{NH}_3$  precursors introduced at both preform exterior surfaces, reducing the characteristic length scale by one-half. Optimal pressures and temperatures were found that favored maximum fiber coating at the preform center and the highest average coating deposit.

Sotirchos (1991) developed a one-dimensional ICVI model that used a dusty-gas model to describe multicomponent species diffusion (Mason and Malinauskas 1983). A random, one-dimensional cylindrical pore network was used to describe the preform porosity. The deposition profiles along the preform thickness were similar to those found by other investigators, however, he suggested that use of Fick's law for diffusion overestimates matrix deposition considerably through the preform thickness by the neglect of multicomponent effects.

The conclusion of the ICVI modeling results show that matrix deposition is favored at the preform exterior, where the precursor is introduced, while the matrix deposition monotonically decreases along the preform thickness due to the slow precursor transport and precursor depletion. The matrix deposition uniformity is improved by enhanced precursor transport with lower temperature and pressure at the expense of longer infiltration times.

### **Thermal Gradient, Isobaric CVI Modeling**

Skamser et al. (1997) considered application of temperature gradients in the isobaric CVI process. The applied temperature gradient forced a lower Thiele modulus in the preform region near the cold surface because of the lower temperature, making the matrix deposition fall within the reaction limited-regime. Optimal temperature gradients were found such that the total infiltration time was minimized, leaving a minimum in the residual preform porosity. High temperatures, temperature gradients, and pressures were necessary to achieve minimum infiltration times, and higher temperature gradients were necessary for thicker preforms due to an increase in resistance to diffusion. Gupte and Tsamopolous (1990) also considered application of temperature gradients with isobaric CVI and concluded that use of a temperature gradient alone could not counterbalance diffusion limitations, leading to undesired density gradients.

### **Modeling with Alternate Heating Methods**

Gupta and Evans (1991) and Midha and Economou (1997) considered microwave and RF heating of fibrous preforms in the isobaric CVI process. The Maxwell equations, defining the electromagnetic field, were solved separately to determine the temperature profile prior to solution of the mass transport and solid reaction balances. Both concluded that manipulation of either the microwave or RF power promoted the achievement of uniform density in the preform. Midha and Economou noticed density progression in the two-dimensional preform to

occur along the preform thickness before progressing along the preform length. Localized high deposition in areas of the preform yielded higher density (higher electrical conductivity) which led to thermal runaway (uncontrolled temperature rise), resulting in non-uniform density in the final composite.

### **Pressure-Pulse CVI Modeling**

Ofori and Sotirchos (1996) modeled pressure-pulse CVI utilizing different pulse waveforms and temperature gradients established by microwave heating. The rapid-filling of precursor and evacuation of reaction by-product by pressure pulsing was performed to eliminate the density gradients in the preform. Their conclusions showed that density gradients could be eliminated in the final composite by the appropriate tuning of the microwave power and the pulse interval lengths (hold-times).

### **Forced Flow, Thermal Gradient CVI (FCVI) Modeling**

Descamps and Vignoles (1996) developed a one-dimensional CVI model using the finite element method coupling energy, momentum, and species balances, which established both temperature and pressure gradients across the preform thickness. The model results only focused on initial temperature, pressure, and reactant concentration fields. These fields were simulated with and without heterogeneous chemical reaction and the results demonstrated that chemical reaction increased the pressure drop across the preform thickness,

although the chemical reaction had no effect on the temperature profile through the preform thickness.

Ofori and Sotirchos (1997) modeled the FCVI process utilizing a pressure gradient and a temperature gradient. Their rigorous model, which included multicomponent transport defined by the dusty gas-model (Mason and Malinauskas 1983), was compared to a simple model that considered only viscous mass transport and solid reaction. Both simple and rigorous models were used to compare their respective reaction rates that occurred along the preform thickness. The simple model was in excellent agreement with the rigorous model with high molar fluxes, representative of a substantial viscous flow. With the implementation of both isothermal and non-isothermal preform conditions, a maximum in the reaction rate was observed in the middle of the preform thickness for all considered total molar fluxes indicating the counterbalance of reactant and by-product concentration.

Starr and Smith (1992) has developed a three-dimensional, finite volume model specifically for simulation of the FCVI process. The model development was in conjunction with experimental FCVI work done at the Oak Ridge National Laboratory. Actual process configurations were partitioned into an array of finite-volume elements. Energy, momentum, continuity, and species balances were solved over the entire volume element array with applied boundary conditions using a central difference technique (Patankar 1980). Darcy's law (Darcy 1856), which applies to flow in a permeable, porous medium, was used to define the momentum and continuity equations. The energy balance included conduction,

convection, and radiation, which dominates the energy transport to the preform at typical infiltration temperatures ( $\sim 1200^{\circ}\text{C}$ ). The momentum and energy balances were de-coupled from the species balances for simplicity and ease of solution convergence.

The steady-state solutions of temperature, pressure, and species concentrations at multiple time intervals were determined and filed for inspection of the transient densification in the preform. Transport properties for both the infiltrating, reactant gas mixture (temperature dependent) and the preform (density dependent) were input to the model, with the preform transport properties determined either by experiment (Starr and Hablutzel 1998) or by a characteristic model (Starr 1995).

Starr and Smith (1995b) handled the thermal radiation in the energy balance with the use of a ray-tracing procedure using Monte Carlo methods. View factors for all volume elements that bordered open gas space were calculated, where the view factor for a particular volume element surface related the radiation emitted and the summation of the radiation received from all other emitting surfaces. The critical assumption used in this radiation algorithm was that the element surface temperature was the same as the node temperature, which is located at the element center. The implementation of the thermal radiation algorithm to their finite volume model produced temperature profiles that closely agreed with experimental measurement.

Matlin (1995) used the finite volume CVI model developed by Starr to optimize one-dimensional infiltration of Nicalon<sup>TM</sup> fibrous disk preforms. He

found that two different sequential temperature gradients were needed to promote uniform densification of the bimodal porosity of the Nicalon™ preforms (220°C and 450°C respectively), leading to a uniform, high composite density. The results from the model had considerable correlation with the results from his experimental preform infiltrations.

Tai and Chou (1990) modeled SiC consolidation from MTS precursor in a structured three-dimensional unit cell. The preform was partially enclosed with heating elements that enabled the variation of temperature in certain regions. Variation of the element temperatures and the apparent activation energy of the SiC deposition were performed to investigate the effects of density uniformity in the preform. They found an element heating schedule and an assumed activation energy that resulted in the best density uniformity in the preform, and concluded that the model results were directly dependent on the values of both the temperature and the activation energy.

### **Alternating Flow CVI Modeling**

Ofori and Sotirchos (1997) and Chiang (1999) modeled the CVI process that utilized an alternating flow, where the gas flow through the preform was periodically reversed. The results from Ofori and Sotirchos demonstrated that the use of a periodic flow reduced final density gradients in the preform, similar to the density results seen with the application of a temperature gradient. However, the modeling results from Chiang demonstrated that the use of a periodic, alternating flow still produced density gradients throughout the preform. The model density profiles produced by Chiang yielded considerable agreement

with the density profiles found with his experimental preform infiltrations through appropriate tuning of the deposition rate parameters.

The summary of the CVI modeling literature indicated that the isobaric CVI process lead to density gradients in the preform even with the use of low, but sufficient, temperatures and pressures and a suitable temperature gradient. The use of a forced-flow, either periodic or continuous, with a thermal gradient could minimize density gradients and could achieve acceptable composite density with relatively short process times. Proper prediction of experimental infiltration depended on the definitions of the evolving, transport properties of the preform that are input to the given CVI model, such as permeability, specific surface area, and thermal conductivity.

### **Silicon Carbide**

This section discusses the silicon carbide (SiC) morphology, thermodynamic equilibrium calculations, and the kinetics and deposition rate studies from MTS. The process conditions that lead to a single-phase SiC matrix deposit are discussed. The intermediate gaseous species from MTS thermal decomposition determined by both experiment and calculation are presented and compared. The numerous observations of the SiC deposition kinetics by several investigators are presented and compared for their dependence on reactor temperature, reactor type, MTS concentration, depletion, and residence time.



## SiC Morphology

Schlichting (1980) reviewed the SiC chemical vapor deposition with many different chemistries and substrates. The dominant matrix deposit phase observed at temperatures above 1000°C is  $\beta$ -SiC (cubic) oriented in the [111] plane with minor orientation in the [220] plane. The [111] plane orientation parallel to the substrate was favored at high deposition temperatures, however, [111] plane orientation perpendicular to the substrate and [220] plane orientation parallel to the substrate was observed under certain deposition conditions. Smooth SiC deposits were observed at low temperatures (1000°C) while faceted and columnar deposits were seen at higher temperatures (1500°C). The most favorable precursor used for the deposition of SiC was methyltrichlorosilane (MTS) due to the quality of the deposit and the 1:1 gram-atomic ratio of Si and C.

The thermal decomposition of MTS was best supported in hydrogen, for it aided the formation of separate siliconaceous species (chlorosilanes) and carbonaceous species (hydrocarbons) (Allendorf et al. 1994). Thermal decomposition of MTS in Ar led to free carbon deposit at high temperatures, lacking the support for the formation of condensed Si (Schlichting 1980) (Lackey 1990). The use of different hydrogen/MTS ratios, from 5-50, led to  $\beta$ -SiC deposit. The SiC deposit had a maximum density of 3.21 g/cm<sup>3</sup>, with the deposit density increasing with an increase in the hydrogen/MTS ratio (10-25). Deposition at lower temperatures (1100°C) and high hydrogen/MTS ratios (>100) yielded elemental Si while deposition at higher temperatures (1700°C) and low hydrogen/MTS ratios (<15) yielded elemental C.

## MTS Decomposition

Schlichting (1980) reported the dominant intermediate species resulting from MTS thermal decomposition by flowing a hydrogen/MTS gas mixture through a heated silica tube and by species detection using mass spectrometry. Around 1000 K, the most prevalent intermediate gas species were  $\text{CH}_4$ ,  $\text{SiHCl}_3$ ,  $\text{HCl}$ , and  $\text{SiCl}_4$  while at 1700 K,  $\text{SiCl}_4$ ,  $\text{SiHCl}_3$ ,  $\text{CH}_4$ ,  $\text{C}_2\text{H}_6$ , and  $\text{C}_2\text{H}_2$  were detected. Pyrolysis of the MTS yielded either a silicon chloride ( $\text{SiCl}_x$ ) or a chlorosilane ( $\text{H}_x\text{SiCl}_{4-x}$ ) with a saturated hydrocarbon ( $\text{CH}_4$  or  $\text{C}_2\text{H}_6$ ) while direct MTS reduction at the substrate surface yielded elemental Si and C reacting to form SiC matrix. Hopfe et al. (1995) studied MTS decomposition in a hot-wall reactor at 1000°C with FTIR (Fourier Transform-Infrared) spectroscopy. The major intermediate species that were detected included MTS ( $\text{CH}_3\text{SiCl}_3$ ),  $\text{SiCl}_2$ ,  $\text{SiCl}_3$ ,  $\text{SiCl}_4$ ,  $\text{SiHCl}_3$ ,  $\text{CH}_4$ ,  $\text{CH}_3\text{Cl}$ , and  $\text{HCl}$ , agreeing with the results observed by Schlichting.

Allendorf et al. (1994) conducted MTS thermal decomposition studies in a cold-wall, high temperature flow reactor. The dominant decomposition products detected by mass spectrometry were  $\text{CH}_4$ , and  $\text{HCl}$  while no chlorosilanes were observed. The chlorosilanes were not detected due to adsorption at the cold-wall. Hydrogen was found to enhance the thermal decomposition of MTS. They also concluded that the dominant initiation step in the MTS decomposition pathway was the fission of the Si-C bond ( $\text{CH}_3$  and  $\text{SiHCl}_3$ ) with some direct 1-2 HCl elimination ( $\text{H}_2\text{C}=\text{SiCl}_2$  and  $\text{HCl}$ ).

These citations concluded that separate siliconaceous species and carbonaceous species were formed due to the Si-C bond fission when the MTS experienced sufficient residence time in the reactor. However, the detection of the chlorosilanes was dependent on the reactor type, for cold-wall decomposition studies favored chlorosilane adsorption at the wall. The prevalent, detected intermediate gas species are now compared to those determined by thermodynamic equilibrium calculation.

### Thermodynamic Calculations

Kington et al. (1983) conducted thermodynamic calculations of SiC CVD phase diagrams with a Si-C-H element system and a Si-C-H-Cl element system concluding that the latter was more complex due to the addition of Cl. The process conditions that were required to deposit SiC with the Si-C-H system were very different than those needed with the Si-C-H-Cl system, suggesting that careful control of temperature, pressure, and concentrations of the carrier and the precursor was necessary to deposit  $\beta$ -SiC in a single phase.

Fischman and Petuskey (1985) conducted thermodynamic equilibrium calculations for a Si-C-H-Cl system at atmospheric pressure and at several temperatures between 1473 K and 1700 K. The general conclusion at all temperatures was that silicon chlorides ( $\text{SiCl}_x$ ) and chlorosilanes ( $\text{H}_x\text{SiCl}_{4-x}$ ) were the most common siliconaceous species while  $\text{CH}_4$  and  $\text{C}_2\text{H}_2$  were the most prevalent carbonaceous species. These thermodynamic calculations were compared to experimental results, with large disagreement seen at 1473 K and

at 1600 K. Fischman and Petuskey concluded that the Si deposition occurred faster than the C deposition on the given substrate because the siliconaceous species have higher sticking probability on polar Si and SiC surfaces due to their non-polar character.

### **SiC Deposition Kinetics from MTS**

Van Kemenade and Stemfoort (1972) studied the SiC deposition kinetics from MTS at atmospheric pressure by variation of the temperature and the MTS flow, with the SiC deposited on suspended graphite rods. An apparent activation energy of 68 kJ/mol was determined from measurement of radial growth rates, and a much lower, peculiar, apparent activation energy of  $-75$  kJ/mol was determined from measurement of the deposit weights. At higher temperatures ( $\sim 2000^{\circ}\text{C}$ ), free carbon deposit was found on the graphite substrates.

They observed that if an equivalent amount of SiC was calculated from the free carbon deposit and its weight added to the existing SiC deposit weight, the activation energy extracted from the radial growth rate data agreed with the activation energy extracted from deposit weight gain data. The primary reason for the discrepancy between the two rate measurements was attributed to the significant MTS depletion in the gas phase, which favored the poisoning of the substrate surface with HCl by-product.

Burgess and Lewis (1974) examined the initial step in the MTS thermal decomposition by infrared analysis of the evaporation of the frozen decomposition gaseous product. At  $750^{\circ}\text{C}$ , only 7% of the MTS was

decomposed while at 850°C, the decomposition increased to approximately 90%. Variation of the MTS partial pressure at 730°C led to constant  $\text{SiHCl}_3/\text{MTS}$  ratio in the frozen gaseous product, indicating a first-order reaction rate dependence in MTS. An activation energy of 336 kJ/mol was determined for the MTS thermal decomposition.

Brennfleck et al. (1984) investigated the SiC deposition kinetics with MTS precursor using a hydrogen/MTS ratio of 3.6 and atmospheric pressure. Their results demonstrated a first-order kinetic relationship in MTS partial pressure with an apparent, activation energy of 120 kJ/mol.

Besmann et al. (1991) considered SiC deposition on Nicalon™ fibers by CVI with MTS in hydrogen. The Nicalon™ fibers that constitute a given fiber bundle were sufficiently spaced to eliminate fiber contact and to prevent discrepancy in SiC radial growth rate measurement. A 0.2  $\mu\text{m}$ -carbon coating was applied to the fibers prior to SiC deposition to simulate the CVI of carbon-coated fibrous preforms. They observed that the SiC deposition rate strongly depended on the degree of MTS thermal decomposition and that HCl severely suppressed the SiC deposition rate. The apparent MTS reaction order in the proposed SiC deposition rate translated from first-order to zeroth-order with high depletion (high HCl content). The HCl inhibition in the SiC deposition rate was less pronounced at higher temperatures ( $\sim 1200^\circ\text{C}$ ).

Josiek and Langlais (1996) was interested in the effect on MTS residence time on the SiC deposition kinetics. For low MTS residence times, the SiC deposition rate depended strongly on the reactor temperature and the total flow

rate. At higher residence times, the SiC deposition rate became independent of both temperature and the residence time, yielding an apparent activation energy of approximately 200 kJ/mol. At short MTS residence times, the thermal decomposition was low and forced the SiC deposition rate to depend on MTS heterogeneous reaction at the substrate surface while at higher MTS residence times, the SiC deposition depended on MTS decomposition in the gas phase.

Papasouliotis and Sotirchos (1998) observed multiple, steady-state SiC deposition rates with MTS in a hot-wall reactor, where the observed rate depended on the schedule in which the reactor was brought to equilibrium. With no HCl in the feed stream, a hysteresis in the deposition rate was seen at a small temperature interval around 850°C, alternating between a high ( $10^{-1}$  mg/cm<sup>2</sup> min) deposition rate and a low ( $10^{-3}$  mg/cm<sup>2</sup> sec) deposition rate. As the reactor temperature was slightly lowered from 850°C, the observed deposition rate switched to the low rate while subsequent increase in the reactor temperature suddenly favored the occurrence of the higher deposition rate. Higher reactor pressures and HCl gas phase content forced the observed hysteresis to occur at higher temperatures. The observed deposition rate depended on the flow rate and on the position in the reactor. They concluded that the primary reason for the observed rate multiplicity was most likely a chemical effect, for the HCl, siliconaceous species, and the carbonaceous species competed for substrate adsorption.

The deposit that was observed with the low deposition rate consisted primarily of amorphous carbon while the deposit seen at the high deposition rate

was  $\beta$ -SiC. The carbon deposit seen with the low deposition rate was attributed to poor substrate adsorption of the siliconaceous species, caused by high MTS depletion. They concluded that the occurrence of the multiple steady-states may be the reason for the disagreement in the SiC deposition kinetics seen in the literature.

Lackey et al. (1998) considered SiC deposition from MTS onto a moving Nicalon™ fiber tow. Silicon carbide deposition rates between 0.3 and 3.7  $\mu\text{m}/\text{min}$  were observed at 1250°C with various hydrogen flow rates and a constant, hydrogen/MTS molar feed ratio (10). The MTS efficiency decreased with the increase in total flow rate indicating that a lower MTS residence time had a greater effect on the SiC deposition rate than did the increase in the MTS mass transport to the fiber surface. They noticed that the MTS efficiencies for SiC deposition with a moving fiber tow were higher than the efficiencies seen for a stationary tow due to the disruption of the boundary layer.

Chiang (1999) studied SiC deposition kinetics using CVI with MTS precursor. A hydrogen/MTS gas mixture was infiltrated through an array of 400  $\mu\text{m}$ -diameter parallel pores drilled through a graphite cylinder. Silicon carbide deposition was performed at 1100°C, 1150°C, and 1200°C using either a total flow of 100 sccm or 300 sccm and a constant, hydrogen/MTS molar feed ratio (10). The SiC-infiltrated graphite cylinder was then sliced at several different axial positions, with the cross-sections photographed with SEM. The SiC deposition rates were extracted from the SEM micrographs by measurement of the SiC deposit in each of the pores.

The proposed SiC deposition rate law used to fit the experimental SiC growth rate data involved a first-order rate dependence in MTS concentration and a first-order rate dependence in HCl concentration, characterizing HCl inhibitive effects. The use of this proposed SiC deposition rate law was successful for predicting the experimental SiC growth rates along the cylinder length at 1150°C and 1200°C, but overestimated the growth rates observed at 1100°C.

These investigators have looked into the kinetics of the SiC matrix deposition from MTS by considering variation in temperature, pressure, and flow rate (residence time). The general conclusions suggested that the SiC deposition kinetics are not a simple, first-order in MTS concentration (partial pressure). The variation in the SiC deposition rate from MTS thermal decomposition was influenced by the variation in the reactor temperature, reactor type, and substrate position.

The residence time of the MTS in the experimental reactor also had a substantial effect on the apparent SiC deposition rate. Low MTS residence times resulted in heterogeneous adsorption and reaction at the substrate surface. High MTS residence time allowed for decomposition into separate siliconaceous and carbonaceous species, with the SiC deposition rate limited by the substrate adsorption of the carbonaceous specie (most likely  $\text{CH}_4$ ). The MTS depletion effect had a substantial inhibitive effect on the SiC deposition rate at moderate infiltration temperatures (700-1000°C), however the HCl inhibition was less pronounced at higher temperatures (~1200°C).



## **Composite Transport Properties**

This section discusses cited references that deal with either the modeling or the experimental measurement of the evolving, density-dependent composite transport properties. The composite transport properties considered include specific surface area, effective diffusion coefficient, permeability, and thermal conductivity, which affect all pertinent conservation balances defined in any given CVI model.

### **Specific Surface Area**

Bhatia and Perlmutter (1980) and Currier (1990) used a one-dimensional, random overlap cylindrical fiber array to model the specific surface area of fiber bundles, using specific pore geometric parameters and random distribution in the fiber diameter. The initial specific surface area was determined assuming no adjacent fiber surface contact. The fiber surface area expanded in the radial direction due to matrix deposition and eventually made contact with neighboring fiber surfaces. The overlap caused by the consolidation of adjacent fiber surfaces was taken into consideration and subtracted from the total calculated fiber surface area. Conclusions found by Avrami (1940) in a one-dimensional random, cylindrical arrangement were implemented, stating that the change in the overlapped cylinder volume was proportional to the change in the analogous non-overlapped cylinder volume ensemble.

The resulting specific surface area function could possess a maximum at the initial stages of matrix deposition (fiber surface advancement) with certain

configurations of the pore structure. The depicted maximum agreed with specific surface area estimation in a fiber bundle using Monte-Carlo techniques (random walk) (Starr 1988). However, the theoretical density at which the maximum is observed is low, making this artifact have a negligible effect on long-term density prediction in the CVI model.

Starr (1995) developed a specific model that simulated the evolving, specific surface area of a fibrous preform with characteristic, multi-modal pore microstructure. This surface area simulation included the use of spherical nodes and cylindrical bonds, where the bonds intersected the nodes in two dimensions (radial and axial). The radii, length, and number of the axial and radial cylindrical bonds and the spherical nodes in a given unit pore volume approximated the dimensions of the physical, bimodal microstructure of the preform porosity. The specific surface area monotonically decreased as the radii for the nodes and bonds decreased uniformly. This specific surface area model can then be incorporated into any given CVI model to describe any particular fibrous preform.

Many cylindrical bonds in the axial direction ( $\sim 1200$ ) with a small initial radii ( $\sim 7 \mu\text{m}$ ) represented the intrabundle preform porosity while the spherical node radius ( $\sim 1 \text{ mm}$ ) and radial cylindrical bond radius ( $\sim 0.5 \text{ mm}$ ) represented the interstitial channel and interlaminar preform porosity in a typical, two-dimensional fiber weave. Statistical distributions were incorporated for the radii and lengths of the axial and radial cylindrical bonds and radius of the spherical node, representing actual variation in the different phases of the preform porosity.

Although results from Currier (1990) and Bhatia and Perlmutter (1980) demonstrated initial increase in surface area with increase in density, Starr's node/bond model (1995) gave a monotonic decrease in surface area until the intrabundle porosity was consumed. At this point, a low specific surface area resulted for the interstitial channel porosity and the interlaminar porosity, with a low rate change with density until complete densification was reached.

### **Effective Diffusion Coefficient**

Several investigators have calculated the effective diffusion coefficient in various structured, isotropic pore geometries. Perrins et al. (1979) calculated conductivities for hexagonal and square cylinder arrays, with the conductivities for the square array being slightly higher. The conductivity was a measure of the geometric pore structure factor, which was analogous to the effective diffusion coefficient. Sotirchos and Burganos (1988) developed models of porous networks using effective medium theory and smooth field-approximation to calculate the effective diffusion coefficient. Their results showed that use of the smooth field-approximation underestimated diffusional resistance while the results from effective medium theory provided a more realistic approximation.

Sotirchos and Zarkanitis (1993) then attempted to use percolation theory to describe evolving pore networks (Bethe lattice, Stauffer and Aharony 1992). A Bethe lattice is a pore network defined by a specific coordination number, referring to the number of pores that emanate from a specific node. This structure continues indefinitely with the pores not reconnecting with the same

node (Cayley tree, Stauffer and Aharony 1992). Distribution in pore size and length influenced the calculated results of the effective diffusion coefficient, where lower coordination number yielded lower coefficients and broader pore distributions yielded lower effective diffusion coefficients by shifting the pore number density to smaller pore dimensions.

Tomadakis and Sotirchos (1993) used Monte Carlo (random walk) simulation to estimate the effective diffusion coefficients in one-dimensional, two-dimensional, and three-dimensional random pore networks. The calculated effective diffusion coefficients for the two-dimensional and the three-dimensional pore networks were slightly higher perpendicular to gas diffusion than the effective diffusion coefficients calculated parallel to gas diffusion. Calculated effective diffusion coefficients for all considered random pore networks were in reasonable agreement with results determined by other investigators (Tsai and Streider 1986, Klemens 1990).

These cited works predicted the change in the effective diffusion coefficient with different assumed random and structured pore networks. The results from the model predictions can be utilized in any CVI model without much difficulty. However, the most sensible method of determining the transient, physical functionalities of actual preform transport properties is by the utilization of experimental methods.

## Experimental Property Measurement

Starr and Hablutzel (1998) constructed an experimental apparatus used to measure the permeability and the effective diffusion coefficient in composite specimens of varied density and fiber orientation. Permeability measurement was conducted by recording pressure drop data and flow rate data across the specimen thickness. The permeability value was extracted from the resulting slope from linear regression of the experimental pressure drop data and the corresponding flow rate data.

The effective diffusion coefficient measurement was conducted by flow of a 10% CH<sub>4</sub>/He mixture across one specimen surface and by flow of pure He across the other specimen surface at varied pressure differentials. Gas chromatography was used to detect the amount of CH<sub>4</sub> that diffused through the specimen. The CH<sub>4</sub> diffusivity through the specimen was extracted from plotting the quantity of CH<sub>4</sub> detected versus the specimen pressure differential (extracted diffusivity at zero pressure differential). The effective diffusion coefficient was found by dividing the extracted CH<sub>4</sub> diffusivity by the CH<sub>4</sub> binary molecular diffusivity in He.

Only one citation was found for thermal conductivity evaluation of fiber-reinforced ceramic composites. Tawil et al. (1985) conducted laser-flash thermal diffusivity measurements on Nicalon™/SiC and C/SiC composite specimens of varied density with surfaces parallel and perpendicular to fiber orientation. The laser-flash method involved a laser flash on one specimen surface while the specimen temperature of the other surface was recorded. The calculation of the

thermal diffusivity involved the half-rise time of the rear specimen surface temperature and the specimen thickness. The thermal conductivity was determined from the thermal diffusivity data with knowledge of the temperature and density dependence of the composite heat capacitive function ( $\rho C_p$ ).

The composite thermal diffusivities increased with increase in density and monotonically decreased with increase in temperature for both Nicalon™/SiC and C/SiC composites. The thermal diffusivities measured parallel to fiber orientation were approximately two to three times greater than those measured perpendicular to fiber orientation. A permanent increase in the SiC matrix grain size resulted in higher thermal diffusivity for both fiber orientations in both composite systems at temperatures beyond 1200°C and 1500°C respectively.

## CHAPTER 3

### FCVI EXPERIMENTAL METHODS

This section describes the experimental methods used in the fiber-reinforced ceramic composite tube fabrication by the FCVI process, which include the fibrous tube preform fabrication and assembly, furnace assembly, experimental FCVI procedure, and post-FCVI handling. The experimental procedures used in the tube density characterization and the preform transport property measurements are also described in this chapter.

#### **Tube Preform Fabrication**

The fibrous tube preforms were fabricated using collapsible, braided tubular sleeves of Nextel™ 312 fiber (3M Corporation, Saint Paul, MN). Nextel™ 312 is an aluminoborosilicate fiber suitable for use at temperatures up to 1200°C. The stretched Nextel™ 312 fiber sleeve diameter was approximately 5 cm.

The characteristic fiber braid shown in Figure 3-1 consists of a satin weave with large channels (~1-3 mm) that exist at the fiber bundle interstices. Each fiber bundle group consists of three smaller fiber bundles, each containing about 500 Nextel™ 312 fibers. The physical characteristics and the constituent weight percents of the Nextel™ 312 fiber are provided in Table 3-1. The actual

composition of the Nextel™ 312 fiber consists of a ternary mixture of  $\text{Al}_2\text{O}_3$ ,  $\text{SiO}_2$ , and  $\text{B}_2\text{O}_3$ .

Table 3-1. Nextel™ 312 Fiber Composition

Alumina ( $\text{Al}_2\text{O}_3$ )	62 wt. %
Silica ( $\text{SiO}_2$ )	24 wt. %
Boria ( $\text{B}_2\text{O}_3$ )	14 wt. %
Fiber Diameter	11 $\mu\text{m}$
Cross Section	Ovoid

### Preform Lay-Up

Eleven Nextel™ 312 fiber sleeve lengths were required to achieve a tube preform with approximately 40% fiber volume with the desired preform thickness (6.4 mm). Each sleeve length was cut from the supplied sleeve roll with a pair of scissors. Prior to fiber sleeve application, wax paper was wrapped around a 5 cm-diameter, high-density polyethylene (HDPE) cylindrical mandrel and fixed at both ends with masking tape. The purpose of the wax paper was to facilitate preform removal after the resin curing stage, which is described later in this section.

The eleven sleeve lengths were applied concentrically and stretched over the HDPE mandrel. The mandrel OD dictated the tube preform ID. Each additional sleeve length that was applied to the mandrel was slightly longer, compensating for the increasing preform diameter. Each applied fiber sleeve was fixed to one mandrel end with masking tape. The desired tube preform dimensions and initial fiber volumes are given in Table 3-2. A Nextel™ 312-fiber sleeve length schedule used for a typical tube preform is provided in Table 3-3.

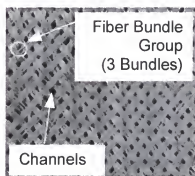


Table 3-2. Tube Preform Data

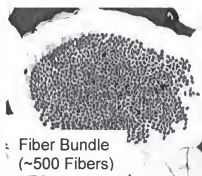
Fiber Type	Nextel™ 312
Fiber Volume	40%
Concentric Sleeve Count	11
Inside Diameter	5.0 cm
Outside Diameter	6.4 cm
Length	35.6 cm

Table 3-3. Nextel™ 312 Fiber Sleeve Length Schedule

Sleeve 1	40.6 cm	Sleeve 7	46.4 cm
Sleeve 2	41.9 cm	Sleeve 8	47.3 cm
Sleeve 3	43.2 cm	Sleeve 9	48.3 cm
Sleeve 4	43.8 cm	Sleeve 10	49.5 cm
Sleeve 5	44.1 cm	Sleeve 11	51.4 cm
Sleeve 6	45.1 cm		



(a)



(b)

Figure 3-1. The physical characteristics of the Nextel™ 312 braided sleeve.

a) Characteristic braid pattern of the Nextel™ 312 tubular sleeve used in the tube preform fabrication; b) An individual, fully infiltrated fiber bundle of the Nextel™ 312 fibers.

### Phenolic Resin Application

A rigidizing step was performed so that the concentric fiber sleeves retained a rigid, cylindrical shape for subsequent furnace fixturing. The tube preform rigidization step involved application of Borden Durite™ SC-1008 phenolic resin (Borden Chemical Corporation, Louisville, KY).

A given amount of Borden Durite™ SC-1008 phenolic resin (actual amount proprietary to the 3M Corporation) was mixed with methanol and the resulting solution was applied to the preform while in continuous rotation. The methanol in the solution also washed away the polyvinyl acetate sizing placed on the Nextel™ 312 fibers during manufacturing. The continuous preform rotation enabled the phenolic resin to seep uniformly throughout the fibrous preform volume. A custom motor and mandrel fixturing were used to rotate the preform.

### **Preform Compression**

The resin-impregnated Nextel™ 312 fiber sleeves were compressed using two different methods. One method involved the use of a cylindrical sleeve made of Dow J RTV Silastic™ silicone rubber (Dow Corning Corporation, Midland, MI) and the other method involved the use of two aluminum tube sections. The desired tube preform OD was 6.4 cm.

Preparation of the Silastic™ compression sleeve involved a 9:1 part Dow J RTV Silastic™ silicone rubber/curing agent mixture. The mixture was poured into an annulus formed by two vertical, concentric aluminum tubes. Vulcanization of the Silastic™ silicone rubber occurred within 24 hours. After vulcanization, the sleeve was sliced through the thickness along the entire length and was removed from the tube assembly. The fabricated sleeve dimensions were 6.4 cm in ID, 6.4 mm in thickness, and 61 cm in length.

The other compression technique involved the use of a 6.4 cm-ID aluminum tube. The aluminum tube was sliced into two sections along the tube

length through the diameter. The two tube section dimensions were 3.2 cm in ID, 6.4 mm in thickness, and 45.7 cm in length.

Both compression techniques did not completely contain the Nextel™ 312 sleeve assembly. The silicone rubber compression sleeve almost completely wrapped around the Nextel™ 312 sleeve assembly, leaving a 0.6 cm-gap along the length. The Nextel™ 312 sleeve assembly was sandwiched between the two aluminum tube sections leaving two 0.6 cm-gaps on both sides of the assembly. The gaps needed to be eliminated to reach the desired preform OD (6.4 mm). Both sleeve assemblies were compressed with the use of swivel-lock hose clamps.

Ten to twelve hose clamps were placed around each sleeve assembly and uniformly spaced along the sleeve length, with the clamp heads aligned 90° from the compression sleeve gap. The hose clamps were tightened from the fixed preform end (end with masking tape) to the free preform end with a 0.8 cm-hex nutdriver. Once the hose clamps were hand-tight, the clamps were further tightened from the fixed preform end to the free preform end with an electric screwdriver.

Thin aluminum shim stock strips were placed underneath the gaps between the sleeve and preform for each sleeve assembly. The strips were used to prevent the preform from buckling through the gaps upon compression with the hose clamps. The aluminum shim stock dimensions were 0.1 mm in thickness, 3.8 cm in width, and 45.7 cm in length. Vacuum grease (Dow Corning Corporation, Midland, MI) was applied on both shim stock strip surfaces to

reduce the friction that occurred between the compression sleeve and the aluminum shim during hose-clamp tightening.

An alternate solution to preform buckling upon compression was the use of an aluminum bar stock. The aluminum bar stock was only used with the Silastic™ sleeve. A rectangular aluminum bar 0.6 cm in height, 1.2 cm in width, and 30.5 cm in length was placed in the Silastic™ sleeve gap prior to hose clamp-tightening.

### **Preform Curing**

After preform compression, the compressed Nextel™ 312 fiber sleeve assembly underwent a specific proprietary heating schedule in air at atmospheric pressure in a conventional oven. The heating cured the phenolic resin that impregnated the Nextel™ 312 sleeves, leaving a rigid, cylindrical preform capable of furnace fixturing. After the resin curing stage, both tube preform ends were sliced with a utility knife, resulting in a tube preform length of 36 cm. The tube preform was then ready for FCVI furnace assembly.

### **Tube Preform Assembly**

Figure 3-2 displays the end projection and the cross-section of the tube preform assembly. A 1.3 cm-OD 316 stainless steel-cooling line was placed inside the tube preform, and a 0.7 cm-OD 316 stainless steel-gas injector line was taped to the cooling line with electrical tape. The injector line end was

placed 9 cm from one preform end. The cooling line was key to the establishment of the temperature gradient across the preform thickness by forcing radiation loss at the tube preform interior.

The tube preform ends were sealed with Fiberfrax™ (Carborundum Company, Niagara Falls, NY) insulation. Two Fiberfrax™ disks, 5 cm in diameter and 1.2 cm in thickness, were used to seal each preform end. The disks were punched from Fiberfrax™ panels with a hammer and a gasket puncher. Concentric holes were punched through the Fiberfrax™ disks for the injector line and the cooling line. The disk peripheries were sealed to the tube preform interior with Aremco™ graphite glue (Valley Cottage, NY), and several hours were necessary to allow proper setting of the graphite glue.

\* *Graphic not to scale*

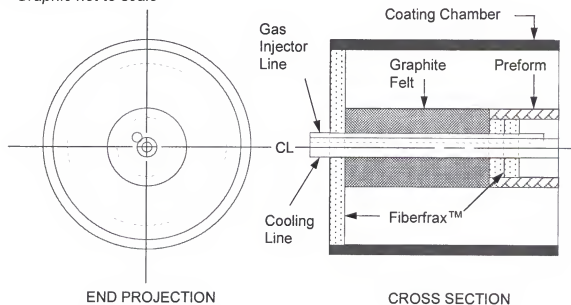


Figure 3-2. Tube preform assembly for FCVI.

The preform assembly was then placed inside a cylindrical graphite coating chamber, 13 cm in OD and 3.2 mm in thickness. Stacks of Polycarbon (Valencia, CA) graphite felt disks, 6.5 cm in diameter, were placed outside both preform ends to provide insulation. The preform-loaded coating chamber was sealed at the gas inlet end with a Fiberfrax™ disk, 12.8 cm in diameter and 1.2 cm in thickness, and Aremco™ graphite glue. The coating chamber gas exhaust-end was loosely fitted with a Fiberfrax™ disk with several holes.

This chamber configuration contained the reactant and effluent gases and directed these gases to the furnace exhaust. The configuration also prevented SiC deposition on the graphite heating element. A tube preform, along with the graphite coating chamber and associated components, is seen in Figure 3-3.



Figure 3-3. Tube preform, cooling and gas injector lines, Fiberfrax™, graphite felt, and coating chamber used in the FCVI tube preform assembly.

## FCVI Apparatus

A schematic of the FCVI experimental apparatus is shown in Figure 3-4. Liquid methyltrichlorosilane ( $\text{CH}_3\text{SiCl}_3$ , MTS) and hydrogen were the chosen precursor and diluent for silicon carbide (SiC) deposition. Hydrogen and liquid MTS were fed separately into a heat-jacketed vaporizer. The hydrogen flow was controlled with a MKS 5000-sccm standard mass flow controller (Andover, MA). Liquid MTS was contained in a cylindrical, stainless steel reservoir and was delivered to the vaporizer with a Cole-Parmer peristaltic pump (Vernon Hills, IL). The desired liquid MTS flow rate was verified by a scale placed underneath the MTS reservoir.

The temperature of the heat-jacketed vaporizer was kept around  $130^\circ\text{C}$ , well above the normal boiling point of MTS ( $65.3^\circ\text{C}$ , Weast 1995). This enabled the liquid MTS to flash to the vapor phase. The vaporizer volume ( $\sim 2000\text{ cm}^3$ ) was sufficiently large to ensure complete mixing of the hydrogen and MTS.

The well-mixed hydrogen/MTS mixture exited the vaporizer through a stainless steel-gas injector line, 0.7 cm in OD, which led to the tube preform assembly in the FCVI furnace. A MKS 133 kPa-Baratron pressure transducer (Andover, MA) was placed in the gas injector line path prior to the furnace entry to monitor the transient preform inlet backpressure. This gas injector line was wrapped with heating tape, from the vaporizer to the furnace, and its temperature was maintained between  $85\text{--}95^\circ\text{C}$  to prevent MTS condensation prior to the

furnace entry. Vaporizer and gas injector line temperatures were regulated with Variac® power controllers (Stark Electronics, Worcester, MA).

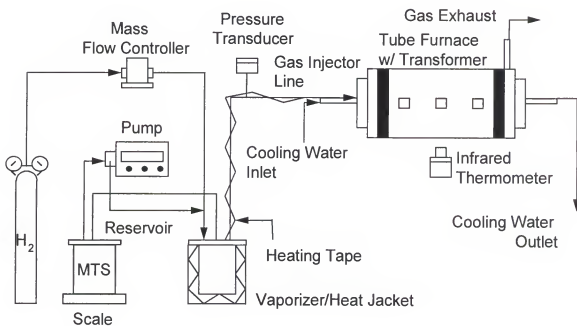


Figure 3-4. Schematic of the FCVI tube experimental apparatus.

The FCVI furnace used a graphite heating element that was enclosed by a water-jacketed, aluminum shell. The furnace shell was designed and constructed by American Furnace Company (Knoxville, TN). Furnace outer dimensions were 35.6 cm in height, 35.6 cm in width, and 72.4 cm in length. Copper electrodes 35.6 cm in height, 35.6 cm in width, and 3.8 cm in thickness were placed at each furnace end. Aluminum endplates of the same dimensions were situated outside the copper electrodes. A smaller aluminum endpiece, 24.1 cm in height, 24.1 cm in width, and 5.1 cm in thickness, was placed outside the aluminum endplate on the gas exhaust side to allow the removal of the preform



assembly. Three glass sight ports were located on one side of the furnace shell to allow for coating chamber temperature measurement by infrared thermometry.

An electrical transformer, with a 72 kVA-rating (Neeltran Inc., New Milford, CT), provided the necessary power to the cylindrical, graphite heating element. The transformer was capable of delivering 6000 A at 12 V with 100% output. Water-cooled copper bus bars, 4 cm in width, connected the transformer power to the copper electrodes.

The cylindrical graphite heating element was 69.9 cm in length, 15 cm in ID, and 1.6 cm in thickness (Figure 3-5). Since the element electrical resistivity was low ( $10^{-3} \Omega\text{-cm}$ , Poco Graphite, Inc., Decatur, TX), a high amperage was necessary to achieve adequate infiltration temperature ( $1200^{\circ}\text{C}$ ). The typical current and voltage supplied to the heating element were 4500 A at 8 V (~50% transformer output). Slots were cut at the heating element ends to increase the electrical resistance locally and to reduce temperature nonuniformity along the furnace length. The heating element ends made sufficient contact with the copper electrodes placed on both furnace ends.

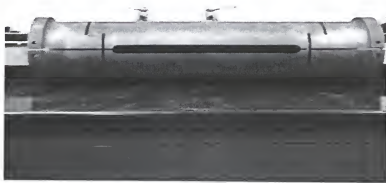


Figure 3-5. Cylindrical graphite heating element used in the FCVI furnace.

## FCVI Procedure

Figure 3-6 illustrates the gas infiltration through the tube preform assembly. The hydrogen/MTS gas mixture entered the assembly through the gas injector line. The gas mixture filled the preform interior gas space, infiltrated through the preform, and exited at the gas exhaust. The Fiberfrax™ disks used to seal both tube preform ends prevented the reactant gas mixture from exiting the tube preform ends. The tube preform exterior was heated by radiation emanating from the graphite heating element and the interior was cooled by radiation losses forced with the concentric cooling line (water at 50°C).

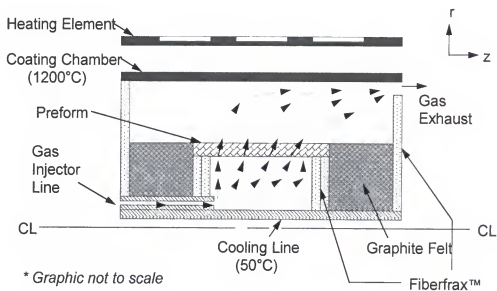


Figure 3-6. Cross-section of the tube preform assembly. Arrows indicate the gas pathway.

The first step of the FCVI infiltration was furnace evacuation. A Kashiyyama 5040V II screw-dry vacuum pump (Tokyo, Japan) evacuated the tube

furnace to an approximate pressure of 11 kPa. This vacuum was limited by the gasket seals placed at the gas injector line and at the outlet aluminum endpiece. The vacuum was typically kept overnight prior to furnace start-up. The furnace was brought back to atmospheric pressure with approximately 3 slm of Ar purge (Air Liquide, Knoxville, TN, 99.985% purity). Cooling water was then supplied to the furnace shell and the cooling line, and the transformer output was initially set at approximately 50%.

The hydrogen flow was turned on when the coating chamber mid-line temperature reached 1000°C. The power output was then gradually increased to 80%. After the chamber mid-line temperature reached 1200°C, the furnace conditions were held constant for 20 minutes, with the hydrogen flowing, to permit thermal equilibrium. After the 20 minute-duration, the MTS reservoir valves were opened and the peristaltic pump was turned on.

The weight loss in the MTS reservoir was carefully monitored during the first hour of infiltration. The pump flow rate setting was periodically adjusted to obtain the desired MTS liquid feed rate (calculation found in Appendix D). The outer coating chamber wall temperatures were measured with an Ircon Ultimax™ Infrared Thermometer (Niles, IL) at three, equidistant sight ports located at the side of the FCVI furnace. The sight port positions directly coincide with the middle and both end-section lengths of the tube preform. The infrared signal passed through a prism and a quartz glass piece, 0.6 cm in thickness, prior to reaching the coating chamber.

Tube infiltration continued until either a 70 kPa-gas inlet backpressure was measured with the Baratron™ pressure transducer or until a specific infiltration time was reached. After the MTS flow was terminated, the hydrogen flow was continued for an additional five minutes before the transformer power was shut off. The furnace cool-down time to room temperature was approximately two hours.

### **Equipment Calibration**

Both the MKS mass flow controller and the Ircon Ultimax™ Infrared Thermometer were calibrated periodically. This ensured that the observed temperatures and the hydrogen flow rates were accurate in experiment.

The MKS mass flow controller was calibrated with a standardized wet-test meter. The desired hydrogen mass flow rate was fixed by the set point and by the gauge factor adjustment located on the mass flow meter controller. The gauge factor was adjusted until the mass flow meter reading matched the wet-test meter reading.

The Ircon Ultimax™ Infrared Thermometer was calibrated with several metal sample standards at their known melting temperatures. The emissivity on the thermometer was adjusted so that its measurement matched a calibrated infrared thermometer measurement of a known metal melting temperature.

Infrared signal losses were estimated in the prism and the three glass sight port pieces. The signal losses in each piece were found with the use of a calibrated infrared thermometer and the metal sample standards. The infrared

measurement through each glass piece and prism was compared to the actual metal sample temperature.

The estimated average infrared-signal losses at 1100°C for both the glass sight port pieces and the prism were 6.7°C and 16.0°C, respectively, making the total signal loss from both components 22.7°C. Therefore, the actual temperature was 22.7°C higher than that provided by the infrared thermometer.

### **Post-FCVI Procedure**

After densification, the tube was removed through the furnace outlet end by the removal of the free aluminum endpiece. The removal was not performed until the furnace thermocouple placed outside the heating element displayed a temperature below 100°C. After preform assembly removal, the Fiberfrax™ disk that sealed the inlet side of the coating chamber was removed from the coating chamber with a utility knife. The loose Fiberfrax™ disk at the coating chamber outlet end was removed, along with the graphite felt disks placed outside both preform ends.

The Fiberfrax™ disks that sealed the preform ends densified with SiC matrix near the preform seal. The Fiberfrax™ disk sections near the cooling line and the gas injector line, however, were not densified with SiC due to their lower temperature. This aided the removal of the cooling line and the gas injector line from the densified tube. These uninfiltated Fiberfrax™ sections were removed with a utility knife.

The final composite tube length was achieved by slicing 5 cm-sections from each tube end. This was done with a Bridgeport Harig® 618 Slicer/Grinder (Bridgeport, CT). Occasionally, SiC would deposit on the tube preform exterior. In the occurrence of this event, excess SiC was machined from the tube exterior with a Weldon AGN4 Automated Grinder (York, PA).

### **Preform Transport Property Measurement**

Composite specimens of varied density and fiber orientation were fabricated for the determination of the density-dependence and the fiber orientation-dependence on the composite thermal conductivity and permeability. Composite thermal conductivity was calculated from laser-flash thermal diffusivity data while the composite permeability was determined from specimen pressure drop data and total flow data measurements. These transport property data were input into a comprehensive CVI model that attempted to predict the transient tube infiltration with the FCVI process.

### **Composite Specimen Preparation**

Nextel™ 312/SiC composite specimens were prepared from infiltrated cylindrical Nextel™ 312 disk preforms, 1.2 cm in thickness with 40% fiber volume. The preforms were prepared using 22 Nextel™ 312 fiber disks, 4.5 cm in diameter. The disks were stacked and fixed in a graphite holder, and subsequently infiltrated by the FCVI process in a vertical, resistive heating furnace with hydrogen and MTS (Stinton et al. 1986). The gas exhaust-side of

the graphite holder was heated by radiation while the gas injector side was directly cooled with a water-cooled, stainless steel-gas injector.

Two Nextel™ 312 disk preforms were infiltrated using 0.3 g/min of liquid MTS precursor (50 sccm MTS in the vapor phase) and 500 sccm of hydrogen, at a preform hot-surface temperature of 1200°C and preform temperature gradient of 200°C/cm. The total infiltration times for the two disk preforms were 10 and 20 hours, respectively. The dense Nextel™ 312/SiC disk preforms were removed from the graphite holder with a conventional lathe.

Square Nextel™ 312/SiC composite specimens were sliced from the infiltrated disk preforms with the Bridgeport Harig® 618 Slicer/Grinder. The prepared specimen dimensions were 1.2 cm in length, 1.2 cm in width, and 2 mm in thickness. The square specimen faces were sliced congruent to both Nextel™ 312 fiber orientations (perpendicular and parallel) (Figure 3-7). The specimen theoretical densities varied between 60-80% as determined from initial fiber volume and final composite mass.

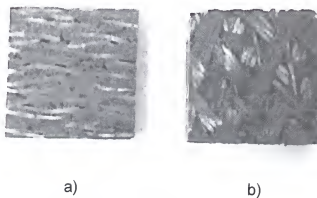


Figure 3-7. Nextel™ 312/SiC composite specimens.

a) parallel to fiber orientation; b) perpendicular to fiber orientation.

### **Laser-Flash Thermal Diffusivity Measurement**

The Nextel™ 312/SiC thermal conductivity data used in the comprehensive CVI model were evaluated from thermal diffusivity measurements using a laser flash-method, for data could be taken over a large temperature range (100–1200°C). Laser-flash thermal diffusivity measurements were performed on Nextel™ 312/SiC composite specimens at varied density for both fiber orientations (perpendicular and parallel). These laser-flash thermal diffusivity measurements were performed at the Thermophysical Properties User Center at the Oak Ridge National Laboratory.

The laser-flash thermal diffusivity unit (Wang et al. 1996) consisted of a graphite furnace, multiple specimen carousel, Flashline™ 5000 Nd:Glass Laser Module, and photovoltaic infrared detectors, and was assembled by Anter Corporation (Pittsburgh, PA). The specimen carousel had a holding capacity of six specimens. In the thermal diffusivity measurement, the laser was fired at one specimen surface and the temperature response at the other surface was continuously monitored with an infrared thermometer with the resulting data recorded.

The thermal diffusivity was calculated using the specimen thickness and the half-rise time of the rear surface temperature (Equation 3-1). The parallel laser-flash thermal diffusivity measurements were performed with a graphite disk, 0.3 mm in thickness placed on top of the Nextel™ 312/SiC composite specimen, to prevent direct contact of the laser flash with the photovoltaic detector (large Nextel™ 312/SiC composite specimen pores, Figure 3-7).



$$\alpha = \frac{\tau_{\text{Specimen}}^2}{t_{1/2}} \quad (3-1)$$

where  $\alpha$  = thermal diffusivity [ $\text{cm}^2/\text{sec}$ ]  
 $\tau_{\text{Specimen}}$  = specimen thickness [cm]  
 $t_{1/2}$  = half-rise time [sec]

The thermal diffusivity for each Nextel™ 312/SiC composite specimen was evaluated at 100°C intervals from 100-1200°C. Three laser shots were performed for each specimen at each temperature. The thermal diffusivity average at each temperature was taken from the three separate measurements.

### Permeability Measurement

Knowledge of the density-dependent composite permeability is important, for it governs the gas flow in the densifying preform. A permeability apparatus was designed and constructed by Starr and Hablutzel (1998) that could handle porous composite specimens of various sizes. The apparatus was equipped with two flow controllers (10 sccm and 200 sccm) and two pressure transducers (1.33 kPa and 26.7 kPa), enabling the successful measurement of a wide magnitude of specimen permeabilities. The low range-mass flow controller (10 sccm) and high pressure transducer (200 kPa) were selected for specimens with low permeability (<10 Darcies), while the high range-mass flow controller (200 sccm) and the low pressure transducer (10 kPa) were selected for specimens with high permeability

(>10 Darcies). The Darcy (Darcy 1856), which is a standard unit of material permeability, is equivalent to  $10^{-8} \text{ cm}^2$ .

The Nextel™ 312/SiC composite specimens were mounted in aluminum rings, 2.5 cm in ID and 2.5 cm in height. The aluminum ring was placed face-down on a flat surface, and the specimen was placed face-down inside the ring. A quick-set epoxy was placed in the space between the aluminum ring and the specimen. The epoxy was given sufficient time to set (10 min), and the epoxy was inspected for any unwanted holes that would prevent gas from solely flowing through the specimen.

The specimen mounted-ring was placed in a chamber where the upper and lower aluminum ring surfaces were sealed with O-rings. The upper and lower chamber components were secured with three screws, tightened  $\frac{1}{4}$  turn past hand-tight. The desired mass flow controller and pressure transducer were selected prior to permeability measurement.

Nitrogen gas was used for the permeability measurement, with the flow regulated with a needle valve. The output voltages for both flow controller and pressure transducer were recorded with no flow to initialize the apparatus. The pressure drop data were then recorded for each flow rate introduced to the specimen.

The specimen permeability was determined by plotting pressure drop versus the flow rate. The permeability value was extracted from the slope produced by the linear fit of the data (Appendix E). Both the specimen thickness

and the nitrogen room temperature-viscosity were needed for the permeability calculation (Appendix E).

### **Tube Density Characterization**

Density characterization was performed on four Nextel™ 312/SiC composite tubes infiltrated with the same process conditions (1200°C, 6 slm total flow, 1 slm MTS) for various time lengths. Prior to the tube density characterization, the overall tube density for each tube was calculated from the tube dimensions, known initial fiber volume, and final composite mass. Tube density characterization was then performed using X-ray computed tomography and digital image analysis methods. X-ray computed tomography, which is a non-destructive technique, and digital image analysis, which is a destructive technique, were attempted to evaluate the transient density progression in the tube preform.

### **Overall Tube Density Estimation**

The preform fiber volumes were determined from the preform fiber mass and geometry (Equation 3-2). The postinfiltration OD was greater than the initial preform OD for some tubes due to a SiC overcoat (~0.2 mm) that appeared on the tube exterior. The initial preform length was 35.6 cm, while the final composite tube length was 30.5 cm, after the removal of both preform ends. Average postinfiltration ID and OD were used in the calculation of the preform volume (Equation 3-4). The preform OD was averaged from five caliper

measurements taken at equidistant interval lengths (7 cm) while the preform ID was averaged from caliper measurements taken at both preform ends.

The calculation of the tube theoretical density involved the preform mass and final composite mass (Equation 3-3). It should be noted that the final preform mass was adjusted after the end removal. The final preform mass was determined with the assumption of a constant preform mass per unit length. A sample calculation of the tube theoretical density is given in Appendix D.

$$\text{Fiber Volume} = \frac{M_{\text{Preform}}}{\rho_{\text{Fiber}} V_{\text{Preform}}} \cdot 100\% \quad (3-2)$$

$$\text{Theoretical Density} = \frac{V_{\text{Fiber}} + V_{\text{Matrix}}}{V_{\text{Preform}}} = \frac{\frac{M_{\text{Preform}}}{\rho_{\text{Fiber}}} + \frac{(M_{\text{Composite}} - M_{\text{Preform}})}{\rho_{\text{Matrix}}}}{V_{\text{Preform}}} \cdot 100\% \quad (3-3)$$

$$V_{\text{Preform}} = \pi \left[ \left( \frac{OD_{\text{Average}}}{2} \right)^2 - \left( \frac{ID_{\text{Average}}}{2} \right)^2 \right] L_{\text{Preform}} \quad (3-4)$$

where

$ID_{\text{Average}}$  = average postinfiltration OD [cm]

$M_{\text{Preform}}$  = preform mass [g]

$M_{\text{Composite}}$  = composite mass [g]

$OD_{\text{Average}}$  = average postinfiltration OD [cm]

$V_{\text{Preform}}$  = postinfiltration preform volume [cm<sup>3</sup>]

$\rho_{\text{Fiber}}$  = fiber density [g/cm<sup>3</sup>]

$\rho_{\text{Matrix}}$  = matrix density [g/cm<sup>3</sup>]

## X-ray Computed Tomography

X-ray computed tomography is a non-destructive technique which involves the inspection of density variation by observing the change in X-ray attenuation. The X-ray attenuation of a material is a density-dependent and energy-

dependent property, with materials of higher density exhibiting a higher X-ray attenuation (Ellingson and Vannier 1988). Planar cross-section tomographic images were reconstructed from the collected X-ray beam attenuation data with the use of Adobe Photoshop™ 5.0 (San Jose, CA). The grayscale variation in these images translated to density variation where lighter grayscale represented higher density.

The X-ray power used in the computed tomography was 120 kV and 0.29 mA. An amorphous silicon detector collected the attenuated X-ray beam after penetration through the composite tube. The tube preform was held vertically and was rotated in 5°-intervals per data set acquisition. The X-ray attenuation data that was collected by the detector at each axial position was processed by a digital computer, producing the planar cross-section tomographic image.

Each composite tube was analyzed at seven equidistant axial positions along the tube length (5 cm intervals). The seven reconstructed planar cross-section images appeared in a grayscale format, where a lighter grayscale corresponded to a higher material density (higher X-ray attenuation). The Adobe Photoshop™ grayscale values seen in the tomographic images fell within a 0-255 range, where pure-black corresponds to a zero-grayscale and pure-white corresponds to a 255-grayscale.

An uninfiltated Nextel™312 tube preform and dense Nextel™312 composite specimens provided a low-density and a high-density standard for the calibration of the X-ray computed tomography technique. With the densities of these calibration standards known, their respective Adobe Photoshop™

grayscale provided a linear density/grayscale relationship that was used for the tomographic image analysis.

For each reconstructed planar cross-section image, the tube thickness was analyzed at 0°, 60°, 120°, and 180°, with 0° located at the 12 o'clock position and 0° coinciding with the tube furnace fixturing. A 5°-arc section was selected at each circumferential position with the tube thickness uniformly discretized into four radial volume elements (~1 mm). The average grayscale value for each radial volume element in a tomographic image was found by taking the grayscale average from all four considered circumferential positions. The grayscale value for each radial volume element fell within the grayscale range determined by the density/grayscale relationship. The density data extracted from all seven tomographic images for each tube constituted a two-dimensional density profile (28 total density points).

### **Digital Image Analysis**

Digital image analysis is a simple, destructive, density characterization technique that is commonly used for composite systems (Matlin 1995). This technique involved the analysis of digital pictures taken from polished specimen cross-section surfaces. Composite specimens of uniform length were prepared from each of the four tubes that were characterized. Images were captured for each composite specimen with a digital microscope. The Nextel™312 fiber, SiC matrix, and void phase had distinguishable grayscales in the digital images.

An image analysis software program was used to calculate the percent area for each phase in a given digital image by counting the number of pixels that fell within a defined grayscale range. Four digital images were taken along the specimen thickness, with the length scale coinciding with the volume element length scale used in the X-ray computed tomography (~1 mm). Two-dimensional data arrays for both fiber volume and theoretical density were generated from the digital image analysis results for each tube characterized.

After the X-ray computed tomography characterization was complete, composite strips 1.2 cm in height, 7 cm in thickness, and 30.5 cm in length were prepared by slicing the composite tube along the entire length. The tube circumferential positions chosen for the composite strips were 0°, 90°, and 180°, with 0° coinciding with the 12 o'clock position in the furnace fixturing. Six composite specimens, 5.0 cm in length, were prepared from each composite strip at each circumferential position (three composite strips per tube).

For each composite tube characterized, all six composite specimens taken at 0° and one composite specimen taken from the composite tube mid-length at 90° and 180° were mounted in epoxy, with the specimen cross-section surface (through-thickness) polished. The epoxy-mounted composite specimens were pulled under vacuum to eliminate air bubbles, and were slowly brought to atmospheric pressure to fill the accessible specimen porosity with epoxy. The specimen surfaces that were analyzed were roughly polished with a 100 grit-diamond disk and subsequently fine-polished with 1  $\mu\text{m}$ -diamond paste.

Digital images (50 X magnification) were captured along either the left or right side of each polished specimen surface with a Nikon Labophot-2 Optical Microscope (Tokyo, Japan). The specimen side chosen for the image capturing coincided with the axial tube positions used in the X-ray computed tomography (5 cm intervals). Overall digital images (12.8 X magnification) were taken from the preform mid-length specimens at 0°, 90°, and 180° to inspect for possible circumferential variations. Four digital images spanned the entire composite specimen thickness.

BioScan® Optimas™ (Fifth Edition, Edmonds, WA) Image Analysis software was used for the digital image analysis. Each digital image was analyzed with a percent area algorithm that involved grayscale differentiation. Grayscale ranges were defined for the Nextel™ 312 fiber, SiC matrix, and void space. In a specified region, the percent area algorithm counted the number of pixels associated with each defined grayscale range in the entire digital image (~400 pixels X 500 pixels), and the resulting percentages for the void, Nextel™ 312 fiber, and SiC matrix were recorded.

The digital image analysis was calibrated with a concentric circle pattern standard having three distinct grayscale values. The percent areas for each grayscale phase in the standard were also measured manually. The calibration standard picture was scanned and analyzed with the Optimas™ software package, with the Optimas™ percent-area results compared to the percent-area results determined by manual measurement. The fiber volumes (percent area of



the Nextel™ 312 fiber) and theoretical densities (percent areas for the Nextel™ 312 fiber and SiC matrix) were measured and recorded for each digital image.

Each digital image required some retouching before analysis with the Optimas™ software package. Specimen damage caused by preparation and polishing created apparent black voids in the fiber bundles seen in the digital images. The Optimas™ software would recognize these damaged areas as voids (zero grayscale). Also, the accessible composite pores that filled with epoxy resembled a grayscale representative of the Nextel™ 312 fiber. The uncharacteristic fiber bundle damage and the epoxy filled-voids were manually painted with a grayscale representative of their respective phases with Optimas™ to correct for their apparent ambiguity.

## CHAPTER 4

### CVI MODELING FUNDAMENTALS

This chapter develops fundamental theory and results through a simplified, one-dimensional model of the CVI process. The analytical model was developed as a tool for exploring the parametric space of the CVI process. Process parameters were varied and their effects on initial preform densification were investigated. The results produced by this simple model suggested the process conditions that would lead to a more uniform density throughout the preform volume. With this understanding, the process conditions found with this model will be implemented in a more comprehensive CVI model.

#### **Model Description**

The one-dimensional CVI process model simultaneously solved material and energy balances in the steady-state with subsequent solution of the solid balance. The material balances for methyltrichlorosilane (MTS), hydrochloric acid (HCl), and hydrogen only considered viscous transport and reaction while the energy balance only considered energy transport by conduction (Fourier's Law). The silicon carbide (SiC) volumetric deposition rate used in the material

balances included the surface deposition rate and the specific surface area of the densifying preform.

Diffusive mass transport and multi-component transport effects in the material balances were neglected while energy transfer by convection and radiation were neglected in the energy balance. Although these mechanisms may exist physically, the inclusion of these additional terms would force a greater computational burden.

Diffusion becomes significant with infiltration using either low pressure or low gas flow. With higher precursor depletion, the precursor intermediates and reaction by-products that occur make multi-component transport effects important. Radiation becomes significant at typical infiltration temperature (1200°C) while convection becomes significant at high gas velocity (>1 cm/sec). This simplification of the material and energy balances approximated the CVI phenomena in the preform while significantly reducing computational cost.

### Constitutive Equations

The material and energy balances are given in Equations 4-1 and 4-2 respectively. These balances were solved in cylindrical coordinates with solution only in the radial direction. The radial dimension,  $r^*$ , was made dimensionless by division of the radial coordinate by the preform thickness,  $\tau_{\text{Preform}}$ . Methyltrichlorosilane (MTS), HCl, and hydrogen entered the preform at the interior ( $r^*=0$ ), infiltrated through the thickness, and exited at the preform exterior ( $r^*=1$ ). A schematic of the tube preform is seen in Figure 4-1. The SiC

deposition from MTS ( $\text{CH}_3\text{SiCl}_3$ ) followed the overall reaction seen in Equation 4-

3.

$$\nabla \cdot \mathbf{N}_i = \frac{1}{\tau_{\text{Preform}}} \frac{1}{r^*} \frac{\partial(r^* N_i)}{\partial r^*} = \nu_i R_v \quad (4-1)$$

$$\nabla T = \frac{q}{\lambda(\rho, T)} \quad (4-2)$$



where

$N_i$  = species molar flux [ $\text{mol}/\text{cm}^2 \text{ sec}$ ]

$q$  = radial energy flux [ $\text{W}/\text{cm}^2$ ]

$R_v$  = SiC volumetric deposition rate [ $\text{mol}/\text{cm}^3 \text{ sec}$ ]

$r^*$  = radial distance [Dimensionless]

$T$  = temperature [K]

$\lambda$  = preform thermal conductivity [ $\text{W}/\text{cm K}$ ]

$\nu_i$  = species stoichiometric coefficient [Dimensionless]



Figure 4-1. Tube preform description. Gaseous precursors entered the preform at the interior and exited at the exterior while the temperature gradient was placed across the preform thickness.

### Silicon Carbide Deposition Rate

The temperature and concentration dependence of the SiC volumetric deposition rate,  $R_v$ , was required to solve the material balances (Equation 4-4).

Starr et al. (1993) has suggested a deposition rate law,  $R_v$ , which is first-order in

MTS with a first-order inhibition in HCl. The volumetric deposition rate was determined by the multiplication of the surface deposition rate and the specific surface area,  $S^e$ , of the densifying preform. The definition of the species mole fraction is seen in Equation 4-5.

The reaction rate constants and the apparent activation energies were determined from fitting the deposition rate law function to experimental SiC growth data at atmospheric pressure (Besmann et al. 1991). The experimental SiC growth rate data and rate law-fit are shown in Figure 4-2. The parameter values that produced a reasonable fit to experimental SiC growth rate data are provided in Table 4-1 along with the stoichiometric coefficient, absolute density, and molecular weight of the SiC matrix (Weast 1995).

$$R_v = \frac{k_{fo} \exp\left(\frac{-E_{af}}{RT}\right) y_{MTS}}{1 + k_{ro} \exp\left(\frac{-E_{ar}}{RT}\right) y_{HCl}} S^e \quad (4-4)$$

$$y_i = \frac{N_i}{N} \quad (4-5)$$

$$N = \sum_i N_i \quad (4-6)$$

where

$E_{af}$ ,  $E_{ar}$  = apparent forward and reverse activation energies [J/mol]

$k_{fo}$ ,  $k_{ro}$  = reaction rate constants [mol/cm<sup>2</sup> sec; Dimensionless]

$R$  = universal gas constant = 8.314 J/mol K

$S^e$  = preform specific surface area [cm<sup>-1</sup>]

$y_i$  = species mole fraction [Dimensionless]

Table 4-1. Silicon Carbide Volumetric Deposition Rate Parameters

$k_{fo}$ [mol/cm <sup>2</sup> sec]	5.26E-03	$E_{af}$ [J/mol]	102.7
$k_{ro}$ [Dimensionless]	3.60E-03	$E_{ar}$ [J/mol]	-168.6
SiC Stoichiometric Coefficient	1		
SiC Density[g/cm <sup>3</sup> ]	3.2		
SiC Molecular Weight[g/mol]	40.1		

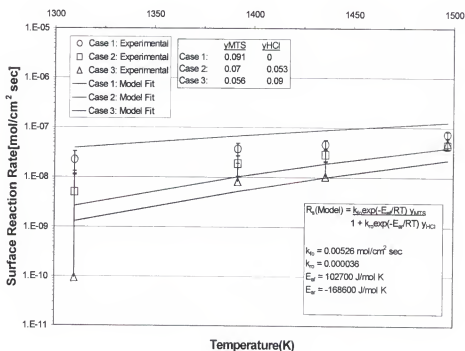


Figure 4-2. Experimental SiC surface deposition rate data at different temperatures for several MTS/HCl/H<sub>2</sub> mixtures (Besmann et al. 1991). The proposed deposition rate law model and associated parameters were fit to the experimental data at atmospheric pressure.

### Preform Transport Properties

The preform thermal conductivity and specific surface area play a significant role in the CVI process. These preform properties continually change during the CVI process as SiC is deposited on the fiber surfaces throughout the

preform. Inspection of their magnitude and functionality can aid the investigator in the selection of process variables ( $T$ ,  $\Delta T$ ,  $N$ ).

The thermal conductivity function used in the model is shown in Figure 4-3. This thermal conductivity function,  $\lambda$ , represents an isotropic, densifying, random three-dimensional fiber structure and was developed by Tomadakis and Sotirchos (1993b). The thermal conductivity monotonically decreases with increasing temperature at a given theoretical density and monotonically increases with the increase in theoretical density at a given temperature. The density,  $\rho$ , is represented as a normalized theoretical density, which is the ratio of the summation of both fiber and matrix volumes to the total volume. The parameter,  $\varepsilon_p$ , is a percolation threshold representing the maximum allowable normalized theoretical density before the preform porosity is no longer accessible. The normalized  $\varepsilon_p$ -value used was 0.963, the percolation threshold found for the random, three-dimensional fiber structure.

The specific surface area function used in the one-dimensional CVI model is shown in Figure 4-4. This surface area function was an approximation to the surface area function representative of fiber bundles, which was calculated using Monte Carlo simulation (Starr 1988). The surface area monotonically decreases with density,  $\rho$ . This surface area function represented the initial stages of CVI, where the intrabundle porosity is filled with SiC matrix (neither interstitial channels nor interlaminar porosity).

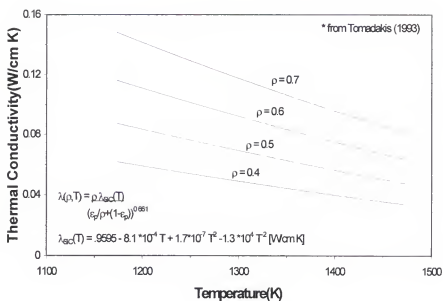


Figure 4-3. The thermal conductivity function used in the one-dimensional CVI model. The composite thermal conductivity was a function of the SiC thermal conductivity, theoretical density, and the percolation threshold,  $\epsilon$ .

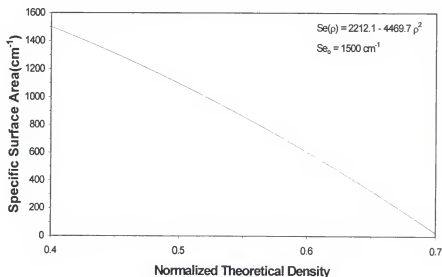


Figure 4-4. The specific surface area function used in the one-dimensional CVI model. This function represents the surface area within a fiber bundle.



Another transport property significant in the CVI process, but not included in this simple model, is the preform permeability. In a porous media, the molar flux is proportional to the pressure gradient across the media thickness (Carman 1956). The proportionality constant includes the preform permeability. For a given molar flux, a decrease in permeability yields an increase in the pressure gradient. With an assumed constant preform permeability, a higher molar flux yields a higher pressure gradient.

### Boundary Conditions

The material and energy balances were solved with appropriate initial boundary conditions. The molar fluxes for MTS, HCl, and hydrogen fed to the preform are provided in Equations 4-7, 4-8, and 4-9. Although no net molar change was seen with the hydrogen, the molar flux of hydrogen changed due to the increase in the preform cross-sectional area. The initial mole fractions of MTS, HCl, and hydrogen seen at the preform interior are functions of the molar feed fraction of MTS and the normalized MTS simulated depletion,  $\beta$ .

The molar MTS feed fraction,  $y_{\text{MTS}}$ , is the ratio of the number of MTS moles to the total number of moles. The MTS simulated depletion,  $\beta$ , is the normalized MTS depletion percent prior to preform infiltration, where higher  $\beta$  values yield higher HCl concentrations and lower MTS concentrations.

$$y_{\text{MTS}} = y_{\text{MTS}}^{\text{Feed}} (1 - \beta) \quad N_{\text{MTS}} = N \cdot y_{\text{MTS}} \quad (4-7)$$

$$y_{\text{HCl}} = 3y_{\text{MTS}}^{\text{Feed}} \beta \quad N_{\text{HCl}} = N \cdot y_{\text{HCl}} \quad (4-8)$$

$$y_{\text{H}_2} = 1 - y_{\text{MTS}}^{\text{Feed}} (1 + 2\beta) \quad N_{\text{H}_2} = N \cdot y_{\text{H}_2} \quad (4-9)$$

where  $y_{\text{MTS}}^{\text{Feed}}$  = molar feed fraction of MTS [Dimensionless]  
 $\beta$  = normalized simulated MTS depletion [Dimensionless]

The initial boundary condition for the energy balance involves the preform radial temperature difference,  $\Delta T$ . A dimensionless temperature,  $\theta$ , was obtained by dividing the preform interior temperature by the preform exterior temperature (Equation 4-10). The preform radial temperature difference,  $\Delta T$ , was defined as a function of the dimensionless temperature,  $\theta$  (Equation 4-11).

$$\theta = \frac{T_{\text{Interior}}}{T_{\text{Exterior}}} \quad (4-10)$$

$$\Delta T = T_{\text{Exterior}}(1 - \theta) \quad (4-11)$$

A  $\theta$ -value of one corresponded to an isothermal system with zero energy flux ( $q=0$ ). For a desired  $\theta$ -value less than one, the energy flux value,  $q$ , was adjusted in the energy balance such that the desired exterior preform temperature was reached ( $r^*=1$ ).

### Method of Solution

The material and energy balances are ordinary differential equations and they were solved simultaneously with the aforementioned initial boundary conditions using a fourth-order Runge-Kutta method (Jennings 1964). Model results were presented as a dimensionless reaction rate ratio. The reaction rate

ratio (Equation 4-12) was defined as the reaction rate at a given position in the preform divided by the reaction rate at the preform interior ( $r^*=0$ ).

$$\text{Reaction Rate Ratio } (r^*) = \frac{\text{Reaction Rate } (r^*)}{\text{Reaction Rate } (r^* = 0)} \quad (4 - 12)$$

## Model Results

The one-dimensional CVI model results show the initial reaction rate ratio (i.e. at the start of infiltration) through the dimensionless preform thickness. The model results show how a single process parameter variation affected the reaction rate ratio throughout the entire thickness. The CVI process parameters that were considered include the preform temperature,  $T_{\text{Exterior}}$ , the total molar flux,  $N$ , the temperature gradient,  $\theta$ , the normalized simulated depletion,  $\beta$ , and the preform thickness,  $\tau_{\text{Preform}}$ . The initial preform theoretical density (fiber volume only) considered in the model,  $\rho$ , was 40%. The variation of each process parameter and its effect on the reaction rate ratio are shown and discussed. From these results, the most favorable process parameters were selected and implemented in GTCVI, a more comprehensive, three-dimensional finite-volume element code.

Isothermal CVI (ICVI) was investigated using the one-dimensional model and the results are shown in Figure 4-5. The magnitude of the total molar flux used was  $10^{-6}$  mol/cm<sup>2</sup> sec (Equation 4-13). This magnitude was estimated

below for a 10 kPa-MTS partial pressure at 1000K with a 0.1 cm-preform thickness.

$$N_{\text{MTS}}^{\text{Diffusive}} = D_{\text{MTS}}^{\text{eff}} \frac{dC_{\text{MTS}}}{\tau_{\text{Preform}}} = (0.1) * \left(0.1 \frac{\text{cm}^2}{\text{sec}}\right) * \frac{\left[\frac{1 \text{ atm}}{(100 \frac{\text{cm}^3 \text{ atm}}{\text{mol K}}) * (1000 \text{ K})}\right] * (0.1)}{(0.1 \text{ cm})} = 10^{-6} \frac{\text{mol}}{\text{cm}^2 \text{ sec}} \quad (4-13)$$

where

$C_{\text{MTS}}$  = MTS concentration [mol/cm<sup>3</sup>]  
 $D_{\text{MTS}}^{\text{eff}}$  = MTS effective diffusivity [cm<sup>2</sup>/sec]  
 $\tau_{\text{Preform}}$  = preform thickness [cm]

For all temperatures considered, the reaction rate was highest at the preform interior and monotonically decreased with dimensionless thickness. As the preform temperature was lowered, the reaction rate ratios were higher throughout the entire preform thickness, but still monotonically decreased. However, the lower temperatures resulted in lower absolute reaction rates. The decreasing reaction rates seen through the preform interior arose from the MTS depletion as the gas infiltrated through the preform thickness. The higher reaction rate ratios seen with the use of lower temperatures forced the FCVI process to fall within the reaction limited-regime (low Thiele modulus). These trends agreed with the cited ICVI modeling work that was presented in Chapter 2.

Variation of the total molar flux and its effect on the reaction rate are seen in Figure 4-6. A dimensionless temperature difference ( $\theta=0.85$ ) was used. For a total molar flux value of  $10^{-6}$  mol/cm<sup>2</sup> sec (comparable diffusive flux), the reaction rate was highest at the preform interior. At a flux value of  $10^{-5}$  mol/cm<sup>2</sup> sec, the

reaction rate increased through the preform and reached a maximum, resulting in greater deposition in the middle of the preform thickness than at the preform interior and exterior. The reaction rate ratio maximum occurred because of the temperature/MTS depletion trade-off, where the increase in MTS depletion outweighed the increase in temperature. For molar flux values greater than  $10^{-5}$  mol/cm<sup>2</sup> sec, the reaction rate was lowest at the preform interior and monotonically increased, reaching a maximum at the exterior where depletion effects were outweighed by the temperature dependence.

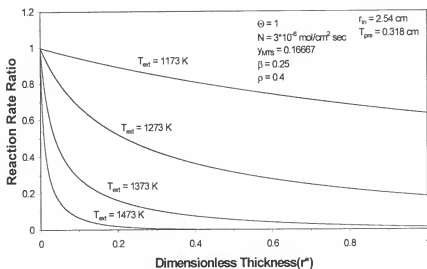


Figure 4-5. Reaction rate ratios with variation of preform temperature. Lower temperature improves uniformity throughout the preform thickness, but still forces preferential matrix deposition at the preform interior. All other CVI process parameters are shown.

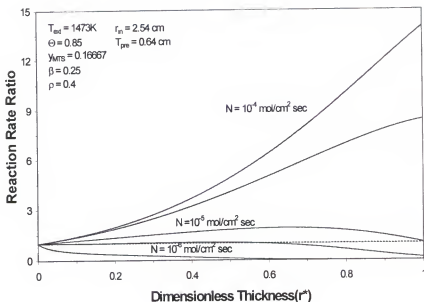


Figure 4-6. Reaction rate ratios with variation of the total molar flux. All other CVI process parameters are shown.

Variation of the preform temperature difference and its effect on the reaction rate are seen in Figure 4-7. For  $\theta$ -values of 0.9 and 1, the reaction rate was highest at the preform interior and monotonically decreased through the preform thickness. For lower  $\theta$ -values, the reaction rate increased through the preform thickness reaching a maximum in the middle of the preform. The reaction rate maximum occurred further towards the preform exterior as  $\theta$  was lowered. Again, the maximum in the reaction rate ratio was due to the trade-off in temperature and MTS depletion. At  $\theta$ -values of 0.7 and 0.75, reaction rate ratios greater than one occurred at the preform exterior. The reaction rate trends with the use of higher temperature differences were similar to those trends seen with the use of a higher total molar flux.

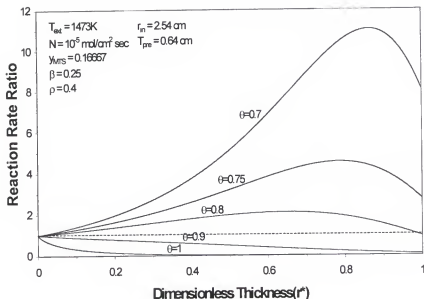


Figure 4-7. Reaction rate ratios with variation of the preform temperature difference. Lower  $\theta$ -values represent higher temperature differences. All other CVI process parameters are shown.

Variation of the normalized simulated MTS depletion,  $\beta$ , is seen in Figure 4-8. The results use a  $\theta$ -value of 0.9 and a preform exterior temperature of 1473 Kelvin ( $\Delta T = 147.3\text{ K}$ ). Higher  $\beta$  values represented higher MTS depletion and higher HCl concentration in the feed gas mixture. At low MTS depletion, the reaction rate was highest at the preform interior and monotonically decreased through the preform thickness. As  $\beta$  was increased, the reaction rate maximum was still at the preform interior. However, the reaction rate ratios were higher through the preform thickness. Increasing MTS depletion at this temperature difference prior to preform infiltration yielded similar results to the ICVI process with the use of a lower preform temperature.

In Figure 4-9, the normalized simulated depletion was examined using a higher preform temperature difference ( $\theta=0.85$ ). For low simulated MTS depletions ( $\beta<0.1$ ), the reaction rate ratios were less than one throughout the entire preform. At higher simulated MTS depletions ( $\beta>0.1$ ), reaction rate ratios greater than one occurred with the ratio maximum shifting towards the preform exterior at higher depletion levels. These trends at higher depletion levels resembled those trends seen with higher preform temperature differences (lower  $\theta$  values) and higher total molar flux. For lower  $\beta$ -values, the reaction rate ratio uniformity improved through the preform thickness. However, the absolute value of the reaction rate was lower at higher depletion levels throughout the entire preform due to the higher HCl content.

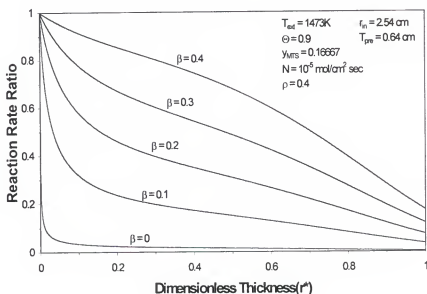


Figure 4-8. Reaction rate ratios with variation of the normalized MTS simulated depletion using  $\theta=0.9$ . All other CVI process parameters are shown.



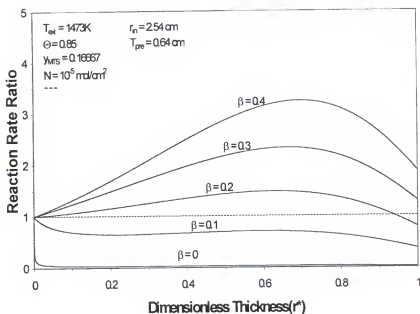


Figure 4-9. Reaction rate ratios with variation of the normalized simulated MTS depletion using  $\theta=0.85$ . All other CVI process parameters are shown.

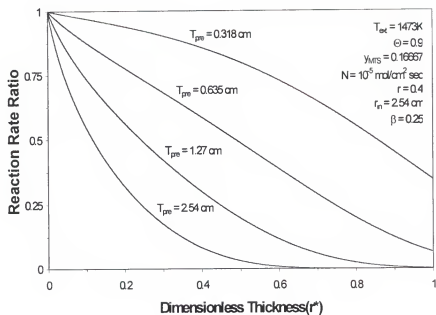


Figure 4-10. Reaction rate ratios with variation of the preform thickness. Results suggest use of higher temperature differences or higher total molar fluxes for thicker preforms. All other CVI process parameters are shown.

The last process variable considered in this section was the preform thickness. Variation of the preform thickness and its effect on the reaction rate are seen in Figure 4-10. As the preform thickness increased, the reaction rate ratio was lower throughout the entire preform resulting in poorer infiltration through the preform due to MTS depletion. This suggested that higher preform temperature gradients or higher total molar fluxes should be used to improve through-thickness infiltration for thicker preforms.

### **One-Dimensional Model Conclusions**

Isothermal conditions and low total molar flux resulted in higher reaction rates at the preform interior. If infiltration continued under these process conditions, the higher MTS concentration and the decreasing specific surface area would result in premature sealing of the interior, leading to poorer deposition uniformity and lower overall density in the preform.

Increasing the total molar flux, temperature gradient, and simulated MTS depletion favored higher reaction rates initially at the preform exterior. At higher preform density, the specific surface area decreased and the thermal conductivity increased. The increase in thermal conductivity from the addition of the SiC increased the preform interior temperature, making reaction rates higher in this region due to higher specific surface area and higher MTS concentration. This forced the maximum SiC deposition rate to advance from the preform exterior to the preform interior promoting a more uniform, final density. This situation was successful given that the preform permeability was adequate to support ample gas flow at high densities.

Variation of the total molar flux under isothermal conditions was not presented in this work. Arguments can be made suggesting that the increase of the total molar flux with an isothermal system would lead to more uniform reaction rates and densities. However, the high convective gas cooling that would result from the high molar flux would lower the preform temperature. Also, low precursor efficiencies would be realized, wasting unutilized precursor. Although the primary focus of this work was the search for process conditions that favored greater density uniformity, the precursor efficiency was a secondary issue for optimization.

A transient CVI process simulation with process conditions selected from the aforementioned results is presented in Figure 4-11. Initially, the density was highest at the preform exterior. At later times, the density change near the preform exterior was slower due to less available surface area. The higher density at the preform exterior also yielded higher thermal conductivity. With a constant radial energy flux assumed in the model, a higher thermal conductivity resulted in a lower preform temperature difference making the preform interior higher in temperature favoring higher deposition rates. At seven hours, a uniform density profile was seen across the entire preform thickness. A normalized theoretical density of 0.7 was chosen to represent sufficient consolidation of the intrabundle porosity.

The use of an acceptable total molar flux and temperature gradient was considered in the next chapter with a comprehensive three-dimensional finite-volume model that simulated the FCVI process. These process parameters were

varied and their effects on density and total infiltration time were considered. Thorough investigation of these favorable process parameters will demonstrate the parameter set that leads to an acceptable tube density in the lowest total process time.

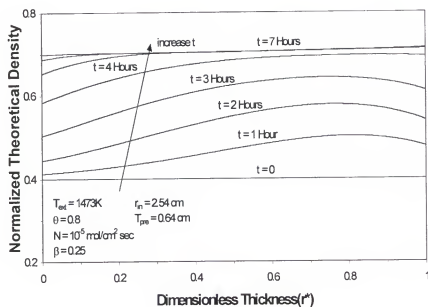


Figure 4-11. Transient CVI simulation with use of an acceptable total molar flux and temperature difference.

## CHAPTER 5

### FCVI PROCESS MODELING

A comprehensive, three-dimensional finite-volume element code, GTCVI, was developed specifically for the modeling of CVI processes (Starr 1988, 1991, Starr and Smith 1992, 1995b). This source code, GTCVI, solved species, energy, and momentum balances in steady-state over a three-dimensional finite-volume element array. The solution of these balances was approximated using a central-difference technique. The central-difference algorithm used approximated the differential equations with an array of simultaneous algebraic equations (Patankar 1980). Model inputs contained array element dimensions and material definitions, transport property values for the tube preform, gas mixture, and other associated materials, and the SiC deposition rate parameters. Multiple time steps of finite length were input to the model making it able to demonstrate the transient densification of the fibrous preform.

#### **Model Description**

This section describes the constitutive balances and discretization used in GTCVI along with the definition of the SiC solid balance used to update the density throughout the tube preform. The boundary conditions used in the

solution of these balances are included. All the information that is contained in input files, describing all pertinent materials and the infiltrating gas mixture, is listed at the end of this section.

### Constitutive Balances

Momentum was defined using Darcy's law (Darcy 1856), which states that the total molar flux,  $N$ , through a porous medium of a given thickness is proportional to the pressure difference,  $\Delta P$  (Equation 5-1). The average gas velocity through a porous medium,  $u$ , was extracted from Darcy's law by dividing the molar flux by the gas concentration (Equation 5-2).

The continuity equation is shown in Equation 5-3. This continuity definition stated that the divergence of the total molar flux is equal to zero. Theoretically, a positive net molar production of moles occurs due to the depletion and reaction of the MTS precursor, yielding 3 moles of HCl per mole of MTS. The primary reason for the zero divergence-assumption was that the MTS is fed in excess hydrogen making the increase in moles minimal.

$$N = uC = \frac{-\beta}{\mu} \frac{P}{RT} \nabla P \quad (5-1)$$

$$u = \frac{-\beta}{\mu} \nabla P \quad (5-2)$$

$$\nabla \cdot N = 0 \quad (5-3)$$

where

- $C$  = total concentration [mol/cm<sup>3</sup>]
- $N$  = total molar flux [mol/cm<sup>2</sup> sec]
- $P$  = pressure [g/cm sec<sup>2</sup>]
- $T$  = temperature [K]
- $u$  = average gas velocity [cm/sec]

$$\beta = \text{permeability [cm}^2\text{]}$$

$$\mu = \text{gas viscosity [g/cm sec}^2\text{]}$$

The energy balance included contributions from conduction, convection, and radiation (Equation 5-4). Calculation of the conduction and convection components was straightforward given the thermal conductivity, permeability, and heat capacity of the permeable element. Radiation terms were considered for volume elements that had faces bordering open gas space elements. The radiation component was included as a source term, which is proportional to the fourth order in temperature ( $\sim \epsilon \sigma T^4$ ) (Bird et al. 1960).

A separate algorithm was used for the calculation of the radiation component. The modeled FCVI geometry involved volume elements that bordered gas space, such as the graphite coating chamber and the tube preform interior and exterior. The algorithm first determined view factors for all radiating faces using a Monte Carlo ray-tracing method (Starr and Smith 1995b). These view factors were then used to calculate the radiosity for each volume element. The radiosity for each element involved the summation of both absorbed radiant energy and reflected radiant energy from all other radiating surfaces.

$$\mathbf{u} \cdot \nabla (\rho C_p T) = \nabla \cdot (\lambda \nabla T) + S_{\text{Radiation}} \quad (5-4)$$

where

$C_p$  = heat capacity [J/mol K]

$S_{\text{Radiation}}$  = volumetric radiation energy flux [W/cm<sup>3</sup>]

$\lambda$  = thermal conductivity [W/cm K]

The fourth order-temperature relationship seen in the radiation component in the energy balance caused the parameter solution to oscillate and sometimes diverge between successive model iterations. This problem was corrected by linearizing the temperature using temperature values from the previous iteration (Equation 5-5). This significantly improved convergence while maintaining the banded matrix structure used in the calculation of the energy balance (Starr and Smith 1995b).

$$S_i^{\text{Radiation}} = K_1 T_{i-1}^3 + K_2 \quad (5-5)$$

where  $K_1, K_2$  = constant terms  
 $T_{i-1}$  = temperature value from previous iteration [K]  
 $T_i$  = temperature value at current iteration [K]

Diffusion, convection, and heterogeneous chemical reaction were considered in the species material balances for MTS and HCl (Equation 5-6). The convective component was directly proportional to the average velocity through the element (Equation 5-1). The effective diffusivity of MTS and HCl was a product of the molecular mixture diffusivity and an effective diffusion coefficient. The effective diffusion coefficient is the ratio of the molecular diffusivity through the composite material and the bulk molecular diffusivity in free space. The volumetric reaction rate of the SiC matrix was added to the species balances as a source term. The SiC deposition rate law, overall reaction, and associated parameters were the same as those defined in Chapter 4.



$$\mathbf{u} \cdot \nabla \mathbf{C}_i = \nabla \cdot (\mathbf{D}_i^{\text{eff}} \nabla \mathbf{C}_i) + \nu_i R_v \quad (5-6)$$

where  $C_i$  = species molar concentration [mol/cm<sup>3</sup>]  
 $D_i^{\text{eff}}$  = species effective mixture molecular diffusivity [cm<sup>2</sup>/sec]  
 $R_v$  = SiC volumetric deposition rate [mol/cm<sup>3</sup> sec]  
 $\nu_i$  = species stoichiometric coefficient [Dimensionless]

### Model Discretization

The FCVI tube experimental reactor configuration was partitioned into a two-dimensional array of finite volume elements (Figure 5-1). Total array dimensions were 6.7 cm by 62.2 cm. Due to reactor symmetry, the array was taken from the coating chamber center-line to the chamber periphery. Thirty-five radial elements and 49 axial elements defined the model domain discretization while four radial elements and twenty-nine axial elements defined the tube preform discretization (6.4 mm x 36.8 cm) in the array.

The chosen preform volume element dimensions were 1.6 mm in thickness and 1.3 cm in length. The volume thickness was chosen to represent an acceptable length scale for the assumption of material homogeneity. The radial and axial volume dimensions for each element in the array were specified in the model input file.

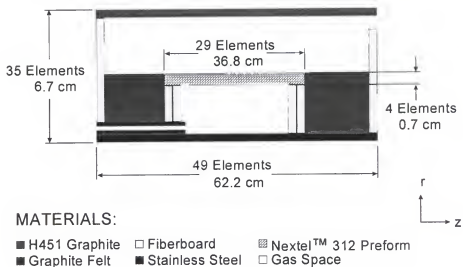


Figure 5-1. Volume element array size in the model domain. Twenty-nine axial and four radial volume elements define the tube preform.

## Boundary Conditions

The applied boundary conditions used in the model are shown in Figure 5-2.

2. The hydrogen flow and the hydrogen/MTS molar feed fraction were provided at the gas injector inlet. Atmospheric pressure was defined at the coating chamber gas exhaust. A coating-chamber temperature profile that matched the experimental temperatures measured by infrared thermometer at the three furnace sight ports was placed along the chamber length. A constant cooling line temperature 50°C was placed along the length of the cooling line. The temperature boundary conditions placed at the coating chamber ends were set at 250°C. The use of an adiabatic temperature boundary condition on the coating chamber ends produced similar temperature and density results, therefore, the isothermal boundary condition was kept. All applied boundary conditions were specified in the model input file.

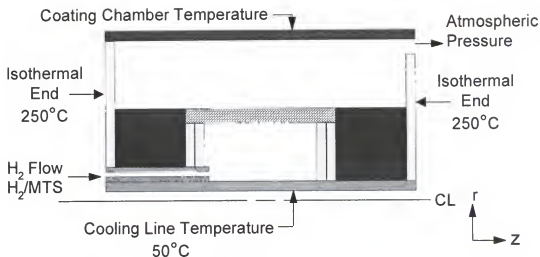


Figure 5-2. Boundary conditions specified in GTCVI.

### Method of Solution

Initial parameter guesses for the temperature, pressure, and species concentrations were specified in the model input file. The solution of these conservation balances translated from the domain boundaries to the domain interior. Parameter convergence was best achieved by performing the solution in the direction of the largest parameter gradient. Therefore, the chosen direction of the parameter solution was taken from the high temperature-coating chamber to the low temperature-cooling line.

The energy, momentum, and continuity balances were de-coupled from the species balances for ease of parameter solution convergence. Although gas mixture transport properties were functions of species concentrations as well as temperature, the model only considered the temperature dependence of the transport properties.

Temperature was solved first using the initial guess-values for the pressure. The iterated temperature values were then used in the momentum and continuity balances to solve for pressure. The calculated pressure values were then used for reiteration of energy balance. This continued until the temperature and pressure values met the convergence criteria specified in the model input.

The MTS and HCl species balances were then iterated using the converged temperatures and pressures. The species balances were solved in mole fractions, and not concentration, since the total concentration was known from the converged pressure and temperature values. Convergence criteria were also specified for both species concentrations.

For each time step, the density was updated in the preform elements from the calculation of the SiC deposition rate, which used the converged values for the temperature, MTS, and HCl concentrations (Equation 5-7 and 5-8). The density used in the specific surface area function in the volumetric deposition rate was the new density that was being evaluated at the particular iteration. This calculation required an iterative process, but lead to smooth density profiles near the end of infiltration (Starr and Smith 1992). Once the density for each preform element was calculated, the preform transport properties were updated before solution at the next time step.

$$\frac{d\rho}{dt} = \frac{v_{\text{SiC}} R_v \text{MW}_{\text{SiC}}}{\rho_{\text{SiC}}} \quad (5-7)$$

$$\rho(t + \Delta t) = \rho(t) + \frac{d\rho}{dt}(t + \Delta t) \cdot \Delta t \quad (5-8)$$

where  $\rho$  = theoretical density [Dimensionless]  
 $MW_{SiC}$  = molecular weight of SiC [g/mol]  
 $\rho_{SiC}$  = SiC density [g/cm<sup>3</sup>]  
 $t$  = time [hours]

The model wrote the converged values for the temperature, pressure, and species concentrations for all domain volume elements for each time step to an individual data file. These parameters at each time step were then extracted for data analysis.

### Model Input Files

Each GTCVI model run required an input file, gas file, and all associated material files. The input file contained the parameter convergence criteria, domain dimensions and material definitions for each volume element, all material and gas files used, and the number and length of the time steps. An example of the model input file used in GTCVI is seen in Appendix A.

### Material Files

The material files contained the functions for the preform permeability, effective diffusion coefficient, specific surface area, and emissivity. These functions were provided in a density-dependent, table format for model interpolation. The material thermal conductivities, including the tube preform, were fitted to a power-law temperature function with a first-order density dependence placed in the denominator. The tube preform material file,

containing the density-dependent transport properties, used in the GTCVI input is seen in Appendix B.

### **Gas Files**

The gas files contained the functions for the gas mixture viscosity, thermal conductivity, and heat capacity. The mixture molecular diffusivities for both the precursor and by-product were also included. The files also contained the SiC deposition rate constants and the molecular weight and density of the SiC matrix. An example of the gas file used in the GTCVI input is seen in Appendix C.

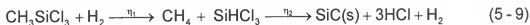
### **Gas Mixture Transport Properties**

The gas mixture transport properties were calculated from the pure species properties as described in this section. The mixture viscosity, heat capacity, thermal conductivity, and molecular diffusivities were needed for the solution of the momentum, energy, and mass species balances. These transport property values were fitted to polynomial functions of temperature.

The mixture thermal transport properties were calculated assuming a quaternary gas mixture of  $\text{CH}_4$ ,  $\text{SiHCl}_3$ ,  $\text{HCl}$ , and  $\text{H}_2$ . The MTS in hydrogen was assumed to fully dissociate into  $\text{CH}_4$  and  $\text{SiHCl}_3$  before reacting to form SiC matrix and  $\text{HCl}$ , yielding a normalized reaction coordinate ( $\eta_1$ ) of one (Equation 5-9). A normalized reaction coordinate of 0.2 was used in the MTS intermediate depletion ( $\eta_2$ ). The mole fractions for all gas species were functions of the

MTS/hydrogen molar feed ratio,  $\alpha$ , and both normalized reaction coordinates,  $\eta_1$  and  $\eta_2$  (Equations 5-10 through 5-13).

The assumption of complete MTS dissociation into  $\text{SiHCl}_3$  and  $\text{CH}_4$  was made from the MTS kinetic observations of others (Allendorf et al. 1994, Besmann et al. 1991). The use of the normalized reaction coordinate for the intermediate depletion ( $\eta_2=0.2$ ) was a sensible average that represented the entire tube preform volume.



$$y_{\text{SiHCl}_3} = \frac{\eta_1 - \eta_1\eta_2}{1 + \alpha + 2\eta_1\eta_2} \quad y_{\text{CH}_4} = \frac{\eta_1 - \eta_1\eta_2}{1 + \alpha + 2\eta_1\eta_2} \quad (5-10-13)$$

$$y_{\text{HCl}} = \frac{3\eta_1\eta_2}{1 + \alpha + 2\eta_1\eta_2} \quad y_{\text{H}_2} = \frac{\alpha - \eta_1 + \eta_1\eta_2}{1 + \alpha + 2\eta_1\eta_2}$$

where  $y_i$  = species mole fraction [Dimensionless]  
 $\alpha$  = hydrogen/MTS molar feed ratio [Dimensionless]  
 $\eta_i$  = normalized reaction coordinate [Dimensionless]

### Pure Species Transport Properties

The Chapman-Enskog equation was used for the calculation of the viscosity of a pure gas species (Equation 5-14). The collision integral used for the viscosity function,  $\Omega_v$ , was based on the Stockmayer potential function (Reid et al. 1977).

$$\mu = 26.69 \cdot 10^{-6} \frac{\sqrt{MW T}}{\sigma^2 \Omega_v} \quad (5-14)$$

where      MW = molecular weight [g/mol]  
               T = temperature [K]  
                $\mu$  = viscosity [Poise]  
                $\sigma$  = collision diameter [Å]  
                $\Omega_v$  = Stockmayer viscosity collision integral [Dimensionless]

### Heat Capacity

The heat capacities of each gas species were calculated from the tabulated data thermochemical data provided in Barin (1989). The temperature-dependent function used to calculate the heat capacity is shown in Equation 5-15.

$$C_p(T)_i = a_i + b_i T + c_i T^2 + d_i T^{-2} \quad (5-15)$$

### Thermal Conductivity

The equation used to calculate the thermal conductivity of a gas component is seen in Equation 5-16 (Reid et al. 1977). The thermal conductivity is a function of the heat capacity, viscosity, and molecular weight. The R-parameter is the universal gas constant.

$$\lambda_i = \left( C_{p_i} + \frac{5}{4} R \right) \frac{\mu_i}{MW_i} \quad (5-16)$$

### Molecular Diffusivity

Chapman-Enskog theory was again used to calculate binary molecular diffusivities (Equation 5-17). The Stockmayer diffusivity collision integral,  $\Omega_D$ , and all necessary parameters are found in Reid et al. (1977).



$$D_{IJ} = 1.858 \cdot 10^{-3} T^{\frac{3}{2}} \frac{M_{IJ}}{P \sigma_{IJ}^2 \Omega_D} \quad (5-17)$$

$$M_{IJ} = \sqrt{\frac{M_I + M_J}{M_I M_J}} \quad (5-18)$$

where  $D_{IJ}$  = binary diffusivity of species I in stagnant J [ $\text{cm}^2/\text{sec}$ ]  
 $M_{IJ}$  = binary molecular weight function [ $\text{mol/g}$ ]  
 $P$  = pressure [atm]  
 $\sigma_{IJ}$  = binary collision diameter [ $\text{\AA}$ ]  
 $\Omega_D$  = Stockmayer diffusivity collision integral [Dimensionless]

### Gas Mixture Calculation

The gas mixture viscosity, heat capacity, and thermal conductivity were calculated using the pure species transport properties (Equation 5-19). Binary interaction parameters were evaluated and were used in the mixture calculation. For the mixture viscosity and heat capacity, the Brokaw theory (Reid et al. 1977) was used to calculate the binary interaction parameters. Reid suggested the Brokaw theory for polar/non-polar interaction pairs.

The binary interaction parameters used in the mixture thermal conductivity were calculated using the Lindsay-Bromley method (Reid et al. 1977). Reid suggested the Lindsay-Bromley theory for polar/non-polar pairs.

$$\Psi_{\text{Mixture}} = \sum_i \left( \frac{y_i \Psi_i}{\sum_j y_j \phi_{ij}} \right) \quad (5-19)$$

where  $y_i$  = species mole fraction [Dimensionless]  
 $\phi_{ij}$  = binary interaction parameter [Dimensionless]  
 $\psi^{\text{Mixture}}$  = mixture  $\mu$ ,  $C_p$ , or  $\lambda$   
 $\psi$  = species  $\mu$ ,  $C_p$ , or  $\lambda$

The equation used in the calculation of the species mixture molecular diffusivity is shown below in Equation 5-20. The use of this function for the mixture calculation holds when all other species are stagnant or are traveling at the same local velocity (Bird et al. 1960).

$$D_i^{\text{Mixture}} = \left( \sum_j \frac{y_j}{D_{ij}} \right)^{-1} (1 - y_i) \quad (5 - 20)$$

where  $D_{ij}$  = binary molecular diffusivity [ $\text{cm}^2/\text{sec}$ ]  
 $D_i^{\text{Mixture}}$  = species mixture diffusivity [ $\text{cm}^2/\text{sec}$ ]  
 $y_i$  = species mole fraction [Dimensionless]

## Material Transport Properties

The calculation method for the material transport properties is included in this section. The tube preform transport properties that were evaluated include the thermal conductivity, permeability, effective diffusion coefficient, specific surface area, and emissivity.

### Thermal Conductivity

The preform thermal conductivities for both fiber orientations (perpendicular and parallel) were fitted to the data taken from experimental laser-

flash thermal diffusivity (Equation 5-9). Experimental thermal diffusivities,  $\alpha$ , were converted to thermal conductivities,  $\lambda$ , by the multiplication of a heat capacitive function,  $\rho C_p$  (Equation 5-21). The calculated thermal conductivities were fitted to a power-law function in temperature (Equation 5-22). The thermal conductivity function parameters for both fiber orientations were calculated and the results are provided in Chapter 7.

$$\lambda_i(T, \rho) = \alpha(T, \rho) \cdot \rho C_{p_i}(T, \rho) \quad (5-21)$$

$$\lambda_i(T, \rho) = \frac{T^c}{a\rho + b} \quad (5-22)$$

where       $a, b, c$  = constants  
                $T$  = temperature [ $^{\circ}\text{C}$ ]  
                $\lambda_i$  = species thermal conductivity [ $\text{W}/\text{cm K}$ ]  
                $\alpha$  = thermal diffusivity [ $\text{cm}^2/\text{sec}$ ]  
                $\rho C_{p_i}$  = species heat capacitive function [ $\text{J}/\text{cm}^3 \text{ K}$ ]

The Nextel™ 312/SiC mixture heat capacitive function was calculated from a weighted average of both SiC and Nextel™ 312 fiber (Equation 5-23). The Nextel™ 312 heat capacity was calculated using a weighted average of crystalline phases of  $\text{Al}_2\text{O}_3$ ,  $\text{SiO}_2$ , and  $\text{B}_2\text{O}_3$  (Equation 5-24) provided by Barin (1989), although the actual fiber composition consists of a  $9\text{Al}_2\text{O}_3:2\text{B}_2\text{O}_3$  crystal type with additional amorphous  $\text{SiO}_2$  (3M Corporation, Saint Paul, MN). The temperature dependent, silicon carbide heat capacity was referenced from thermochemical data provided by Chase (1986).

The thermal conductivity functions for the Polycarbon graphite felt, Poco graphite, and the Fiberfrax were fitted to experimental data provided by the respective companies. A constant thermal conductivity of 0.3 W/cm K was used for the stainless steel (Weast 1995).

$$\rho C_p(\rho, T) = \frac{\text{Fiber Volume}}{100} \rho C_{p_{\text{Nextel}}}(\rho, T) + \frac{(\text{Theoretical Density} - \text{Fiber Volume})}{100} \rho C_{p_{\text{SiC}}} \quad (5-23)$$

$$\rho C_{p_{\text{Nextel}}}(\rho, T) = 0.62 \rho_{\text{Al}_2\text{O}_3} C_{p_{\text{Al}_2\text{O}_3}}(T) + 0.24 \rho_{\text{SiO}_2} C_{p_{\text{SiO}_2}}(T) + 0.14 \rho_{\text{B}_2\text{O}_3} C_{p_{\text{B}_2\text{O}_3}}(T) \quad (5-24)$$

where  $\rho C_p$  = composite heat capacitive function [ $\text{J}/\text{cm}^3 \text{ K}$ ]  
 $\rho C_{p_i}$  = species heat capacitive function [ $\text{J}/\text{cm}^3 \text{ K}$ ]  
 $\rho_i$  = species density [ $\text{g}/\text{cm}^3$ ]  
 $T$  = temperature [K]

## Permeability

Preform permeabilities for both fiber orientations were fitted to the experimental data. The permeability data for the Nextel™ 312/SiC specimens at various densities for both fiber orientations are provided in Chapter 6. The density-dependent permeability values were generated from their respective logarithmic functions that were fit to the experimental data, and were input to the model in tabular form.

Both graphite and stainless steel were considered impermeable. A measured permeability of  $10^{-8} \text{ cm}^2$  (1 Darcy) was reported for the Fiberfrax™ (Starr and Hablutzel 1998). A sensible permeability of  $10^{-6} \text{ cm}^2$  (100 Darcies) was given to the Polycarbon graphite felt.

## Effective Diffusion Coefficient

The Nextel™ 312 preform effective diffusion coefficient function was fitted to experimental diffusivity data of Nicalon™ (Nippon Corporation, Tokyo, Japan)/SiC composite specimens (Starr and Hablutzel 1998). The diffusivity apparatus used in this work was not available for measurement on the Nextel™ 312/SiC specimens. Thus, the diffusivity data for the Nicalon™/SiC composite specimens approximated the density-dependent, porous microstructure of the Nextel™ 312/SiC composite. The actual value of the Nicalon™/SiC effective diffusion coefficient may be somewhat different than that for the Nextel™ 312/SiC composite due to differences in the fiber diameter, fiber bundle density, and fiber weave.

## Preform Surface Area

The preform specific surface area was estimated using a descriptive spherical node/cylindrical bond model developed by Starr (1995). The node and bond radii, length, and number densities that were used in the descriptive model translated to the physical dimensions of the initial tube preform porous microstructure, including the intrabundle, interlaminar, and channel porosity. The node and bond radii and bond lengths used in the model are listed in Table 5-1. The initial specific surface area was adjusted in the node/bond model by changing the number of bond lengths that represented the intrabundle porosity (1500 for a  $1500\text{ cm}^{-1}$  initial value). The percolation threshold, which represents the density when the available specific surface area of the preform becomes

zero, was unknown. Therefore, a normalized theoretical density threshold of 0.9069 was assumed, the value for a hexagonal closed packed system (Perrins et al. 1979).

Table 5-1. Radii and Lengths used in the Starr Node/Bond Model

	<u>Radius(<math>\mu\text{m}</math>)</u>	<u>Length(cm)</u>
Intrabundle Porosity	7	1
Interlaminar Porosity	500	0.05
Channel	1000	N/A

### Emissivity

A constant preform emissivity of 0.87, an average of both Nextel™ 312 (0.88, 3M Corporation) and SiC (0.86, Campbell and Sherwood 1967) was used in the model. Sensible emissivity values used in the model for the Polycarbon graphite felt, Poco graphite, Fiberfrax, and stainless steel were 0.8, 0.99, 0.5, and 0.99 respectively. However, the actual emissivity values for these materials were unknown.

## CHAPTER 6

### FCVI EXPERIMENTAL RESULTS

This chapter discusses the success of the tube preform fabrication, including the results from both compression techniques and the effects of the phenolic resin variation. Infiltration times and theoretical densities are reported for the initial composite tubes, the tube preforms infiltrated using the same process conditions for various time lengths, and the tubes infiltrated with variation in process temperature and total flow. The tube densities determined by both X-ray computed tomography and digital image analysis techniques are provided along with the overall tube densities obtained from final composite mass and volume. The experimental results for both preform permeability and thermal diffusivity for both fiber orientations are listed at the end of the chapter.

#### **Tube Preform Fabrication**

This section presents tube preform fabrication results using both preform compression methods and both phenolic resin-volume percent solutions. These results show the preform compression method and the resin volume-percent solution that produced rigid, free-standing preforms that had no residual carbon on the fiber surface. These favored, fabrication results were then used for all successive tube preforms used in this research.

## **Preform Compression**

Tube preform compression with the Dow J RTV Silastic™ sleeve and the aluminum shim stock resulted in the Nextel™ 312 preform buckling through the gap along its entire length. The use of the aluminum bar stock resulted in the preform buckling around the stock (two buckles) along its entire length. The minimum OD that was reached using the Silastic™ sleeve without buckling was 6.6 cm, slightly greater than the desired preform OD (6.4 mm).

The preform compression with the aluminum tube sections and the aluminum shim stock eliminated the buckling phenomenon outright. The resulting Nextel™ 312 tube preform OD was 6.5 cm, although the preform circumference was slightly ovoid due to the material lost in the aluminum tube slicing.

## **Phenolic Resin Variation**

The use of the initial X-resin volume percent resulted in excess carbon on the fiber surfaces, which consumed a significant proportion of the preform porosity that was to be filled with SiC matrix. Reduction of the resin volume by 3% eliminated the excess carbon while maintaining preform rigidity. The cross-sections of infiltrated, fibrous preforms fabricated with each resin volume percent are shown in Figure 6-1. The dark-gray regions surrounding the fibers represent the carbon, while the light-gray regions represent the SiC matrix.



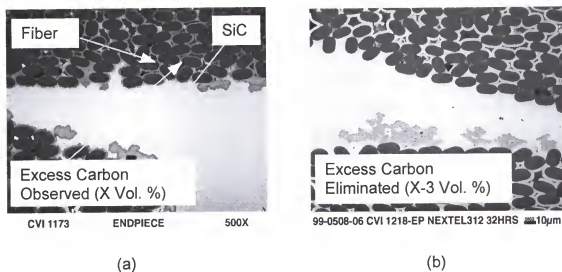


Figure 6-1. The variation of the phenolic resin volume percent and its effect on residual carbon.

a) Excess residual carbon observed with use of an initial X-resin volume percent solution; b) Excess carbon was eliminated using a 3% lower resin volume percent solution.

### Tube Infiltration Results

The following presents the initial tube infiltration efforts that demonstrated the feasibility of the FCVI process for tubes. Tube dimensions, tube characteristics, and process conditions for these Nextel™ 312 preforms are shown in Table 6-1. The tube preforms for CVI 1102 and CVI 1103 were fabricated by Matlin (1995) using a different Nextel™ 312 braided fiber sleeve. The fiber bundles for this sleeve contained approximately twice as many fibers (~1000 fibers) as the fiber bundles seen in the Nextel™ 312 fiber sleeve described in Chapter 3.

The theoretical density of CVI 1102 was undetermined due to sleeve delamination and preform deformation during infiltration. Evidence of delamination is shown in X-ray tomographic images seen in Figure 6-2.

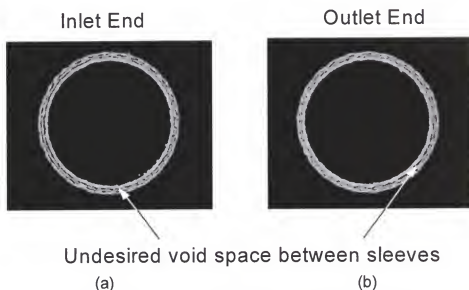


Figure 6-2. X-ray tomographic images indicating delamination of concentric Nextel™ 312 fiber sleeves in CVI 1102.

a) inlet end; b) outlet end.

The infiltration of CVI 1103 yielded a 70-kPa inlet backpressure at 24 hours. The infiltration temperature for CVI 1103 was about 30°C higher (1234°C) than that for CVI 1102 and CVI 1173. A theoretical density of 80% was realized in 24 hours of infiltration. The tube interior of CVI 1103 experienced a significant amount of SiC overcoat seen in X-ray tomographic images taken at the inlet end, center section, and outlet end (Figure 6-3). The SiC overcoat thickness was highest at the middle of the preform and lower at each end, following the observed profile of the experimental coating chamber temperature (Figure 7-1).

The theoretical density of CVI 1103 was determined by subtraction of the estimated SiC overcoat mass (Appendix F).

The final theoretical density for CVI 1173 was 87% and was achieved in 24 hours. The preform fiber volume of CVI 1173 was 50%, somewhat higher than the 35% for the other two preforms (CVI 1102 and CVI 1103). Although, some SiC overcoat was apparent on this tube, the actual amount was uncertain, for X-ray computed tomography was not performed on this tube.

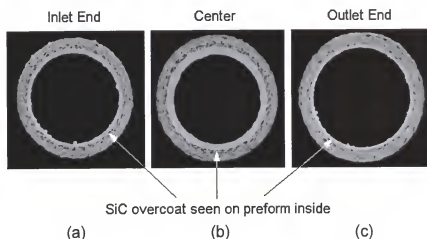


Figure 6-3. Excess SiC overcoat observed with tube CVI 1103.  
a) inlet end; b) center; c) outlet end.

Table 6-1. Initial FCVI Tube Data

	CVI <u>1102</u>	CVI <u>1103</u>	CVI <u>1173</u>
<u>Tube Dimensions</u>			
Inside Diameter(cm)	4.8	4.8	5.1
Thickness(mm)	3.2	6.4	4.1
Length(cm)	35.6	36.8	36.8
<u>Tube Characteristics</u>			
Fiber Volume(%)	50	35	50
Theoretical Density(%)	Undetermined	80	87
<u>FCVI Process Conditions</u>			
Average Mid-Line Coating			
Chamber Temperature(°C)	1209	1234	1202
Hydrogen Flow(slm)	5	5	5
Average $\alpha$ (H <sub>2</sub> /MTS)	7.06	5.05	5.27
Infiltration Time(Hours)	14	24	24

The next Nextel™ 312 tube preform (CVI 1132) that was fabricated varied in thickness along its length and was infiltrated to satisfy an objective of the research sponsor (U.S. D.O.E., Office of Fossil Energy). A diagram of the multi-thick, Nextel™ 312 tube preform is seen in Figure 6-4. Ten concentric Nextel™ 312 sleeves were used for the preform fabrication, with fourteen sleeves used at the thicker, gas inlet end (Section 1).

Tube dimensions, tube characteristics, and process conditions for CVI 1132 are shown in Table 6-2. This tube preform had a fiber volume of 44% reaching 75% theoretical density in 28 hours of infiltration. A slight SiC overcoat was observed on both the interior and the exterior. The SiC overcoat mass was estimated and subtracted from the total composite mass in the theoretical density estimation (Appendix F). Several X-ray tomographic images taken from CVI 1132 are seen in Figures 6-5.

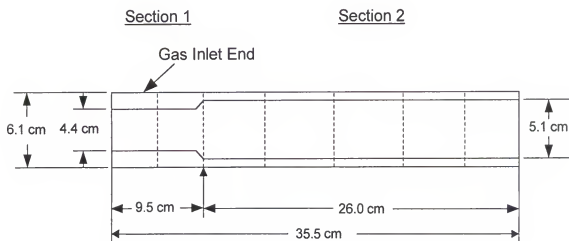


Figure 6-4. Nextel™ 312 tube preform dimensions for CVI 1132.

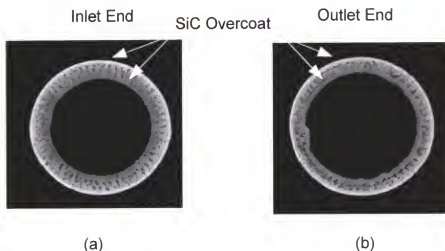


Figure 6-5. X-ray computed tomographic images of CVI 1132.  
a) inlet end; b) outlet end.

Table 6-2. FCVI Tube Data for CVI 1132

	Section 1	Section 2		
<u>Tube Dimensions</u>			<u>Tube Characteristics</u>	
Inside Diameter(cm)	4.4	5.1	Fiber Volume(%)	44
Thickness(mm)	8.3	5.1	Theoretical Density(%)	75
Length(cm)	9.5	26		
<u>FCVI Process Conditions</u>				
Average Mid-Line				
Coating Chamber				
Temperature(°C)	1188			
Hydrogen Flow(slm)	5			
Average $\alpha$ (H <sub>2</sub> /MTS)	5.64			
Infiltration Time(Hours)	28			

The next set of infiltration results includes the Nextel™312/SiC composite tubes that were fabricated for the density characterization, which was performed to evaluate model accuracy. These four Nextel™312 tube preforms (CVI 1211, CVI 1223, CVI 1217, and CVI 1218) were infiltrated with the same process

conditions for infiltration times of 6, 12, 24, and 32 hours respectively. The tube dimensions, tube characteristics, and process conditions for these tubes are seen in Table 6-3. An approximate SiC overcoat thickness of 150  $\mu\text{m}$  and 250  $\mu\text{m}$  was observed on the tube exterior for tubes CVI 1217 and CVI 1218 respectively, and no apparent overcoat was observed on the other tubes (CVI 1211 and CVI 1223).

Table 6-3. FCVI Data for Tubes Infiltrated for Various Time Lengths

	<u>CVI</u> <u>1211</u>	<u>CVI</u> <u>1223</u>	<u>CVI</u> <u>1217</u>	<u>CVI</u> <u>1218</u>
<u>Tube Dimensions</u>				
Inside Diameter(cm)	5	5	5	5
Outside Diameter(cm)	6.6	6.5	6.6	6.7
Thickness(mm)	8.4	7.9	8.4	9
Length(cm)	35.6	35.6	35.6	35.6
<u>Tube Characteristics</u>				
Fiber Volume(%)	35	35	33	32
Theoretical Density(%)	40	54	70	80
Infiltration Time(Hours)	6	12	24	32
<u>FCVI Process Conditions</u>				
Average Mid-Line Coating				
Chamber Temperature( $^{\circ}\text{C}$ )	1206	1198	1194	1190
Hydrogen Flow(slm)	5	5	5	5
Average $\alpha$ ( $\text{H}_2$ /MTS)	5.69	4.94	4.56	4.74

The next set of tube infiltration results includes those with the variation of the process temperature and the total flow rate. These experiments were conducted to observe their effect on total infiltration time (Table 6-4). CVI 1241 was infiltrated at 1246 $^{\circ}\text{C}$  at the coating chamber mid-line, approximately 50 $^{\circ}\text{C}$

higher than the other tubes with the other process parameters remaining the same. A 90% theoretical density was realized in 27 hours of infiltration.

CVI 1248 was infiltrated using a higher coating chamber mid-line temperature and a higher hydrogen flow (1242°C and 7.5 slm) with the hydrogen/MTS molar feed ratio remaining constant ( $\alpha=4.94$ ). The use of the higher total flow reduced the infiltration time from 27 hours to 16 hours.

Both CVI 1241 and CVI 1248 had post-infiltrated fiber volumes of 33%. Averages of measured inside and outside diameters for both tubes were used in the estimates of the fiber volume and the final theoretical density. Tube density characterization was not done on either tube.

Table 6-4. FCVI Tube Data with Varied Process Conditions

	CVI <u>1241</u>	CVI <u>1248</u>
<u>Tube Dimensions</u>		
Inside Diameter(cm)	4.9	5
Thickness(mm)	7.8	6.1
Length(cm)	35.6	35.6
<u>Tube Characteristics</u>		
Fiber Volume(%)	33	33
Theoretical Density(%)	90	88
Infiltration Time(Hours)	27	16
<u>FCVI Process Conditions</u>		
Average Mid-Line Coating Chamber Temperature(°C)	1246	1242
Hydrogen Flow(slm)	5	7.5
Average $\alpha$ ( $H_2$ /MTS)	4.87	4.94

## Tube Density Characterization

This section presents the density profiles obtained by both X-ray computed tomography and digital image analysis techniques. Calibration standards used for both techniques are provided. Sectional and radial density averages and standard deviations are provided with the profiles for each technique to easily analyze the density variation through the tube thickness and along the tube length.

### X-ray Computed Tomography

An uninfiltreated, Nextel™ 312 tube preform (40% theoretical density) and dense Nextel™ 312/SiC specimens (85% theoretical density) of various thickness provided the calibration standards for the X-ray computed tomography. The average Adobe Photoshop™ grayscale values and corresponding theoretical densities for both preform and dense composite specimens are seen in Table 6-5, along with the fitted linear density/grayscale relationship.

Table 6-5. Grayscale Values and Fitted Linear Density Relationship for the Nextel™ 312 Tube Preform and the Dense Nextel™ 312/SiC Specimens

	<u>Theoretical Density</u>	<u>Adobe Photoshop™ Grayscale Value(GS)</u>
Nextel™ 312 Tube Preform	40%	115.5
Nextel™ 312/SiC Specimens	85%	215.6

#### Linear Density/Grayscale Relationship\*

$$\rho(\text{GS}) = a(\text{GS}) + b$$

$$a = 0.00450$$

$$b = -0.01192$$

\* Theoretical density is normalized in the relationship



The theoretical density arrays determined by X-ray computed tomography for tubes CVI 1211, CVI 1223, CVI 1217, and CVI 1218 are provided in Tables 6-6 through 6-9. The section numbers increased from the tube inlet to the outlet with Radial Position 1 corresponding to the tube exterior and Radial Position 4 to the tube interior. The average theoretical densities determined for the four tubes were 37.0%, 52.3%, 65.7%, and 73.0% respectively.

Section and radial density averages and theoretical densities are provided with the density arrays for each tube. The section density averages were lowest at the preform inlet end for all tubes characterized. The highest section density average was found at the middle of the tube length for all tubes except CVI 1223 (12 hours infiltration), where the highest section density average was seen at the gas inlet. The radial density averages monotonically decreased from the tube exterior to the tube interior for all four tubes. The X-ray tomographic images taken from the uninfiltreated Nextel™312 tube preform, Nextel™312/SiC composite specimens, and for all four composite tubes characterized are provided in Appendix G.

Table 6-6. CVI 1211 Density Results from X-ray Computed Tomography

Overall Theoretical Density = 37.0%

Radial Position	Section 1	Section 2	Section 3	Section 4	Section 5	Section 6	Section 7	Radial Averages	Radial Std. Dev.
1	32.8%	50.5%	50.5%	50.5%	50.5%	50.5%	50.5%	48.0%	6.7%
2	32.8%	36.8%	42.5%	51.1%	55.0%	41.3%	34.0%	41.9%	8.4%
3	30.9%	29.6%	29.3%	31.3%	36.4%	31.3%	30.4%	31.3%	2.4%
4	26.4%	27.4%	24.8%	25.4%	31.5%	27.5%	25.8%	27.0%	2.2%
Section Averages	30.7%	36.1%	36.8%	39.6%	43.3%	37.7%	35.2%		
Std. Dev.	3.0%	10.4%	11.8%	13.2%	11.2%	10.4%	10.7%		

Table 6-7. CVI 1223 Density Results from X-ray Computed Tomography

Overall Theoretical Density = 52.3%

<u>Radial Position</u>	<u>Section 1</u>	<u>Section 2</u>	<u>Section 3</u>	<u>Section 4</u>	<u>Section 5</u>	<u>Section 6</u>	<u>Section 7</u>	<u>Radial Averages</u>	<u>Radial Std. Dev.</u>
1	60.9%	70.1%	73.5%	70.8%	72.4%	72.7%	62.5%	69.0%	4.8%
2	51.0%	63.9%	62.1%	61.7%	64.6%	65.2%	52.8%	60.2%	5.4%
3	38.8%	52.6%	49.5%	48.2%	50.9%	50.0%	36.8%	46.7%	5.8%
4	33.7%	46.1%	32.6%	32.1%	32.5%	31.3%	24.1%	33.2%	6.0%
<u>Section Averages</u>	46.1%	58.2%	54.4%	53.2%	55.1%	54.8%	44.1%		
<u>Std. Dev.</u>	12.2%	10.8%	17.5%	16.9%	17.5%	18.3%	17.0%		

Table 6-8. CVI 1217 Density Results from X-ray Computed Tomography

Overall Theoretical Density = 65.7%

<u>Radial Position</u>	<u>Section 1</u>	<u>Section 2</u>	<u>Section 3</u>	<u>Section 4</u>	<u>Section 5</u>	<u>Section 6</u>	<u>Section 7</u>	<u>Radial Averages</u>	<u>Radial Std. Dev.</u>
1	76.9%	79.3%	82.3%	81.2%	81.7%	82.0%	78.3%	80.2%	1.9%
2	60.3%	68.4%	75.9%	76.2%	75.2%	78.0%	74.2%	72.6%	5.8%
3	42.4%	51.5%	66.5%	68.4%	66.1%	68.6%	66.3%	61.4%	9.5%
4	36.3%	36.1%	49.2%	54.9%	53.7%	53.7%	57.1%	48.7%	8.2%
<u>Section Averages</u>	46.3%	52.0%	63.8%	66.5%	65.0%	66.8%	65.9%		
<u>Std. Dev.</u>	18.4%	19.0%	14.4%	11.5%	12.1%	12.6%	9.4%		

Table 6-9. CVI 1218 Density Results from X-ray Computed Tomography

Overall Theoretical Density = 73.0%

<u>Radial Position</u>	<u>Section 1</u>	<u>Section 2</u>	<u>Section 3</u>	<u>Section 4</u>	<u>Section 5</u>	<u>Section 6</u>	<u>Radial Averages</u>	<u>Radial Std. Dev.</u>
1	82.8%	83.1%	83.4%	83.4%	84.1%	83.1%	83.3%	0.4%
2	76.6%	80.0%	78.5%	76.9%	77.5%	78.1%	77.9%	1.1%
3	61.3%	70.7%	75.6%	74.1%	74.4%	73.8%	71.7%	4.9%
4	42.6%	51.3%	61.9%	70.0%	68.2%	61.6%	59.3%	9.6%
<u>Section Averages</u>	65.8%	71.3%	74.9%	76.1%	76.1%	74.2%		
<u>Std. Dev.</u>	17.9%	14.3%	9.2%	5.6%	6.6%	9.2%		

## Digital Image Analysis

The multiphase calibration standard picture used for the BioScan Optimas™ Image Analysis software is seen in Figure 6-6. The concentric circle pattern was produced on Microsoft™ Word97 (Richmond, WA). The comparison of the percent area found manually and by Optimas™ is provided in Table 6-10. The relative error was defined as the ratio of the difference between the manual and Optimas™ grayscale values and the manual grayscale value.

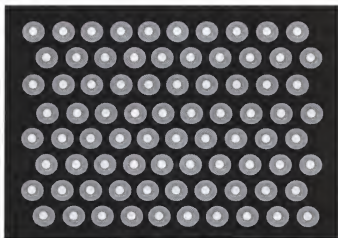


Figure 6-6. Calibration standard used for the BioScan Optimas™ image analysis software. Three different grayscales were chosen to represent distinct grayscale values.

Table 6-10. Manual and Optimas™ Percent Area Comparison (Calibration Std.)

Black Phase	0-50	Grayscale	
Gray Phase	51-140	Grayscale	
White Phase	141-255	Grayscale	
	Bio Scan		
	<u>Manual</u>	<u>Optimas™</u>	<u>Relative Error</u>
Black Phase	57.4%	57.8%	0.8%
Gray Phase	35.7%	35.2%	1.5%
White Phase	6.9%	7.0%	1.4%

\* Relative error at 100% magnification

The calibration standard was analyzed at various magnifications for consistency in the percent area estimates. The relative error for each phase was less than 4% for all magnifications considered (10X to 100X). Relative errors for each phase at various magnifications are seen in Table 6-11.

Table 6-11. Optimas™ Relative Errors of the Calibration Standard Grayscale Phases at Various Magnification

<u>Magnification</u>	<u>Black Phase</u>	<u>Gray Phase</u>	<u>White Phase</u>
100 X	0.8%	1.5%	1.4%
75 X	0.6%	1.2%	1.6%
50 X	0.8%	1.4%	0.4%
25 X	0.9%	1.4%	0.1%
15 X	0.9%	1.6%	0.6%
10 X	2.1%	3.9%	2.4%

An untouched and a retouched digital image taken from tube CVI 1218 are seen in Figure 6-7. The black areas seen in the fiber bundles are damaged regions from specimen preparation and polishing. The void space observed between the fiber bundles had a similar grayscale to that of the Nextel™ fibers. The retouched digital image shows where the epoxy-filled voids were painted with a zero grayscale (black), and where the damaged spots in the fiber bundles were painted with a grayscale representative of the Nextel™ 312 fiber.

The fiber volume and theoretical density arrays determined from digital image analysis for tubes CVI 1217 and CVI 1218 are seen in Tables 6-12 through 6-15 respectively. The average fiber volumes and theoretical densities for tubes CVI 1217 and CVI 1218 were 33.4% and 71.2% and 33.1% and 83.4% respectively. The fiber volume for each data point was subtracted and replaced

with the average tube fiber volume to compensate for variation in the fiber weave. The majority of the theoretical density array for CVI 1217 was between 70-80% while the theoretical density array for CVI 1218 was between 80-90%.

Several data points at the periphery of both density arrays resulted in a lower density. These data points strayed from the density average because of the unrepresentative voids seen in the digital images caused by specimen damage and the apparent voids in the digital image that did not physically exist in the composite specimen. Several selected digital images from runs CVI 1217 and CVI 1218 are found in Appendix H.

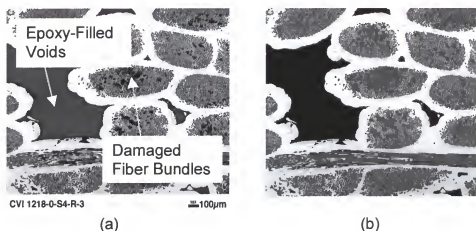


Figure 6-7. Captured digital images of the composite tube cross-section. a) original digital image showing the damaged fiber bundles and the epoxy-filled void space; b) retouched digital image.

Overall theoretical density measurements were performed on Section 3 (tube mid-length) at  $0^\circ$ ,  $90^\circ$ , and  $180^\circ$  for both CVI 1217 and CVI 1218 ( $0^\circ$  at the 12 o'clock position). The overall theoretical densities for CVI 1217 at  $0^\circ$ ,  $90^\circ$ , and  $180^\circ$  were 71.4%, 67.5%, and 74.2%, respectively while the overall theoretical

densities for CVI 1218 at 0°, 90°, and 180° were 76.8%, 75.2%, and 76.8% respectively. Thus, no significant circumferential density variation was apparent for either tube.

Digital image analysis was not performed on CVI 1211 and CVI 1223. The interior Nextel™ 312 fiber layers for these tubes were not densified with SiC matrix, and these layers delaminated upon specimen preparation.

Table 6-12. CVI 1217 Fiber Volumes from Digital Image Analysis

Average Fiber Volume = 33.4%

Radial Position	Section 1	Section 2	Section 3	Section 4	Section 5	Section 6	Radial Averages	Radial Std. Dev.
1	27.6%	38.3%	31.0%	35.7%	28.8%	21.2%	30.4%	5.6%
2	29.4%	32.7%	37.0%	32.3%	27.4%	35.7%	32.4%	3.3%
3	32.4%	34.5%	27.7%	42.8%	35.1%	35.5%	34.7%	4.5%
4	45.1%	37.6%	36.1%	36.2%	33.1%	27.8%	36.0%	5.2%
Section Averages								
	33.6%	35.8%	33.0%	36.8%	31.1%	30.1%		
Std. Dev.								
	7.9%	2.6%	4.4%	4.4%	3.6%	7.0%		

Table 6-13. CVI 1217 Density Results from Digital Image Analysis

Overall Theoretical Density = 71.2%

Radial Position	Section 1	Section 2	Section 3	Section 4	Section 5	Section 6	Radial Averages	Radial Std. Dev.
1	76.9%	63.5%	64.0%	74.0%	54.2%	51.3%	64.0%	10.2%
2	74.9%	67.9%	68.4%	74.1%	65.0%	65.0%	69.2%	4.3%
3	73.0%	80.9%	73.6%	73.5%	77.7%	69.2%	74.7%	4.1%
4	72.9%	72.8%	75.8%	80.9%	81.4%	76.9%	76.8%	3.7%
Section Averages								
	74.4%	71.3%	70.5%	75.6%	69.6%	65.6%		
Std. Dev.								
	1.9%	7.5%	5.3%	3.5%	12.4%	10.7%		

Section 3 Overall Densities

0 Degrees	71.4%	Average	71.0%
90 Degrees	67.5%	Std. Dev.	3.4%
180 Degrees	74.2%		

Overall Pictures @ 12.8 X Magnification  
All Other Pictures @ 50 X Magnification

Table 6-14. CVI 1218 Fiber Volumes from Digital Image Analysis

Average Fiber Volume = 33.1%

<u>Radial Position</u>	<u>Section 1</u>	<u>Section 2</u>	<u>Section 3</u>	<u>Section 4</u>	<u>Section 5</u>	<u>Section 6</u>	<u>Section 7</u>	<u>Radial Averages</u>	<u>Radial Std. Dev.</u>
1	25.2%	30.3%	40.4%	42.0%	32.4%	36.2%	24.6%	33.0%	6.9%
2	26.1%	30.9%	33.3%	27.1%	36.6%	29.3%	39.2%	31.8%	4.9%
3	24.1%	34.6%	29.6%	41.4%	40.0%	33.7%	39.7%	34.7%	6.3%
4	29.0%	30.4%	20.0%	36.5%	36.3%	38.3%	40.5%	33.0%	7.1%
<u>Section Averages</u>	26.1%	31.6%	30.8%	36.8%	36.3%	34.4%	36.0%		
<u>Std. Dev.</u>	2.1%	2.1%	8.5%	6.9%	3.1%	3.9%	7.6%		

Table 6-15. CVI 1218 Density Results from Digital Image Analysis

Overall Theoretical Density = 83.4%

<u>Radial Position</u>	<u>Section 1</u>	<u>Section 2</u>	<u>Section 3</u>	<u>Section 4</u>	<u>Section 5</u>	<u>Section 6</u>	<u>Section 7</u>	<u>Radial Averages</u>	<u>Radial Std. Dev.</u>
1	79.0%	85.2%	82.0%	77.5%	88.1%	84.7%	69.0%	80.8%	6.4%
2	81.9%	86.5%	84.7%	85.6%	78.9%	86.4%	82.8%	83.8%	2.8%
3	82.2%	84.3%	91.0%	82.0%	84.6%	85.7%	82.8%	84.7%	3.1%
4	77.9%	74.1%	94.4%	81.5%	84.4%	79.5%	70.1%	80.3%	7.8%
<u>Section Averages</u>	80.3%	82.5%	88.0%	81.7%	84.0%	84.1%	76.2%		
<u>Std. Dev.</u>	2.1%	5.7%	5.7%	3.3%	3.8%	3.1%	7.7%		
<u>Section 3 Overall Densities</u>									
0 Degrees	76.8%	Average	76.3%	Overall Pictures @ 12.8 X Magnification All Other Pictures @ 50 X Magnification					
90 Degrees	75.2%	Std. Dev.	0.9%						
180 Degrees	76.8%								

A summary of the tube fiber volumes and theoretical densities for tubes CVI 1211, CVI 1223, CVI 1217, and CVI 1218, determined by final composite mass and volume (overall experimental method), X-ray computed tomography, and digital image analysis, is listed in Table 6-16. The tube fiber volumes and theoretical densities from digital image analysis were in excellent agreement with the overall experimental values, while the theoretical densities determined by X-ray computed tomography show the same trend, but were slightly lower. The

greatest discrepancy in the theoretical density results between the X-ray computed tomography and the overall experiment results was seen with CVI 1218 (7%).

Table 6-16. Experimental Comparative Summary of Tube Fiber Volumes and Theoretical Densities

	<b><u>CVI 1211</u></b>	<b><u>CVI 1223</u></b>	<b><u>CVI 1217</u></b>	<b><u>CVI 1218</u></b>
Infiltration Time(Hours)	6	12	24	32
<b><u>Preform Fiber Volume</u></b>				
Overall(%)	35	35	33	32
Digital Image Analysis(%)	N/A	N/A	33	33
<b><u>Theoretical Density</u></b>				
Overall(%)	40	54	70	80
X-ray CT(%)	37	52	66	73
Digital Image Analysis(%)	N/A	N/A	71	83

### **Preform Transport Property Measurement**

This section presents the experimental results of the permeability and the laser-flash thermal diffusivity measurements. The permeabilities for both fiber orientations are listed in a density-dependent tabular form. The laser-flash thermal diffusivities for various composite theoretical densities are listed in a temperature-dependent tabular form.



## Permeability Measurements

The permeability results for the Nextel™312/SiC specimens at varied density are shown in Table 6-17. The parallel permeability values were slightly greater than the perpendicular values and monotonically decreased with density for both fiber orientations. The higher parallel permeabilities were due to the pores that existed in the composite specimens (large fiber braid channels). A Microsoft™ Excel98 spreadsheet used to determine the specimen permeability from the experimental specimen pressure drop data and the corresponding total flow data is found in Appendix E.

Table 6-17. Nextel™312/SiC Specimen Permeabilities

Perpendicular Permeability		Parallel Permeability	
<u>Theoretical Density</u>	<u>[Darcies]</u>	<u>Theoretical Density</u>	<u>[Darcies]</u>
59.7%	460.2	66.4%	813.0
60.2%	145.5	70.7%	254.4
74.4%	73.8	77.2%	155.0
79.4%	22.4	78.2%	125.2
85.8%	0.1	80.3%	51.8

## Laser-Flash Thermal Diffusivity Measurements

The perpendicular laser-flash thermal diffusivity results for Nextel™312/SiC specimens of varied density are presented in Table 6-18 while the parallel laser-flash thermal diffusivity results are presented in Table 6-19. The perpendicular thermal diffusivities monotonically decreased with temperature at a given theoretical density and increased with density at a given temperature. Parallel thermal diffusivities increased with density at a given temperature and

displayed a maximum with temperature at a given density. These thermal diffusivity data were used to calculate the Nextel™312/SiC composite thermal conductivities for both fiber orientations.

Table 6-18. Perpendicular Thermal Diffusivities of Four Nextel™312/SiC Specimens of Varied Theoretical Density

Temperature (°C)	⊥ Thermal	⊥ Thermal	⊥ Thermal	⊥ Thermal
	Diffusivity ( $\alpha$ )	Diffusivity ( $\alpha$ )	Diffusivity ( $\alpha$ )	Diffusivity ( $\alpha$ )
	[cm <sup>2</sup> /sec] ( 59.7% TD)	[cm <sup>2</sup> /sec] (63.2% TD)	[cm <sup>2</sup> /sec] ( 68.2% TD)	[cm <sup>2</sup> /sec] ( 79.4% TD)
103	0.0120	0.0159	0.0195	0.0511
198	0.0111	0.0141	0.0179	0.0444
298	0.0103	0.0133	0.0166	0.0384
398	0.0098	0.0130	0.0159	0.0346
506	0.0093	0.0124	0.0152	0.0314
622	0.0099	0.0097	0.0139	0.0281
701	0.0099	0.0105	0.0134	0.0275
800	0.0100	0.0107	0.0127	0.0262
901	0.0100	0.0105	0.0128	0.0250
1003	0.0093	0.0108	0.0122	0.0231
1102	0.0096	0.0100	0.0122	0.0215
1206	0.0085	0.0073	0.0103	0.0198

Table 6-19. Parallel Thermal Diffusivities of Three Nextel™ 312/SiC Specimens of Varied Theoretical Density

Temperature (°C)	Thermal	Thermal	Thermal
	Diffusivity ( $\alpha$ )	Diffusivity ( $\alpha$ )	Diffusivity ( $\alpha$ )
	[cm <sup>2</sup> /sec] ( 70.7% TD)	[cm <sup>2</sup> /sec] (75.8% TD)	[cm <sup>2</sup> /sec] ( 80.3% TD)
104	0.0084	0.0169	0.0147
218	0.0170	0.0240	0.0263
301	0.0156	0.0209	0.0232
403	0.0160	0.0207	0.0234
505	0.0170	0.0204	0.0234
625	0.0223	0.0224	0.0302
700	0.0244	0.0239	0.0302
799	0.0245	0.0247	0.0312
899	0.0244	0.0242	0.0309
999	0.0237	0.0240	0.0291
1100	0.0229	0.0233	0.0292
1203	0.0188	0.0205	0.0257

## CHAPTER 7

### FCVI PROCESS MODEL RESULTS

This section presents the results produced by GTCVI. The tube preform theoretical density and temperature profiles at specific time intervals predict the transient tube densification behavior. Changes observed in the theoretical density profiles reflected the temperature profiles, where tube preform regions of higher density yielded higher absolute temperatures and lower radial temperature differences. Transient average tube theoretical density profiles extracted from the transient model output files demonstrated the preform densification rate and total process time required for sufficient density achievement. The FCVI parameter variation and its effects on the preform densification rate and the total process time demonstrated which process conditions minimized the total process time while achieving an acceptable tube density.

#### **Model Input**

The convergence criteria specified in GTCVI for the temperature, pressure, and the MTS and HCl concentrations are listed in Table 7-1. Model iteration terminated when each parameter change between consecutive iterations became less than the specified convergence criterion value.

Table 7-1. GTCVI Parameter Convergence Criteria.

Parameter	Convergence Criteria
Temperature	1E-04 Celsius
Pressure	1E-06 kPa
MTS Mole Fraction	1E-03
HCl Mole Fraction	1E-02

The measured coating chamber temperatures from infrared thermometry (Table 7-2) were used to develop the axial parabolic temperature profiles seen in Figure 7-1 by fit to a parabolic function (Equation 7-1). These profiles span the 49 axial elements used in the model domain. The standard temperature profiles were the averages of experimental infrared thermometer measurements taken from tubes CVI 1211, CVI 1223, CVI 1217, and CVI 1218 while the high temperature profiles were taken from the average experimental infrared thermometer measurements for tubes CVI 1241 and CVI 1248. The average temperature profile was just the calculated average of both standard and high temperature profiles. This average temperature profile, along with the standard and high temperature profiles, were used in the process parameter variation performed to determine the lowest total process time while achieving an acceptable density.

$$T(N) = a + bN + cN^2 \quad (7-1)$$

where      a,b,c = constant [°C]  
               N = axial node [Dimensionless]  
               T = temperature [°C]

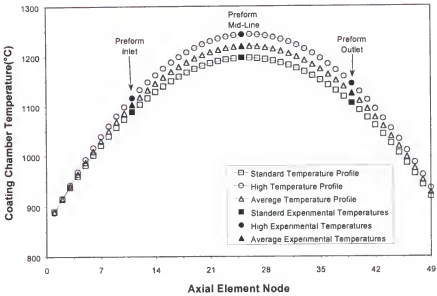


Figure 7-1. Coating chamber temperature profiles used in GTCVI.

Table 7-2. Infrared Thermometer Measurements at the Coating Chamber

	Inlet Side Temperature	Mid-Line Temperature	Outlet Side Temperature
Standard	1089°C	1197°C	1106°C
Average	1103°C	1220°C	1126°C
High	1117°C	1244°C	1145°C

All other boundary conditions input to GTCVI are shown in Table 7-3. The total molar flux was found by dividing the total molar flow by the injector cross-section used in the model domain discretization (2.74 cm<sup>2</sup>) (Appendix D). The total molar flux and the MTS molar feed fraction were averages of tubes CVI 1211, CVI 1223, CVI 1217, and CVI 1218. The SiC deposition rate law and associated parameters used were the same as those seen in Chapter 4. The total infiltration times for each time interval are listed in Table 7-4.

Table 7-3. GTCVI Boundary Conditions

Total Molar Flux*	1.63E-3 mol/cm <sup>2</sup> sec
MTS Feed Mole Fraction	0.16722
HCl Feed Mole Fraction	0
Cooling Line Temperature	50°C
Gas Exhaust Pressure	100 kPa
Boundary Ends	250°C

\* Injector Cross-Sectional Area = 2.74 cm<sup>2</sup>

Table 7-4. GTCVI Infiltration Time Interval Table

Time Step	Infiltration Time(Hours)	Time Step	Infiltration Time(Hours)
0	0	15	12
1	0.5	16	14
2	1	17	16
3	1.5	18	18
4	2	19	20
5	2.5	20	22
6	3	21	24
7	4	22	25
8	5	23	26
9	6	24	27
10	7	25	28
11	8	26	29
12	9	27	30
13	10	28	31
14	11	29	32

### Material Transport Properties

The Nextel™ 312 preform specific surface area, permeability, effective diffusion coefficient, and thermal conductivity were input into GTCVI as functions of density. The preform specific surface area, permeability, and effective diffusion coefficient were input to the model in tabular form while the fitted

preform thermal conductivity parameters were input for both fiber orientations (Equation 5-22).

The Nextel™ 312 preform specific surface area functions used in the model are shown in Figure 7-2. These three surface area functions have similar shape with their only difference lying in the initial value of the specific surface area, since the initial surface area available for deposition in the preform was uncertain. The upper-limit of the initial specific surface area ( $1500 \text{ cm}^{-1}$ ) was determined from the initial fiber volume and effective fiber radius ( $\sim 40\%$  and  $5.5 \mu\text{m}$ ).

The uncertainty in the initial specific surface area arose from the Nextel™ ovoid fiber cross-section and the preform compression, which resulted in some initial fiber contact, thus reducing the available initial specific surface area. Transient average density profiles using all three specific surface area functions were calculated and compared with the overall experimental tube densities.

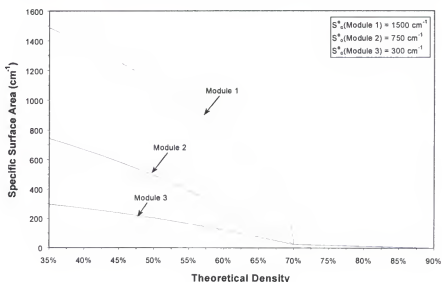


Figure 7-2. Specific surface area functions for the Nextel™ 312 preform.

The preform effective diffusion coefficient (Starr 1998), which monotonically decreased with density, is shown in Figure 7-3. The sharp decrease in the effective diffusion coefficient appearing around 70% theoretical density occurred when the intrabundle porosity became no longer accessible. This abrupt occurrence at 70% theoretical density agreed with that demonstrated with the specific surface area functions.

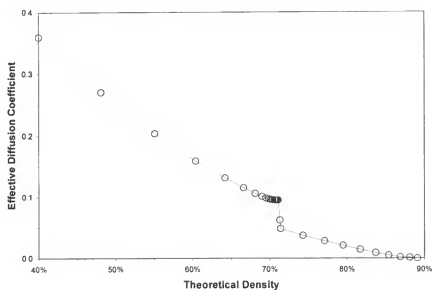


Figure 7-3. Effective diffusion coefficient function used for the tube preform.

The perpendicular and parallel preform thermal conductivity parameters calculated from the experimental laser-flash thermal diffusivity data (Tables 6-18 and 6-19) are shown in Table 7-5. The thermal conductivities for both fiber orientations increased with theoretical density. The parallel thermal conductivities were higher than the perpendicular thermal conductivities for all theoretical densities except at 80%. The higher parallel thermal conductivity



values resulted from the continuous fiber phase in this direction and fewer fiber/matrix phase interfaces.

The thermal conductivities at each theoretical density for both fiber orientations were averaged over the temperature range used in the laser flash-thermal diffusivity measurements (100-1200°C). The temperature dependence in the thermal conductivity function (Equation 5-22,  $c=0$ ) was removed because the apparent thermal conductivity change in the temperature range that the tube preform experiences was slight (1000-1150°C).

The experimental permeability data and the respective fitted logarithmic functions for both fiber orientations (Table 6-17) are shown in Figure 7-4. The parallel permeabilities were slightly higher than the perpendicular permeabilities due to the large pores (interstitial channels) seen with these specimens. At a theoretical density of 80%, the permeabilities for both fiber orientations sharply decreased, indicating the latter stages of infiltration.

Table 7-5. Nextel™ 312/SiC Thermal Conductivity Data

	<u>Perpendicular</u> <u>Thermal Conductivity</u> <u>Constants: (Equation 5-22)</u>	<u>Parallel</u> <u>Thermal Conductivity</u> <u>Constants: (Equation 5-22)</u>
	a = b = c =	-250.1 211.7 0
		-100.3 95.6 0
Theoretical	<u>Perpendicular</u>	<u>Parallel</u>
<u>Density</u>	<u>Thermal Conductivity[W/cm K]</u>	<u>Thermal Conductivity[W/cm K]</u>
40%	0.0090	0.0180
45%	0.0101	0.0198
50%	0.0115	0.0220
55%	0.0135	0.0247
60%	0.0162	0.0282
65%	0.0204	0.0329
70%	0.0273	0.0394
75%	0.0415	0.0491
80%	0.0861	0.0651

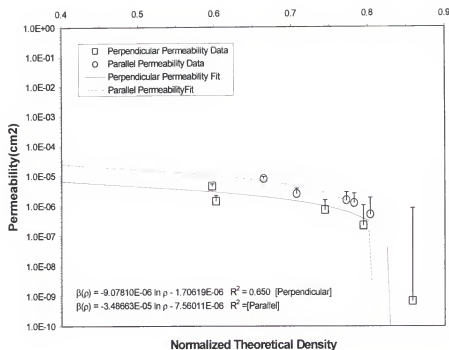


Figure 7-4. Nextel™ 312/SiC preform perpendicular and parallel permeability functions.

The constant Nextel™ 312 preform emissivity value used in the model was 0.87, which is an average of both SiC (0.86, Campbell and Sherwood 1967) and Nextel™ 312 fiber (0.88, 3M Corporation, Saint Paul, MN).

### Other Associated Materials

The thermal conductivities and the respective thermal conductivity function parameters for the Carborundum Fiberfrax™ insulation (Niagara Falls, NY), Polycarbon graphite felt insulation (Valencia, CA), and Poco Graphite (Decatur, TX) are shown in Table 7-6. These data were obtained from their respective manufacturers. Relevant transport properties for all other associated materials used in the model are seen in Table 7-7.

Table 7-6. Thermal Conductivity Data for Carborundum Fiberfrax™, Polycarbon Graphite Felt, and Poco H451 Graphite

Thermal Conductivity

Function Constants: (Equation 5-22)

	<u>Carborundum Fiberfrax</u>	<u>Polycarbon Graphite Felt</u>
a=	0	0
b=	1.338E+07	1.068E+05
c=	1.429	0.810

	<u>Fiberfrax Thermal</u>	<u>Graphite Felt Thermal</u>
<u>Temperature(°C)</u>	<u>Conductivity[W/cm K]</u>	<u>Conductivity[W/cm K]</u>
25	7.425E-06	1.270E-04
100	5.380E-05	3.903E-04
200	1.448E-04	6.843E-04
400	3.898E-04	1.200E-03
600	6.957E-04	1.666E-03
800	1.049E-03	2.104E-03
1000	1.443E-03	2.520E-03
1200	1.873E-03	2.922E-03

Poco H451 Graphite

Thermal Conductivity

Function Constants: (Equation 5-22)

	<u>Against Grain</u>	<u>With Grain</u>
a=	0	0
b=	0.025	0.0275
c=	-0.585	-0.550

	<u>Thermal Conductivity[W/cm K]</u>	<u>Thermal Conductivity[W/cm K]</u>
<u>Temperature(°C)</u>	<u>(Against Grain)</u>	<u>(With Grain)</u>
900	0.748	0.863
1000	0.703	0.814
1100	0.665	0.773
1200	0.632	0.736

Table 7-7. Transport Properties for Other Associated Materials

	Carborundum <u>Fiberfrax</u>	Polycarbon <u>Graphite Felt</u>	Poco <u>Graphite</u>	<u>Stainless Steel</u>
Permeability [Darcies]	1	100	N/A	N/A
Emissivity [Dimensionless]	0.5	0.8	0.99	0.99
Thermal Conductivity [W/cm K]	*	*	**	0.3†

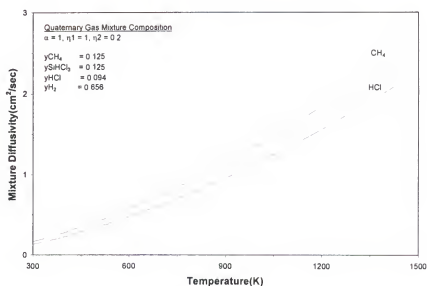
\* See Table 7-5

\*\* See Table 7-6

† (Weast 1995)

### Gas Mixture Transport Properties

The calculated mixture molecular diffusivities and quaternary gas mixture composition for  $\text{CH}_4$  and  $\text{HCl}$  are shown in Figure 7-5, and the calculated functions for the mixture viscosity, heat capacity, and thermal conductivity are shown in Figure 7-6. The  $\text{CH}_4$  diffusivity function was used to describe the MTS transport, since  $\text{CH}_4$  was found to limit the  $\text{SiC}$  deposition rate (Allendorf et al. 1994).

Figure 7-5. Quaternary mixture molecular diffusivities for  $\text{CH}_4$  and  $\text{HCl}$ .

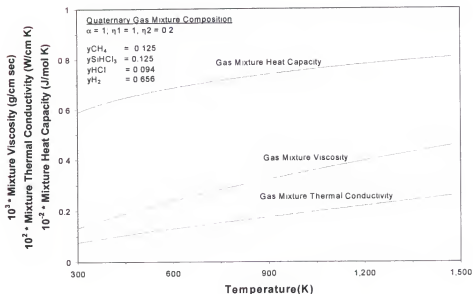


Figure 7-6. Quaternary gas mixture viscosity, heat capacity, and thermal conductivity functions.

## Model Results

The GTCVI source code simulated the CVI process through multiple, steady-state intervals. Temperature and theoretical density profiles were inspected at several of these time intervals. Transient radial temperature difference curves demonstrated conduction and gas convection effects, while transient average theoretical density curves indicated densification rates and total infiltration times necessary for achieving adequate density. Transient radial deposition rates for each radial volume element, demonstrating the density progression, are presented along with gas flow plots that display the gas velocity distribution in the densifying preform. The FCVI process parameters were varied

to determine their effects on the total infiltration time. From this work, process conditions were suggested that minimize the total process time while achieving a acceptable tube density (80%).

### **Preform Temperature Profiles**

The tube preform temperature profiles at the start of infiltration and after 28 hours of infiltration are seen in Figures 7-7 and 7-8 and resemble the parabolic coating chamber temperature profile seen in Figure 7-1. The apparent bulges seen in both temperature profiles slightly to the right of the gas injector inlet were caused by convective gas cooling from the hydrogen/MTS gas mixture.

The average radial temperature difference was calculated from the average tube exterior temperature (Radial Element 1) and the tube interior temperature (Radial Element 4). As expected, the absolute radial temperature difference is much lower at 28 hours of infiltration (23.2°C) than at the start of infiltration (92.9°C) (Figure 7-9), indicative of the higher thermal conductivity from sufficient SiC matrix deposition. Initially, the highest preform temperature difference was seen in the region directly above the gas inlet due to the dominant gas convection. After 28 hours of infiltration, the highest radial preform temperature difference was seen at the tube preform outlet end, where the absolute theoretical density was lower (higher permeability) and the gas convection was highest.

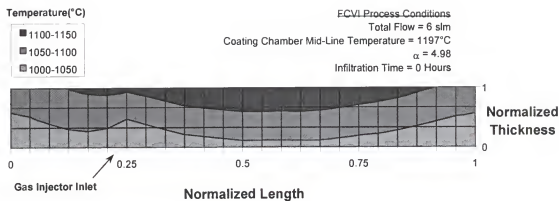


Figure 7-7. Initial Nextel™ 312 preform temperature profile.

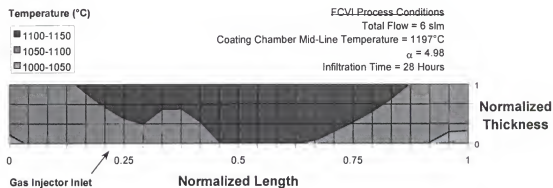


Figure 7-8. Nextel™ 312 preform temperature profile at 28 hours of infiltration.

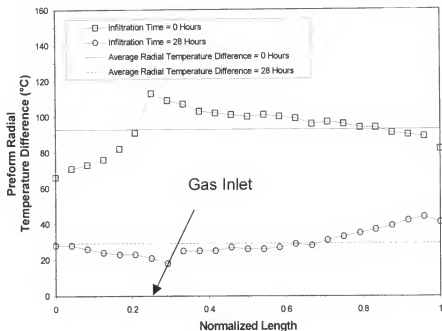


Figure 7-9. Variation of the radial temperature difference along the preform length initially and at 28 hours of infiltration. Average radial preform temperature differences for each time are also provided.

Transient average preform radial temperature difference curves for three total flows are seen in Figure 7-10. The average preform temperature difference was highest at the start of infiltration and monotonically decreased with time due to the continual addition of SiC matrix. Higher total flows increased both the initial radial temperature difference and the radial temperature difference rate change. The higher initial radial temperature difference seen with higher total flow was directly related to higher gas convection, for the entire preform is at the same density. The rate change in the radial average preform temperature difference increased with the total flow due to the increase in SiC matrix deposition, supported by higher preform interior temperatures and greater MTS precursor transport.



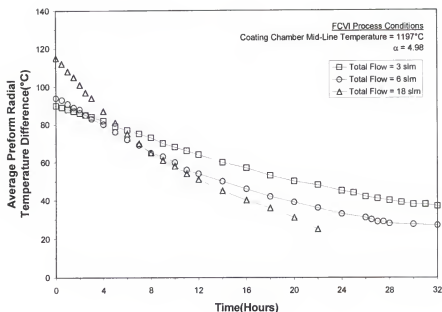


Figure 7-10. Transient preform radial temperature difference curves of the Nextel™ 312 preform with variation of the total flow.

### Transient Average Theoretical Density Profiles

Transient average theoretical density curves using the three specific surface area functions are shown in Figure 7-11. All three theoretical density curves had a similar shape with the absolute density decreasing as the initial specific surface area decreased. Also shown in this figure are the average experimental tube densities of CVI 1211, CVI 1223, CVI 1217, and CVI 1218, which most closely agreed with the model results that used a  $300 \text{ cm}^{-1}$  initial specific surface area (Module 3). The reason for the agreement with the low initial specific surface area module is best explained by the reduction in the available surface area caused by fiber contact, which was enhanced by the close packing of the ovoid cross-sections and the preform compression.

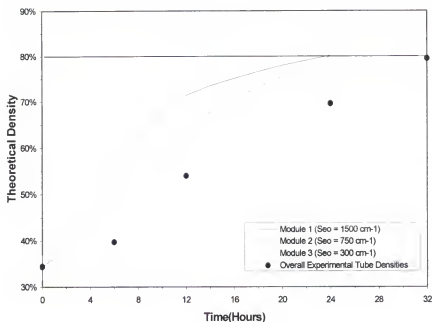


Figure 7-11. Transient average theoretical density curves for the Nextel™ 312 preform using the three different specific surface area functions.

Transient average tube density curves using the SiC deposition parameters found by both Chiang (1999) and Besmann et al. (1991) are presented and compared along with the overall experimental tube theoretical densities (Figure 7-12). The specific initial surface area function of  $1500 \text{ cm}^{-1}$  was used with the Chiang parameters while the specific surface area function with a  $300 \text{ cm}^{-1}$  initial value was used with the Besmann SiC deposition parameters. All other FCVI process conditions were held constant. A table listing the SiC deposition parameters determined by both Besmann and Chiang (Equation 4-4) is seen in Table 7-8.

Table 7-8. Besmann and Chiang SiC Deposition Parameters (Equation 4-4).

	<b>Besmann</b>	<b>Chiang</b>
$E_{af}$ [kJ/mol]	102.7	104.0
$E_{ar}$ [kJ/mol]	-168.6	-591.9
$k_{r0}$ [mol/cm <sup>2</sup> sec]	5.26E-03	6.32E-03
$k_{r0}$ [dimensionless]	3.60E-05	4.70E-20

Both model results for the transient average density were similar initially. The transient average density curve using the Chiang parameters overpredicted at 6 hours and underpredicted the experimental tube densities at 12, 24, and 32 hours, while the transient average density curve using the Besmann deposition parameters slightly overpredicted the experimental tube densities at all four infiltration times. The use of a lower, initial value-specific surface area function with the Chiang deposition parameters made the predicted average densities even lower. The underprediction with the Chiang SiC deposition parameters arose from the stronger HCl inhibition effects (lower  $k_{r0}$ ,  $E_{ar}$ ).

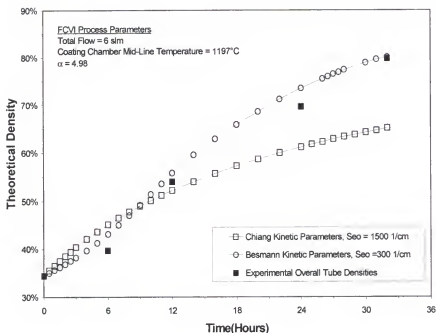


Figure 7-12. Transient average density curves using SiC deposition parameters provided by Chiang (1999) and Besmann et al. (1991).

### Tube Density Profiles

The Nextel™ 312 tube preform theoretical density profiles at six, 12, 24, and 28 hours of infiltration are seen in Figures 7-13 through 7-16, respectively. Average overall tube theoretical densities were 43.1%, 55.8%, 73.5%, and 77.4% respectively.

After six hours of infiltration, the highest preform density at the tube exterior was located slightly to the right of the gas injector inlet. Lower absolute theoretical densities were observed at both preform ends. These trends seen in the density profiles reflected the coating chamber temperature profile (Figure 7-1). Similar density profiles, but with higher absolute theoretical densities, were seen at 12, 24, and 28 hours of infiltration. These profiles demonstrated that the

preform region slightly to the right of the gas injector inlet experienced the fastest densification rate, for it experienced the highest MTS precursor concentration. At 28 hours of infiltration, the majority of the tube theoretical density was between 75-85% with both tube preform ends between 65-75% theoretical density.

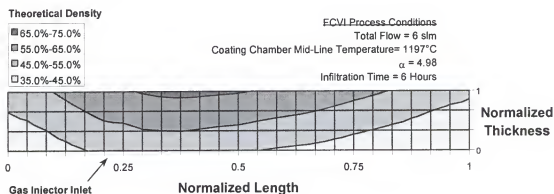


Figure 7-13. Nextel™ 312 theoretical density profile at six hours of infiltration.

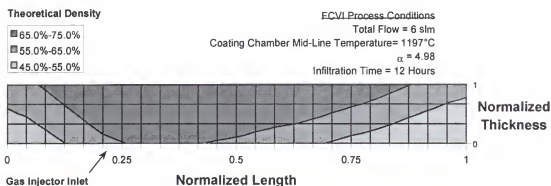


Figure 7-14. Nextel™ 312 preform theoretical density profile at 12 hours of infiltration.

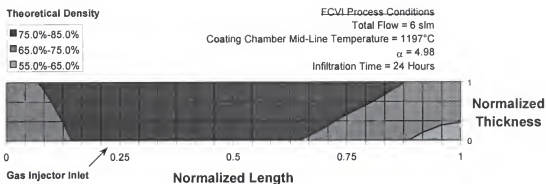


Figure 7-15. Nextel™ 312 preform theoretical density profile at 24 hours of infiltration.

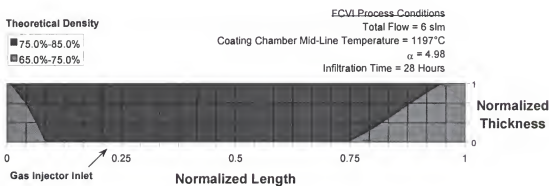


Figure 7-16. Nextel™ 312 preform theoretical density at 28 hours of infiltration.

## Average Radial SiC Deposition Rate Profiles

Transient average deposition rate profiles for each radial element are seen in Figure 7-17. The average SiC deposition rate for each radial element was calculated from all 29 axial elements in the preform. At the start of infiltration, the SiC deposition rate was highest at the preform exterior (Radial Element 1). The average deposition rate profiles for Radial Element 1 and 2 peaked initially and monotonically decreased with time. The deposition rate profiles for Radial Elements 3 and 4 increased with time and reached a maximum, with the rate maximum for Radial Element 4 occurring later than the maximum in Radial Element 3. Therefore, the transient progression in the SiC deposition rate maximum translated from the preform exterior to the interior.

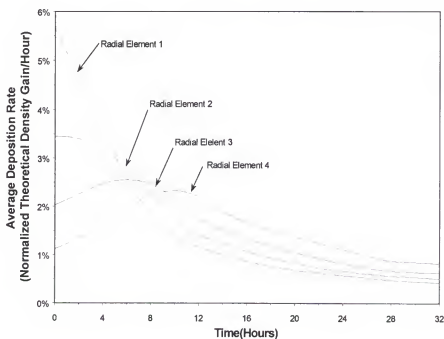


Figure 7-17. Transient average radial deposition rates in the Nextel™ 312 preform. The deposition rate maximum transiently shifts from Radial Element 1 (Preform exterior) to Radial Element 4 (Preform interior).

## FCVI Process Parameter Variation

Variations of the FCVI process parameters and their effects on average tube theoretical density and total infiltration time were investigated. Average tube theoretical density curves with variation of the coating chamber temperature indicated that higher infiltration temperatures resulted in more rapid densification and lower infiltration time (Figure 7-18). Average tube theoretical density curves with variation in  $\alpha$ , the hydrogen/MTS molar feed ratio, also showed that higher MTS concentration also sped infiltration and lowered infiltration time (Figure 7-19). Higher total flow sped infiltration for the majority of the infiltration with a minimum in infiltration time seen at 18 slm (Figure 7-20). At a higher total flow (30 slm), the total infiltration time again increased due to lower densification at the preform outlet ends due to lower temperatures (gas convection).

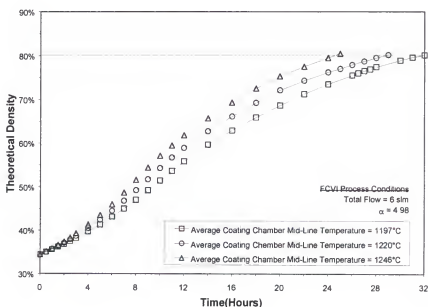


Figure 7-18. Transient average theoretical density curves for the Nextel™ 312 preform with variation of the coating chamber mid-line temperature.



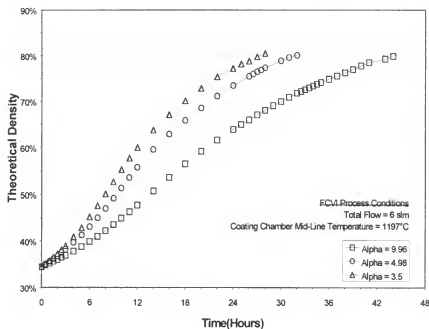


Figure 7-19. Transient average theoretical density curves for the Nextel™ 312 preform with variation of  $\alpha$ .

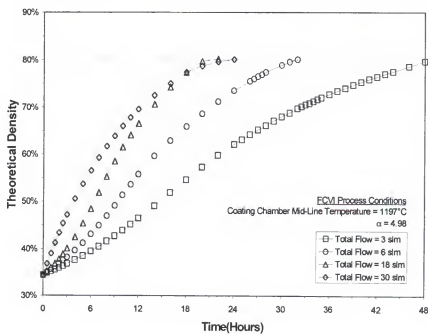


Figure 7-20. Transient average theoretical density curves for the Nextel™ 312 preform with variation of the total flow.

## Gas Flow Profiles

Gas flow vector profiles, through the tube preform, at the beginning and end of infiltration are seen in Figures 7-21 and 7-22, respectively. At the start of infiltration, the gas flowed through the preform with a maximum seen near the gas injector inlet. At the end of infiltration, essentially all of the gas flow occurred at the preform outlet end where the theoretical density was lowest and the permeability was highest.

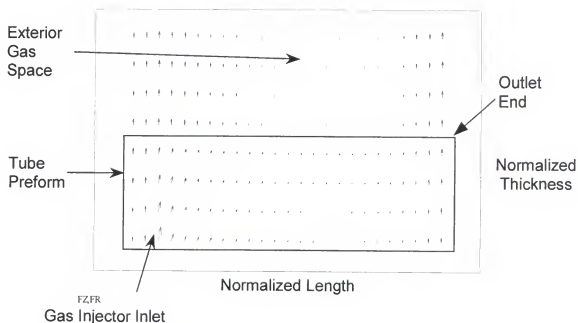


Figure 7-21. Gas flow vector profile at the start of infiltration. The flow is highest near the gas injector inlet.

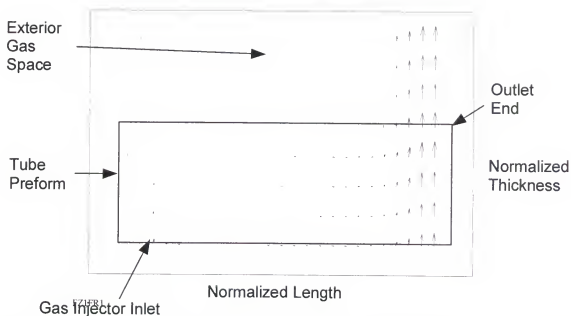


Figure 7-22. Gas flow vector profile near the end of infiltration (28 Hours). Flow dominates through the tube and preform outlet end.

### Total Infiltration Time

Total infiltration times that resulted in an average tube theoretical density of 80% using various temperatures and total flows are seen in Table 7-9. For each flow rate, an increase in coating chamber temperature reduced the total infiltration time. For each coating chamber temperature, a minimum in total infiltration time was seen at 18 slm. Infiltration times at 30 slm were slightly higher due to lower SiC deposition in the tube preform outlet ends from lower temperatures (gas convection and furnace temperature profile).

### Most Favorable FCVI Process Conditions

The FCVI process conditions of 1244°C at the coating chamber mid-line, 18 slm of total flow, and an  $\alpha$ -value of 4.98 yielded 80% theoretical density with the lowest total process time (15.9 hours). A theoretical density profile using these process conditions at 15 hours of infiltration time is shown in Figure 7-23 with the interior length section between 80-85%. However, theoretical densities of 65-75% were seen at both tube ends. Again, the lower densities observed at both preform ends were due to the lower temperature.

Table 7-9. Total Infiltration Time (Hours) Matrix with  $\alpha=4.98$

Coating Chamber Mid-Line	Total Flow				
<u>Temperature</u>	<u>3 slm</u>	<u>6 slm</u>	<u>18 slm</u>	<u>30 slm</u>	
1197°C	48.5	31.8	21.2	23.6	
1220°C	45.0	28.7	17.0	21.7	
1244°C	40.3	24.5	15.9	18.4	

Theoretical Density

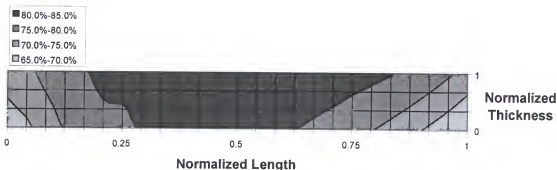


Figure 7-23. Nextel™ 312 preform theoretical density profile at 15 hours of infiltration with the FCVI process conditions resulting in the lowest process time (1244°C, 18 slm, and  $\alpha = 4.98$ ).

A summary of the fiber volumes and theoretical densities for tubes CVI 1211, CVI 1223, CVI 1217, and CVI 1218 predicted by the overall experimental methods, X-ray computed tomography, digital image analysis, and the GTCVI model is presented in Table 7-10. The average tube densities at the intermediate infiltration times were in reasonable agreement with all considered density measurement methods.

Table 7-10. Model/Experiment Comparative Summary of Tube Fiber Volumes and Theoretical Densities

	<u>CVI 1211</u>	<u>CVI 1223</u>	<u>CVI 1217</u>	<u>CVI 1218</u>
Infiltration Time(Hours)	6	12	24	32
<u>Preform Fiber Volume</u>				
Overall(%)	35	35	33	32
Digital Image Analysis(%)	N/A	N/A	33	33
<u>Theoretical Density</u>				
Overall(%)	40	54	70	80
X-ray CT(%)	37	52	66	73
Digital Image Analysis(%)	N/A	N/A	71	83
GTCVI(%)	43	56	74	80

## CHAPTER 8

### DISCUSSION

This chapter presents the discussion of all the pertinent phases in this research. Physical observations and interesting occurrences in the experimental infiltrations are addressed. Results and characteristic patterns of the preform transport properties are discussed and compared to composite transport property results that exist in the literature. The results of both density characterization techniques are evaluated while addressing distinct features from each. The GTCVI model results, demonstrating transient tube density progression and parameter effects on densification rate and total infiltration time, are discussed. The GTCVI model validation, by appropriate parameter adjustment, is presented, while the lowest total process time found with the model is compared to the times realized with the experimental tube infiltrations using higher process temperature and total flow rate. The density profiles produced by GTCVI are compared to the profiles extracted from the density characterization to evaluate the effectiveness of the model predictability of the FCVI process.

#### **Tube Infiltrations**

The tube theoretical densities achieved with 1197°C coating chamber mid-line temperature, 6 slm total flow, and a  $\alpha$ -value of five, increased with longer

infiltration times, from 40% theoretical density with 6 hours of infiltration to 80% theoretical density with 32 hours of infiltration. For CVI 1211 (6 hours infiltration), only the tube exterior appeared dense with SiC while the rest of the tube preform appeared black from the pyrolyzed carbon. The density increased from the tube exterior to the tube interior as the infiltration time increased, indicating that the SiC deposition advanced in this manner. This observation confirmed the successful application of a temperature gradient across the preform thickness.

Infiltration with a higher coating chamber temperature (1246°C), keeping all other process conditions constant, reduced the process time from 32 hours to 27 hours, and infiltration with both a higher coating chamber temperature (1242°C) and a higher total flow (9 slm) reduced the total process time by one-half to 16 hours. These experimental infiltration results indicated that an increase in both the process temperature and the total flow had dramatic effects on the total process time.

The only tube preform that achieved a 70 kPa-gas inlet backpressure at the end of infiltration was CVI 1103. The gas inlet backpressure was realized because the Fiberfrax™ disks used to seal the preform ends were almost completely densified with SiC matrix. Only the Fiberfrax™ disk region in the vicinity of the cooling line was not completely densified with SiC. Low permeability in the dense, tube preform and the dense Fiberfrax™ forced the reactive hydrogen/MTS mixture to deposit SiC on the tube interior. Use of the Fiberfrax™ disks was successful in containing the reactive hydrogen/MTS gas mixture inside the tube preform. However, significant gas inlet backpressures at

the end of infiltration were not realized as compared to the steep backpressures observed with the infiltration of fibrous disk preforms (Stinton et al. 1986). The reason for the lack of inlet backpressure was due to both the semi-permeability of the Fiberfrax™ material and the graphite glue seal bonding the Fiberfrax™ and the tube preform.

During the course of infiltration, the required transformer power necessary to maintain a constant coating chamber temperature gradually increased due to the increase in preform thermal conductivity. The higher preform thermal conductivity from the SiC matrix enhanced the heat flux through the preform, forcing higher temperature and associated higher radiation losses at the tube preform interior.

The carbon soot that appeared on the tube exterior and the coating chamber interior after infiltration could be easily removed with thorough scrubbing with water and a wire brush. The carbon soot arose from the significant MTS depletion (high HCl content) seen in this tube preform region, with the most likely carbonaceous species responsible for the carbon deposit being either  $\text{CH}_4$  or  $\text{CH}_3$ -radical (Allendorf et al. 1994).

The apparent SiC overcoat seen on both tube surfaces for some of the infiltrated tubes was actually beneficial to the final composite product. A physical property that is demanded of the dense, fiber-reinforced ceramic composite tube is hermeticity, or prevention of gas leakage through the composite thickness. The SiC overcoat would actually help achieve this property by sealing both interior and exterior preform surfaces.



## **Preform Transport Properties**

This section discusses the pertinent density-dependent preform transport properties and their respective trends. These property trends are compared to those seen with a similar fiber-reinforced ceramic composite system (Starr and Hablutzel 1998). The preform properties that were not determined by experimental measurement were determined by a descriptive model, and are discussed for their validity in physical description.

### **Homogeneous Length Scale**

The 2 mm-thickness of the Nextel™ 312/SiC composite specimens used for experimental transport property measurement was a reasonable homogeneous length scale in the radial direction (perpendicular to fiber orientation), but not in the axial direction (parallel to fiber orientation). This specimen thickness corresponded to approximately three concentric fiber sleeves in the radial direction, making the assumption of composite homogeneity reasonable. However, the Nextel™ 312 fiber weave pattern is congruent to the axial direction, with a typical interstitial channel width between 1-3 mm. Therefore some channels may be wider than the specimen thickness. This explains the large pores observed in the composite specimens parallel to fiber orientation (Figure 3-7). The choice of the 2-mm thickness was used to satisfy use in the laser-flash thermal diffusivity measurement. The temperature change

of the rear specimen faces with greater thickness (>5 mm) may not have been detected.

### **Preform Permeability**

The Nextel™ 312/SiC composite permeabilities parallel to fiber orientation were higher than those measured perpendicular to fiber orientation due to the large observed specimen pores seen with the parallel specimens. The measured permeabilities of the Nextel™ 312/SiC composite specimens were approximately two orders of magnitude greater than the permeabilities of Nicalon™/SiC composite specimens reported by Starr and Hablutzel (1998). This was an artifact of the loose weave and the wide interstitial channels seen in the Nextel™ 312 braided tubular sleeve.

The permeability change with density was rather small initially for both fiber directions until the fiber bundles were densified (around 70% theoretical density). At this theoretical density, the permeability decreased significantly until the preform was essentially fully densified with SiC matrix. This permeability characteristic agreed with Nicalon™/SiC composite data reported by Starr and Hablutzel (1998).

### **Preform Thermal Conductivity**

The Nextel™ 312/SiC composite parallel thermal conductivities were higher than those measured perpendicular to fiber orientation. The composite thermal conductivity in both directions increased with an increase in theoretical

density due to the addition of the SiC matrix. The explanation for higher parallel thermal conductivity values is due to fewer interfaces between the fiber and matrix, which present a lower resistance to heat conduction.

Higher parallel composite thermal conductivities were also observed experimentally by laser-flash thermal diffusivity measurements for Nicalon™/SiC composites (Tawil et al. 1985). The Nextel™ 312/SiC composite parallel thermal conductivity at 80% theoretical density was approximately 7 W/m K at 1000°C with a Nextel™ 312 fiber thermal conductivity of 0.25 W/m K (3M Corporation). For comparison with results found by Tawil et al., the determined Nicalon™/SiC composite parallel thermal conductivity at 90% theoretical density was about 20 W/m K at 1000°C with a Nicalon™ fiber thermal conductivity of 3 W/m K. The difference in the two composite thermal conductivities was primarily due to differences in the specimen densities (amount of SiC matrix).

The preform thermal conductivity data used in GTCVI was made independent of temperature because the thermal conductivity change was minimal in the temperature range that the tube preform experienced during infiltration (1000-1200°C). Also, the removal of temperature dependence simplified the solution and convergence of the energy balance throughout the volume element array.

### **Preform Specific Surface Area**

The spherical node, cylindrical bond model (Starr 1995) used to characterize the preform specific surface area was a simple approach to the

description of the evolving, preform porous microstructure. Actual physical dimensions of the preform intrabundle porosity, channel area, and interlaminar porosity were approximated by the initial definitions of the node and bond radii (Table 5-1), while distributions in the node and bond radii and the bond length were added to simulate variation in the preform porosity.

The specific surface area function evaluated from Starr's node/bond model demonstrated a steep initial decrease with increase in density, unlike the specific surface area functions developed by Bhatia and Perlmutter (1980) and Currier (1990) where an initial increase in surface area was observed. Although, this initial increase in specific surface area may occur, the composite theoretical density at which the surface area maximum was observed was rather low (~40%). The neglect of this phenomenon would have minimal effect on the transient, long-term model prediction of the preform densification.

### **Preform Effective Diffusion Coefficient**

The effective diffusion coefficient function used in the model approximated the tortuosity of the evolving porous microstructure of the Nextel™ 312 preform. Although, the data used in the function were taken from Nicalon™/SiC specimens, the effective diffusion coefficient function trend was expected to be similar for the Nextel™ 312/SiC composite. Both composite systems had a bimodal, porous microstructure that included small pores that represented the intrabundle porosity and large pores that represented interstitial channel and interlaminar porosity. The actual value of the effective diffusion coefficient for the

Nextel™312/SiC composite may be somewhat higher than that for the Nicalon™/SiC composites due to the loose weave and wide interstitial channels seen with the Nextel™312 fiber weave.

### **Preform Emissivity**

A constant emissivity was assumed for the densifying Nextel™ 312 preform because the emissivities of the Nextel™ 312 fiber and the SiC matrix are similar (0.88 and 0.86 respectively), although the radiating surfaces became predominately SiC within a short period of infiltration time. Both tube interior and exterior surfaces were not smooth, but were rough in texture. Stray fibers in the tube preform and the ridges of the fiber bundles provided sites for SiC deposition, which made both tube surfaces characteristically rough. The roughness of the tube surfaces may have effected the local preform emissivity to some extent, however the amount of variation was uncertain.

### **Tube Density Characterization**

This section discusses the results of the density profiles determined by both X-ray computed tomography and digital image analysis. Their similarities, differences, and peculiar features are mentioned while their results are evaluated for their prediction of the transient density progression of the tube preform and the overall tube fiber volumes and theoretical densities at intermittent infiltration times.

## X-ray Computed Tomography

Theoretical density profiles provided by X-ray computed tomography indicated higher preform densities at the tube exterior and lower densities at both preform ends at early infiltration times. The dense preform thickness increased from the tube exterior to the interior as total infiltration time increased, agreeing with physical inspection of the tubes. At long infiltration times, the preform interior at the inlet end was shown to have the lowest density. The average tube theoretical densities taken from the X-ray computed tomography results were similar to the experimental tube theoretical densities, with the theoretical density values from the X-ray computed tomography slightly lower ( $\sim 2\text{--}7\%$ ).

Two outstanding artifacts from the theoretical density profiles produced by X-ray computed tomography appeared puzzling and needed some additional explanation. These artifacts involved the high X-ray attenuation that was seen at the SiC exterior overcoat and the fiber sleeve delamination seen at the tube preform interior.

The theoretical density profile of CVI 1218 (32 hours infiltration) showed a theoretical density gradient of approximately 20% at the tube mid-length with an even higher theoretical density gradient of about 40% at the preform inlet end. Density gradients of this magnitude were not apparent with physical inspection. The most likely explanation for this occurrence is the significant X-ray attenuation that was apparent at the tube exterior.

A thin SiC overcoat thickness of approximately  $250\text{ }\mu\text{m}$  was seen on the exterior. Pure SiC has a higher density ( $3.2\text{ g/cm}^3$ ) than the dense, Nextel™ 312

preform ( $\sim 2.5 \text{ g/cm}^3$ ), thus supporting higher X-ray attenuation. The X-rays that penetrated the composite tube thickness traveled through the SiC overcoat layer prior to encountering the preform material. The higher X-ray attenuation seen in this region resulted in X-ray beam hardening, thus lowering the energy of the penetrating X-ray flux. The lower energy of the X-ray flux affected the subsequent attenuation throughout the composite thickness.

Theoretical densities at the tube interior of CVI 1211 (6 hours infiltration) indicated by CT were less than the initial preform fiber volume (<35%). Some axial sections of the tube preforms experienced slight delamination of the interior Nextel™ 312 fiber sleeves (Appendix G). The thin gas space resulting from the delamination lowered the local tube theoretical density by the creation of a void, thus lowering the observed X-ray attenuation.

Another problem with the density analysis from X-ray computed tomography was the thickness non-uniformity in the tube preforms used. The preform fabrication technique used for these preforms was not optimized, with the composite thickness as high as 9 mm for some sections, much higher than the desired preform thickness (6.4 mm). The greater preform thickness supported additional X-ray beam hardening.

A qualitative description of the tube density progression was evident with the density results from X-ray computed tomography, indicating the density progression from the tube exterior to the interior. However, the SiC overcoat phenomenon and the sleeve delamination prevented realistic density prediction at the tube preform interior at the latter stages of infiltration.

## Digital Image Analysis

Tube density characterization by digital image analysis was performed only for tubes CVI 1217 and CVI 1218 (24 and 32 hours infiltration). Digital image analysis was not performed for the other two tubes because of severe specimen damage resulting from preparation and polishing of these low density-specimens. The inner Nextel™ 312 sleeves of the specimens from both CVI 1211 and CVI 1223 (6 and 12 hours infiltration) delaminated from the rest of the dense composite due to lack of SiC deposition.

The grayscale differentiation technique utilized in the digital image analysis enabled the evaluation of both preform fiber volume and theoretical density. Average tube preform fiber volumes and theoretical densities for both CVI 1217 (33% and 71% respectively) and CVI 1218 (33% and 83% respectively) from the digital image analysis agreed well with the overall density values from final composite mass and volume (Table 6-16). However, some data values for the fiber volume and theoretical density were somewhat lower than the average values (up to 20% lower). This is explained from the variation in the Nextel™312 fiber sleeve dimensions and the observed void in some of the digital images that did not physically exist in the composite specimen volume.

Each concentric Nextel™ 312 sleeve that was applied to a tube preform stretched to a slightly larger diameter, altering the unit dimensions of the Nextel 312 fiber weave. This phenomenon altered the fiber-bundle braiding angle, and also altered the dimensions of the porous channels. This caused some channels



from concentric fiber sleeves to directly stack vertically, leading to an above-average void phase percentage in the digital image.

Also, the digital images captured at the tube exterior contained void that did not physically exist in the composite volume. These non-associated voids were seen with the digital images captured at the tube exterior (Appendix H; Position 1). This void was included in the digital image analysis results making both fiber volumes and theoretical densities lower.

### **GTCVI Model Results and Validation**

This section discusses the results produced by GTCVI and their prediction of the experimental FCVI of tube preforms. Transient changes in tube preform temperature and density profiles are discussed as they relate to the degree of SiC densification. Local and transient temperature effects from gas convection and thermal conduction are mentioned. The effects of the variation of temperature, total flow rate, and hydrogen/MTS molar feed ratio on densification rates and total infiltration time are considered.

The specific, model parameter adjustment that yielded the best agreement with experimental tube average densities is discussed while the model was used to determine a process parameter set that yielded the lowest process time while achieving an acceptable tube density. The lowest process time produced by GTCVI is then compared with the infiltration times realized with the experimental tube infiltrations that utilized higher process temperature and total flow.

## Model Results

The preform temperature profiles at the start and end of infiltration (28 hours) basically reflected the parabolic coating chamber temperature profile that was placed as a boundary condition (Figures 7-7 and 7-8). The initial higher radial temperature difference seen at the gas inlet was indicative of convective cooling from the gas mixture (Figure 7-9). A plot of the initial gas flow pattern confirmed the strong gas convection in this region (Figure 7-21). The higher radial temperature difference observed at the preform outlet end at the end of infiltration (28 hours) was due to higher gas flow in this region, resulting from lower density and higher permeability. Again, the gas flow profile at this time confirms this (Figure 7-22). The lower temperature region seen near the gas inlet at 28 hours was still influenced from convective cooling of the gas mixture (Figure 7-8). The degree of convective gas cooling was also noticed in the transient average radial temperature difference curves (Figure 7-10), where higher total flow yielded a higher temperature difference.

The transient average radial deposition rate curves demonstrated higher rates at the tube exterior initially (Figure 7-17) with the deposition rate maximum translating from the tube exterior to the interior. This agreed with the physical observation and the X-ray computed tomography density results. Higher deposition rates were seen at the interior near the end of infiltration because of the higher available surface area. However, the absolute specific surface area available in this region at this time was much lower, making the SiC deposition rate much lower.

The tube theoretical density profiles reflected the preform temperature profiles, with higher theoretical densities seen at the tube exterior and lower theoretical densities seen at the tube interior and both preform ends arising from lower temperature in these regions. The preform region near the gas inlet experienced the fastest SiC densification rate, for this region experienced the highest reactant concentration during infiltration because of the dominant gas convection. The density profiles at longer infiltration times showed similar trends.

Transient average tube theoretical density results demonstrated that an increase in either infiltration temperature or MTS concentration (lower hydrogen/MTS molar feed ratio,  $\alpha$ ) enhanced the tube densification rate and reduced the total infiltration time required for complete densification. The increase in total flow showed the same trend except with high total flow (30 slm). With the high flow, the convective gas cooling increased the initial radial temperature difference. The tube preform region near the gas inlet experienced high densification rates, however both preform ends experienced slower densification rates due to significant gas convection and attributed heat loss, which forced lower temperatures in these regions.

The GTCVI transient simulations were performed with two distinct SiC deposition parameter sets (Besmann and Chiang, Table 7-8). Excellent model agreement with the average tube densities was achieved with the Besmann deposition parameters (Besmann 1991), and the Chiang parameters (1999) greatly underpredicted the tube densities at longer infiltration times despite a surface area module with a high initial value ( $1500 \text{ cm}^{-1}$ ). This suggested that

the SiC deposition parameters utilized in the model depended on reactor and experimental conditions from which the SiC growth rate data was taken. Although, the methods used by Chiang to determine the SiC deposition parameters had significant merit, the reactor configuration that he used was different (cold-wall) than the configuration used in this research (hot-wall). However, it was believed that the simplicity of the momentum definition used in the GTCVI model also made the density results with the Chiang parameters much worse, and the higher HCl inhibition led to significantly lower SiC deposition rates (an order of magnitude) throughout the model simulation.

## **Model Validation**

The transient simulation of the tube infiltration was modeled with GTCVI using three different specific surface area modules, with their only difference lying in the initial value. The transient average tube theoretical density profiles using all three surface area functions had similar shape (Figure 7-11). The transient model density profile with the use of the  $300\text{ cm}^{-1}$  initial specific surface area value produced the best agreement with the overall experimental tube densities at all intermittent times. Therefore, this specific surface area module was chosen for subsequent simulation and was used to determine the lowest total process time by the variation of process temperature and total flow.

The initial specific surface area value of  $300\text{ cm}^{-1}$  was significantly lower than  $1500\text{ cm}^{-1}$ ; the associated value if no initial fiber contact was assumed. However, it is noted that the initial value is inversely proportional to the effective

fiber radius. Initial fiber contact would lower the available initial surface area, resulting in a larger effective fiber radius. The fiber contact that physically existed in the fiber bundles was seen in Figure 3-1(b), caused by the tight fiber packing in the bundles and the compression of adjacent fiber sleeves. Therefore, this lower, initial value of the specific surface area was not unrealistic.

The variation of the process temperature and total flow in the GTCVI model simulation resulted in the lowest process time of 15.9 hours (1244°C mid-line temperature, 18 slm total flow, and a hydrogen/MTS ratio of 4.98). The average tube theoretical density achieved with the lowest time was 80%. The shortest process time that was seen in experiment was 16 hours with the use of a 1242°C mid-line temperature, 9 slm total flow, and a hydrogen/MTS ratio of 4.94. These total process times were in excellent agreement, however, the total flow predicted by the model was much higher. The model disagreement with the total flow was due to the simplification of momentum defined in the open gas space.

Another issue of disagreement between the GTCVI results and the experimental results involved the prediction of the axial preform region that experienced the fastest densification rate. The X-ray computed tomography density profiles showed that the preform mid-length experienced the fastest densification rate, while the GTCVI model density profiles predicted the tube section near the gas inlet. The GTCVI simulation predicted lower tube densities at both preform ends at the end of infiltration (32 hours), while the density profile from X-ray computed tomography at this time showed lower densities only at the

preform inlet end. Again, the discrepancy in the density results for both GTCVI and X-ray computed tomography was probably due to the simplification of the momentum definition in the open gas space-volume elements.

In the model, Darcy's law was defined in the gas spaces as well as in the preform. Darcy's law is applicable to porous media, but not so in open gas space. The model assumes a permeability of 100 Darcies ( $10^{-6} \text{ cm}^2$ ) for the open gas space. Initially, the preform perpendicular and parallel permeabilities were approximately 500 Darcies and 800 Darcies respectively, making the convective resistance lower in the preform than in the open gas space, which is obviously unrealistic. This simplified, momentum definition in the open gas space in the model explains the dominant gas flow pattern observed at the start of infiltration, the dominant densification rates seen near the gas inlet, and the low densification rates seen at both preform ends.

Although the model did not agree with experiment on particular issues, it successfully demonstrated the transient density progression in a semi-quantitative sense while predicting lower infiltration times with the increase in both temperature and total flow. The GTCVI model results also provided excellent agreement with the average tube theoretical densities at all four intermediate infiltration times with reasonable adjustment of the specific surface area function.

## CHAPTER 9

### SUMMARY AND CONCLUSIONS

The fabrication of dense, fiber-reinforced ceramic composite tubes using the forced-flow, chemical vapor infiltration process was successful, but labor-intensive. An experimental method was implemented to fabricate fibrous tube preforms 5 cm in ID, 6.5 mm in thickness, and 30 cm in length using collapsible braided tubular sleeves of Nextel™312 fiber and a binding phenolic resin. The tube preforms underwent a unique preform fixturing for furnace assembly that established the forced flow and temperature gradient across the preform thickness. The FCVI apparatus consisted of a furnace that utilized resistive heating to achieve adequate infiltration temperature. Silicon carbide (SiC) was deposited throughout the fibrous preform with the use of methyltrichlorosilane (MTS) and hydrogen diluent.

A tube theoretical density of 80% with approximately 35% initial fiber volume was achieved in 32 hours of infiltration using a coating chamber mid-line temperature of 1197°C, a total flow of 6 slm, and a hydrogen/MTS molar feed ratio,  $\alpha$ , of 5. Tube preforms infiltrated with similar process conditions for 6, 12, and 24 hours achieved final theoretical densities of 40%, 54%, and 70% respectively. These overall average tube theoretical densities were determined from final masses of the fiber, composite, and the composite tube volume. The

postinfiltration composite tube volume increased somewhat due to the change in dimension influenced by the apparent SiC deposit on the tube interior and exterior.

An increase in infiltration temperature (1246°C), with all other process parameters constant, reduced the total infiltration time from 32 hours to 27 hours achieving a 90% tube theoretical density. An increase in infiltration temperature (1242°C) and an increase in total flow (9 slm) decreased the total infiltration time to 16 hours achieving an 88% theoretical density. The final theoretical densities for these tubes were somewhat higher than 80% due to the unaccounted SiC deposited on the tube interior wall.

The transient density progression in the tube preforms with the FCVI process was investigated by characterizing the tube density profiles for the composite tubes infiltrated with the same process conditions for various time lengths. The tube densities were characterized using an X-ray computed tomographic technique and a digital image analysis technique, while both techniques were calibrated with suitable standards prior to tube density characterization.

The density profiles produced from the X-ray computed tomography qualitatively demonstrated the tube density progression from the tube exterior to the tube interior. However, significant radial density gradients (up to 40%) appeared with the tube preform infiltrated for 32 hours (CVI 1218). This phenomenon was attributed to significant X-ray attenuation at the SiC overcoat seen at the tube exterior. The high X-ray attenuation in this SiC overcoat region



lowered the X-ray energy flux affecting the subsequent X-ray attenuation through the composite thickness. Despite this overcoat phenomenon, the average tube theoretical densities from X-ray computed tomography (37%, 52%, 66%, and 73% for 6, 12, 24, 32 hours infiltration respectively) were in good agreement with the overall average tube densities determined from final composite mass and volume, although the tube densities determined by the X-ray computed tomography were slightly lower.

Unlike the density profiles determined from X-ray computed tomography, the transient tube density progression was not seen with digital image analysis. The specimen preparation severely damaged the specimens taken from the composite tubes infiltrated for short times (six and 12 hours). These specimens were destroyed due to delamination of the inner preform Nextel™312 fiber sleeves caused by lack of SiC deposition.

The grayscale ambiguity in the captured digital images seen with the fiber bundle damage and the epoxy-filled voids was corrected by digital retouching with suitable grayscales representative of the respective material phases. The average fiber volume and the theoretical density for tube CVI 1217 (24 hours) were 33% and 71%, respectively while the average fiber volume and theoretical density for tube CVI 1218 (32 hours) were 33% and 83%, respectively. The majority of the tube theoretical density profile throughout CVI 1217 was between 70-80%, while the majority of the tube theoretical density profile throughout CVI 1218 was between 80-90%. A few data outliers were observed with these two tubes, with fiber volumes and theoretical densities as much as 20% lower than

the tube average. This was caused by the variation in the fiber weave and the inclusion of void space in the digital image that did not physically exist in the composite volume. Despite these discrepancies, the average tube fiber volumes and theoretical densities provided by digital image analysis were in excellent agreement with the overall average density values.

Pertinent transport properties of the densifying tube preform were evaluated with either experimental techniques or with the use of a characteristic model. These transport properties were then input to the FCVI process model, GTCVI, in efforts to effectively simulate the transient tube densification.

The preform thermal conductivities were higher parallel to fiber orientation, due to fewer interfaces between the fiber and matrix, while the thermal conductivities increased with an increase in theoretical density ( $\sim 7$  W/m K at 80% theoretical density). Preform permeabilities were slightly higher parallel to the fiber orientation, due to the large specimens pores resulting from the large channels seen in the fiber weave, while overall initial permeabilities were approximately two orders of magnitude greater ( $\sim 1000$  Darcies) than those found with a similar fiber-reinforced ceramic composite.

Other preform transport properties that were input into GTCVI were reasonable approximations of the densifying tube preform. The specific surface area function developed from a spherical node/cylindrical bond model was a reasonable description of the bimodal porosity of a fibrous preform, which consists of small intrabundle pores and large channels and interlaminar porosity. The effective diffusion coefficient function, although taken from a similar fiber-

reinforced ceramic composite, also demonstrated a bimodal relationship representing the interbundle porosity and the channel and interlaminar porosity. The preform emissivity was assumed constant, taken from the averages of both Nextel™312 fiber and SiC matrix. Even though the emissivity values for both were similar (0.86 and 0.88 respectively), the radiating surfaces were predominantly SiC for the majority of the infiltration.

Analysis of the CVI fundamentals with the use of a simple, one-dimensional model enabled the investigation of key infiltration parameters and their corresponding effects on the reaction rate throughout the preform thickness. Isothermal infiltration with a low total molar flux resulted in preferential reaction at the preform interior. Preform infiltration with a higher simulated MTS depletion improved reaction uniformity, but lowered the absolute reaction rate. Infiltration with both a temperature gradient and a higher total molar flow favored higher initial reaction rates at the preform exterior. A transient simulation with a suitable temperature gradient and total molar flux demonstrated the achievement of a uniform density, favoring SiC deposition to advance from the preform exterior (higher temperature) to the interior (lower temperature).

These favorable infiltration conditions were used in GTCVI, a comprehensive, finite volume element model specifically developed for the simulation of FCVI processes. The results produced by GTCVI demonstrated the transient tube densification with two-dimensional temperature and density profiles provided at many specified intervals. Transient and axial radial preform temperature difference plots demonstrated gas convection effects on preform

densification. The preform regions that experienced the highest degree of gas convection initially and at the end of infiltration were visualized with gas flow plots. The variation of infiltration parameters in the GTCVI simulation displayed effects on tube densification rate and total infiltration time. The results obtained from GTCVI were made to agree with the experimental average tube densities at intermediate times by suitable adjustment of the initial specific surface area.

The temperature profiles of the tube preform reflected the coating chamber temperature profile with higher temperatures seen at the tube mid-length and lower temperatures seen at both ends. The highest radial temperature difference occurred near the gas inlet initially due to significant gas convective cooling. The average radial temperature difference increased with an increase in flow rate, also indicating gas convection effects. As the tube infiltration progressed, the average radial temperature difference decreased due to the addition of SiC matrix, which increased the thermal conductivity of the tube preform. At the end of infiltration, the highest radial temperature difference was seen at the preform outlet end, which resulted from significant gas flow due to lower density and higher permeability. Gas flow vector plots produced by GTCVI confirmed the significant gas convection seen at the gas inlet at the start of infiltration and at the preform outlet end at the end of infiltration.

The tube density profiles produced by GTCVI resembled the tube temperature profiles with the tube preform region near the gas inlet experiencing the fastest densification rate. Inspection of the tube density profiles at various times demonstrated the transient tube densification from the tube exterior to the

tube interior with lower densities observed at both tube preform ends. At longer infiltration times, the tube density profiles produced by GTCVI were qualitatively the same, but at higher theoretical densities.

Variation of the process temperature, total flow rate, and hydrogen/MTS molar feed ratio was performed to determine their effects on the tube densification rate and total infiltration time. Increase in temperature and a decrease in hydrogen/MTS molar feed ratio enhanced the tube densification rate and reduced total infiltration time. A minimum in the total infiltration time was seen with the variation in total flow rate. At very high total flow rates (~30 slm), the densification rate was higher near the gas inlet, but both preform ends experienced lower SiC deposition rates due to lower temperature resulting in longer total infiltration time.

The GTCVI model results were made to agree with the overall experimental average tube densities at intermediate times by variation of the specific surface area module used in the simulation. Three different specific surface area modules were used with their only difference lying in the initial value. The model results with all three specific surface area functions produced the same transient relationship as the overall average tube densities. However, the best agreement with the overall average tube densities was achieved with the specific surface area module with an initial value of  $300 \text{ cm}^{-1}$ .

This initial specific surface area value was much less than the estimated initial specific surface area value that assumed no initial fiber contact ( $1500 \text{ cm}^{-1}$ ). The lower initial specific surface area value was justified by the observed tight

fiber packing of the Nextel™312 fibers and the compression of concentric Nextel™312 fiber sleeves which led to some fiber contact. The apparent fiber contact was evident in the captured digital images, where the contiguous fibers in a given bundle were closely packed and poorly infiltrated with SiC matrix.

The tube density profiles produced by GTCVI were in semi-quantitative agreement with the density profiles produced X-ray computed tomography. The density profiles from both depicted the tube density progression from the tube exterior to the tube interior. However, the initial tube densification was favored near the gas inlet in the GTCVI results, and was favored about mid-length in the X-ray computed tomography results.

At the early stages of infiltration (6 and 12 hours), the GTCVI density profiles and the X-ray computed tomography density profiles agreed somewhat in that higher densities were seen at the tube exterior and lower densities were seen at both preform ends. However, at the latter stages of infiltration, the GTCVI density profiles showed the majority of the tube length at high theoretical density (75-85%) with lower densities seen at both preform ends (65%). The X-ray computed tomography density profiles showed a radial density gradient through the preform thickness with the lowest densities (~40%) seen only at the preform inlet end, which was unrealistic. Despite their depicted differences, the average tube densities and density profiles produced by GTCVI were in reasonable agreement with those produced by X-ray computed tomography.

The most favorable infiltration conditions produced by GTCVI were 1246°C, 18 slm total flow, and a  $\alpha$ -value of 4.98, yielding an 80% tube theoretical

density in 15.9 hours. This predicted total infiltration time agreed with the experimental tube infiltration with use of higher temperature and total flow (16 hours with 1242°C and 18 slm). The only discrepancy between the conditions used in experiment and the conditions predicted by GTCVI was in the total flow rate. The primary reason for the discrepancy between the model and the experimental infiltrations was attributed to the simplification of momentum defined in the volume elements of the open gas space in GTCVI.

In the GTCVI source code, Darcy's Law was used to define momentum in the permeable preform and in the open gas space. Darcy's law, which applies to flow through porous media, does not apply to open gas space. The model designated a permeability of 100 Darcies ( $10^{-6} \text{ cm}^2$ ) to the volume elements of the open gas space. The measured preform permeabilities at initial preform theoretical density were approximately 1000 Darcies ( $10^{-5} \text{ cm}^2$ ). This defined a higher resistance in the open gas space elements, which was obviously unrealistic. This artifact explains the dominant initial gas flow pattern at the gas inlet, the preferred tube densification in the tube preform region near the gas inlet, and the lower densities seen at both preform ends.

Despite the use of a simplified momentum for the open gas space, GTCVI was successful in the semi-quantitative prediction of the transient tube density progression, and was successful in the prediction of densification effects and total infiltration times with variation of the FCVI process parameters. With the adjustment of the initial specific surface area, the GTCVI prediction of the overall average tube densities at intermediate times was excellent.

## CHAPTER 10 FUTURE WORK

The fabrication of fiber-reinforced ceramic composite tubes using the FCVI process was successful at the developmental stage. However, consideration must be taken in the FCVI process scale-up for fossil energy applications. Several issues that need addressing include furnace scale-up and preform fabrication, improvement in ceramic composite performance, improvement in the predictive FCVI process model, and development of a workable, heat exchanger design.

### **Scale-Up Considerations**

The proposed ID and thickness of the fiber-reinforced ceramic composite tubes are the same (5 cm and 6.4 mm respectively). However, the Department of Energy wishes to implement tubes 120 cm in length. A suitable FCVI furnace that can accommodate a uniform axial-temperature zone length of 120 cm is necessary. The experimental FCVI furnace used in this research experienced significant heat loss at both ends. Ample furnace shell insulation would be required to reduce heat loss in the scale-up FCVI furnace.



The utilization of furnace heating with graphite resistance would make the most sense, for it can sufficiently heat a large volume with suitable power (high amperage, low voltage). Furnace heating using radio frequency-induction would not be a good choice for the scale-up. A long, inductive coil with a large radius would be necessary, and its use would most likely lead to thermal runaway in the preform caused by favored matrix deposition at certain locations (Midha 1997).

The use of a higher total flow is needed due to the increase in the preform cross-sectional area. The four-fold increase in preform cross-sectional area requires a four-fold increase in the total flow rate to achieve the same total molar flux used in this developmental research. If the flow is introduced to the tube preform at one position, localized high preform temperature gradients may occur (gas convection), and the uniform distribution of MTS precursor may be disrupted along the length of the tube interior. Therefore, a system of multiple gas injectors, with the outlets at equidistant locations, should be used to uniformly distribute the precursor and to eliminate gas convective cooling.

The associated costs with the furnace, required power delivery, materials, and labor and maintenance are high. To justify the capital investment, a FCVI furnace should accommodate a multiple tube-fixturing in order to reduce the total cost per composite part (Roman 1995). However, each tube would have its own cooling line and multiple gas injector system, thus making the tube preform fixturing cumbersome.

The preform compression used in this research was tedious, but effective. New techniques may be employed that can compress multiple resin

impregnated-tube preforms with relative ease. This would reduce labor cost associated with the preform fabrication step.

### Composite Performance

A critical issue for the ceramic composite is its associated strengths in the principle modes of loading (tension and torsion) at high temperature (1100°C). The room-temperature tensile strength for the composite tubes fabricated in this research is approximately 150 MPa (Carter 2000). The proper choice of the fiber type and fiber weave can be made to meet specific loading requirements. Suggested fiber types include Nextel™ 610 (3M Corporation, Saint Paul, MN), which is >99%  $\text{Al}_2\text{O}_3$ , and Hi-Nicalon™ (Nippon Corporation, Tokyo, Japan), which is predominantly SiC with little oxygen content.

The most important mechanical property of the fiber-reinforced ceramic composite is the fracture toughness (Lowden 1987). The composite fracture toughness can be significantly enhanced with the application of a uniform interface thickness, which is compliant with both fiber and matrix and stable in oxidizing environments at high temperature. Currently, the most attractive interface that has potential for ceramic composite application is BN (Griffiths and Nilson 1998). The most likely method for the interface application would be chemical vapor deposition at low temperature (~900°C) and pressure (<1 kPa). The total time may be excessive (~1000 hours), however, the interface may be applied to multiple tube preforms simultaneously.

## Process Model Improvement

The area that needs the most improvement in the FCVI process model is the definition of fluid momentum for the gas phase. Darcy's law (Darcy 1856), which is suitable for potential flow in porous media, is not suitable for description of fluid flow in open space. A more, complete treatment of fluid momentum, including inertial effects and viscous effects, is necessary. The incorporation of multicomponent mass transport effects in the species balances would make the model more realistic in describing the existing FCVI phenomena.

The FCVI process could be modeled with a three-dimensional, finite element (FEM) package, which can solve robust conservation balances over many different domain discretizations (meshing). A difficult issue that stands with the use of an appropriate FEM package is the applied boundary conditions in the circumferential direction ( $\theta$ -direction) because the actual associated temperature and species boundary conditions are uncertain in this direction. Finite element analysis with adiabatic and constant boundary conditions shall be done for the comparison of results.

The most useful application of the FEM package would be the investigation of different multiple-tube arrangements. The FEM package could reveal a particular tube arrangement that would yield the most uniform temperature profiles for all tubes in the arrangement. In a given multiple-tube arrangement, a particular tube is heated by radiation emanating from the coating

chamber and from contiguous tubes in the arrangement. The optimal tube arrangement found with the FCVI furnace would support densification that would yield high, uniform density for all of the tubes in the arrangement.

### **Heat Exchanger Design**

An optimal tube arrangement in the heat exchanger must be found that minimizes the number of fiber-reinforced ceramic composite tubes required for the design. It is noted that only the use of heat exchanger passes made of fiber-reinforced ceramic composite would be quite expensive and impractical. If the ceramic composite is utilized for the tube passes near the inlet of the combustor flue and for the tube passes near the outlet of the clean air, where the temperatures are highest (1100°C), the remaining tube passes may be constructed with the current traditional materials (metal alloys, aluminides).

A critical issue that lies with the heat exchanger design is the ceramic composite joining with metals and alloys. The joining must maintain adequate strength in corrosive environments at high temperature (Iwamoto 1991). Current joining methods that are being investigated include mechanical joining, brazing, and solid-phase joining. The necessary requirement for these joining methods is the limitation of species diffusion at the ceramic/metal interface, which can significantly reduce the joining strength over long periods of time.

## APPENDIX A GTCVI MODEL INPUT FILE

This appendix displays the model input file used in GTCVI. The contents of the input file include the parameter convergence criteria, direction sweep of equation solution, number and dimensions of the volume elements in the domain configuration, element material definitions, boundary conditions, material filenames, gas filenames, and lengths of the time intervals.

### GTCVI Model Input File

**[Coordinate Definition]**

rZ .

**[Cylindrical Off-set (cm)]**

54610

**[Maximum Number of Iteration Per Time Step]**

80

**[Parameter Convergence Criteria]**

02,1.0D-4,0.5 temperature

02,1.0D-6,1.0 pressure

02,1.0D-3,1.0 MTS concentration

02,1.0D-2,0.5 HCl concentration

**[Parameter Solution Direction]**

100000

**[Number of radial volume elements]**

35









**[Boundary Conditions]**

{Radial Element Number,  $\theta$ -Element Number, Axial Element Number, Adiabatic/Fixed Toggle, Temperature, Pressure, MTS Mole Fraction, HCl Mole Fraction}

```

99,01,99,'A',0.0,'A',0.0,'A',0.0,'A',0.0
99,03,99,'A',0.0,'A',0.0,'A',0.0,'A',0.0
99,99,01,'F',200.0,'A',0.0,'A',0.0,'A',0.0
99,99,49,'F',200.0,'A',0.0,'A',0.0,'A',0.0
30,02,49,'F',200.0,'F',100.0,'A',0.0,'A',0.0
31,02,49,'F',200.0,'F',100.0,'A',0.0,'A',0.0
32,02,49,'F',200.0,'F',100.0,'A',0.0,'A',0.0
33,02,49,'F',200.0,'F',100.0,'A',0.0,'A',0.0
35,99,01,'F',890.0,'A',0.0,'A',0.0,'A',0.0
35,99,02,'F',914.5,'A',0.0,'A',0.0,'A',0.0
35,99,03,'F',937.9,'A',0.0,'A',0.0,'A',0.0
35,99,04,'F',960.4,'A',0.0,'A',0.0,'A',0.0
35,99,05,'F',981.8,'A',0.0,'A',0.0,'A',0.0
35,99,06,'F',1002.2,'A',0.0,'A',0.0,'A',0.0
35,99,07,'F',1021.6,'A',0.0,'A',0.0,'A',0.0
35,99,08,'F',1040.0,'A',0.0,'A',0.0,'A',0.0
35,99,09,'F',1057.3,'A',0.0,'A',0.0,'A',0.0
35,99,10,'F',1073.7,'A',0.0,'A',0.0,'A',0.0
35,99,11,'F',1089.0,'A',0.0,'A',0.0,'A',0.0
35,99,12,'F',1103.3,'A',0.0,'A',0.0,'A',0.0
35,99,13,'F',1116.6,'A',0.0,'A',0.0,'A',0.0
35,99,14,'F',1128.9,'A',0.0,'A',0.0,'A',0.0
35,99,15,'F',1140.2,'A',0.0,'A',0.0,'A',0.0
35,99,16,'F',1150.4,'A',0.0,'A',0.0,'A',0.0
35,99,17,'F',1159.7,'A',0.0,'A',0.0,'A',0.0
35,99,18,'F',1167.9,'A',0.0,'A',0.0,'A',0.0
35,99,19,'F',1175.1,'A',0.0,'A',0.0,'A',0.0
35,99,20,'F',1181.3,'A',0.0,'A',0.0,'A',0.0
35,99,21,'F',1186.5,'A',0.0,'A',0.0,'A',0.0
35,99,22,'F',1190.6,'A',0.0,'A',0.0,'A',0.0
35,99,23,'F',1193.8,'A',0.0,'A',0.0,'A',0.0
35,99,24,'F',1195.9,'A',0.0,'A',0.0,'A',0.0
35,99,25,'F',1197.0,'A',0.0,'A',0.0,'A',0.0
35,99,26,'F',1197.1,'A',0.0,'A',0.0,'A',0.0
35,99,27,'F',1196.2,'A',0.0,'A',0.0,'A',0.0
35,99,28,'F',1194.3,'A',0.0,'A',0.0,'A',0.0
35,99,29,'F',1191.3,'A',0.0,'A',0.0,'A',0.0
35,99,30,'F',1187.4,'A',0.0,'A',0.0,'A',0.0
35,99,31,'F',1182.4,'A',0.0,'A',0.0,'A',0.0
35,99,32,'F',1176.4,'A',0.0,'A',0.0,'A',0.0
35,99,33,'F',1169.4,'A',0.0,'A',0.0,'A',0.0
35,99,34,'F',1161.4,'A',0.0,'A',0.0,'A',0.0
35,99,35,'F',1152.3,'A',0.0,'A',0.0,'A',0.0
35,99,36,'F',1142.3,'A',0.0,'A',0.0,'A',0.0
35,99,37,'F',1131.2,'A',0.0,'A',0.0,'A',0.0
35,99,38,'F',1119.1,'A',0.0,'A',0.0,'A',0.0

```

```

35,99,39,'F',1106.0,'A',0.0,'A',0.0,'A',0.0
35,99,40,'F',1091.9,'A',0.0,'A',0.0,'A',0.0
35,99,41,'F',1076.8,'A',0.0,'A',0.0,'A',0.0
35,99,42,'F',1060.6,'A',0.0,'A',0.0,'A',0.0
35,99,43,'F',1043.5,'A',0.0,'A',0.0,'A',0.0
35,99,44,'F',1025.3,'A',0.0,'A',0.0,'A',0.0
35,99,45,'F',1006.1,'A',0.0,'A',0.0,'A',0.0
35,99,46,'F',985.9,'A',0.0,'A',0.0,'A',0.0
35,99,47,'F',964.7,'A',0.0,'A',0.0,'A',0.0
35,99,48,'F',942.4,'A',0.0,'A',0.0,'A',0.0
35,99,49,'F',919.2,'A',0.0,'A',0.0,'A',0.0
01,99,99,'F',50.0,'A',0.0,'A',0.0,'A',0.0
04,02,01,'F',90.0,'A',0.0016325,'F',0.16722,'F',0.0
0,0,0,'A',0.0,'A',0.0,'A',0.0,'A',0.0

```

**[Gas Filename]**

'PolarMix.GAS'

**[Activation of Radiation Algorithm]**

radiation

**[Initial Parameter Guess-values]**

{Temperature, Pressure, MTS Mole Fraction, HCl Mole Fraction}

500.0,101.0,0.1,0.00

**[Number of Time Steps]**

27

**[Time Step Intervals (Hours)]**

0.5,0.5,0.5,0.5,0.5,0.5,0.5

1.,1.,1.,1.,1.,1.,1

2.,2.,2.,2.,2.,2.,2

2.,2.,2.,2.,2.,2.,2

## APPENDIX B

### GTCVI TUBE PREFORM MATERIAL FILE

This appendix presents the material file containing the pertinent transport properties of the densifying tube preform. The preform transport properties include the thermal conductivity, permeability, effective diffusion coefficient, specific surface area, and emissivity. The initial preform fiber volume is specified at the beginning of the file to queue the initial tube preform transport properties. The constants for the thermal conductivity for both fiber orientations (Equation 5-22) are provided while the permeability, specific surface area, and effective diffusion coefficient data are listed in tabular form. A constant emissivity is input at the end of the tube preform material file.

#### GTCVI Tube Preform Material File

##### [Material Identification]

NxTriBr7 Nextel 7ppi triaxial braid 8Aug97

##### [Initial Preform Fiber Volume]

3.44200D-01  
.FALSE.

##### [Thermal Conductivity]

.FALSE.

{c in r-coordinate, c in  $\theta$ -coordinate}

{a,b in r-coordinate, a,b in  $\theta$ -coordinate, a,b in z-coordinate}

0.00000D+00 0.00000D+00 0.00000D+00  
-1.41190D+02 1.42857D+02 -1.87500D+01 2.00000D+01 -1.87500D+01 2.00000D+01





```
8.99313E-01 0.00000E+00 0.00000E+00 0.00000E+00
1.00000E+00 0.00000E+00 0.00000E+00 0.00000E+00
```

### [Specific Surface Area]

```
.TRUE.
```

```
{Number of data entries}
```

```
{Normalized theoretical density, r-coordinate,  $\theta$ -coordinate, z-coordinate}
```

```
44
```

```
0.00000E+00 1.47684E+03 1.47684E+03 1.47684E+03
4.00465E-01 1.47684E+03 1.47684E+03 1.47684E+03
4.81228E-01 1.27860E+03 1.27860E+03 1.27860E+03
5.50709E-01 1.00479E+03 1.00479E+03 1.00479E+03
6.04255E-01 7.00130E+02 7.00130E+02 7.00130E+02
6.41544E-01 4.61185E+02 4.61185E+02 4.61185E+02
6.65744E-01 2.83551E+02 2.83551E+02 2.83551E+02
6.80758E-01 1.64667E+02 1.64667E+02 1.64667E+02
6.89802E-01 1.06094E+02 1.06094E+02 1.06094E+02
6.95041E-01 7.00799E+01 7.00799E+01 7.00799E+01
6.98623E-01 4.40112E+01 4.40112E+01 4.40112E+01
7.01040E-01 3.57690E+01 3.57690E+01 3.57690E+01
7.02878E-01 2.73865E+01 2.73865E+01 2.73865E+01
7.04387E-01 2.50382E+01 2.50382E+01 2.50382E+01
7.05746E-01 2.19447E+01 2.19447E+01 2.19447E+01
7.06963E-01 2.14099E+01 2.14099E+01 2.14099E+01
7.09304E-01 2.00777E+01 2.00777E+01 2.00777E+01
7.10426E-01 1.99444E+01 1.99444E+01 1.99444E+01
7.11545E-01 1.98032E+01 1.98032E+01 1.98032E+01
7.12658E-01 1.96474E+01 1.96474E+01 1.96474E+01
7.13765E-01 1.94893E+01 1.94893E+01 1.94893E+01
7.43473E-01 1.62804E+01 1.62804E+01 1.62804E+01
7.70630E-01 1.46871E+01 1.46871E+01 1.46871E+01
7.95249E-01 1.30850E+01 1.30850E+01 1.30850E+01
8.17342E-01 1.13893E+01 1.13893E+01 1.13893E+01
8.36921E-01 9.46343E+00 9.46343E+00 9.46343E+00
8.54002E-01 7.30062E+00 7.30062E+00 5.09599E+00
8.80877E-01 3.05533E+00 3.05533E+00 3.05533E+00
8.90994E-01 7.26589E-01 7.26589E-01 7.26589E-01
8.99313E-01 0.00000E+00 0.00000E+00 0.00000E+00
8.99313E-01 0.00000E+00 0.00000E+00 0.00000E+00
8.99313E-01 0.00000E+00 0.00000E+00 0.00000E+00
8.99313E-01 0.00000E+00 0.00000E+00 0.00000E+00
8.99313E-01 0.00000E+00 0.00000E+00 0.00000E+00
8.99313E-01 0.00000E+00 0.00000E+00 0.00000E+00
8.99313E-01 0.00000E+00 0.00000E+00 0.00000E+00
8.99313E-01 0.00000E+00 0.00000E+00 0.00000E+00
8.99313E-01 0.00000E+00 0.00000E+00 0.00000E+00
8.99313E-01 0.00000E+00 0.00000E+00 0.00000E+00
8.99313E-01 0.00000E+00 0.00000E+00 0.00000E+00
8.99313E-01 0.00000E+00 0.00000E+00 0.00000E+00
8.99313E-01 0.00000E+00 0.00000E+00 0.00000E+00
8.99313E-01 0.00000E+00 0.00000E+00 0.00000E+00
8.99313E-01 0.00000E+00 0.00000E+00 0.00000E+00
1.00000E+00 0.00000E+00 0.00000E+00 0.00000E+00
```

**[Emissivity]**

.FALSE.

{r-coordinate,  $\theta$ -coordinate, z-coordinate}

8.70000D-01 0.00000D+00 8.70000D-01 0.00000D+00 8.70000D-01 0.00000D+00

## APPENDIX C GTCVI GAS FILE

This appendix contains the gas input file input to the GTCVI model. The contents of the gas file include the parameters for the quaternary gas mixture viscosity, heat capacity, thermal conductivity, and mixture molecular diffusivities for CH<sub>4</sub> and HCl. It is noted that the CH<sub>4</sub> mixture diffusivity represents the MTS species in the GTCVI simulation because of its limitation of the SiC deposition rate (Allendorf et al. 1994). The parameters for the SiC surface deposition rate are listed along with the stoichiometric coefficient (Equation 4-3) and the density of the SiC matrix.

### GTCVI Gas File

#### [Thermal Conductivity]

$$[\lambda = a + b \cdot T + c \cdot T^{**2} + d \cdot T^{** -2}]$$

{a, b, c, d, units}'

'EQUATION'

7.449459D-04 1.714231D-06 -1.634002D-10 0.0D0 [W/cm K]

#### [Heat Capacity]

$$[C_p = a + b \cdot T + c \cdot T^{**2} + d \cdot T^{** -2}]$$

{a, b, c, d, units}'

'EQUATION'

5.9558368D+01 3.0085D-02 -1.072989D-05 0.0D0 [J/mol K]



**[Viscosity]**

$$[\mu = a + b \cdot T + c \cdot T^{**2} + d \cdot T^{**-2}]$$

{a, b, c, d, units}

'EQUATION'

1.275965D-04 3.575009D-07 -7.215374D-11 0.0D0 [g/cm sec]

**[CH<sub>4</sub> Mixture Molecular Diffusivity]**

$$[D_{CH_4} = a + b \cdot T + c \cdot T^{**2} + d \cdot T^{**-2}]$$

{a, b, c, d, units}

'EQUATION'

1.22169D-01 1.112172D-03 8.020364D-07 0.0D0 [cm<sup>2</sup>/sec]

**[HCl Mixture Molecular Diffusivity]**

$$[D_{HCl} = a + b \cdot T + c \cdot T^{**2} + d \cdot T^{**-2}]$$

{a, b, c, d, units}

'EQUATION'

9.4709D-02 9.359042D-04 6.920934D-07 0.0D0 [cm<sup>2</sup>/sec]

**[SiC Information]**

'BETA-SiC'

40.0965D0 [Molecular Weight, g/mol]  
 1.0D0 [Stoichiometric Coefficient]  
 3.21D0 0.0D0 [Density, g/cm<sup>3</sup>]  
 3.0D0 [HCl Stoichiometric Coefficient]

**[SiC Deposition Rate Parameters]**

{Species 1}

{k<sub>10</sub> [mol/cm<sup>2</sup> sec], E<sub>a1</sub> [kJ/mol], k<sub>r0</sub> [Dimensionless], E<sub>a2</sub> [kJ/mol]}

{Species 2}

'MTS'

5.26D-3 1.027D2 0.0D0 3.6D-5 -1.686D2 1.0D0 reaction rate

'HCl'

## APPENDIX D SAMPLE CALCULATIONS

This appendix contains sample calculations of the tube preform volume, fiber volume, and theoretical density. The calculation of the preform volume involves postinfiltration OD and ID, for these can change during infiltration due to SIC overcoat deposition. Other important calculations in this research are presented, including the required liquid MTS feed rate and the total molar flux input to the model. These sample calculations shall help the interested reader understand the experimental and model results presented in this dissertation.

### Tube Preform Volume

The determination of the tube preform volume requires the knowledge of the postinfiltration OD and ID (Equation D-1). Both diameters are averaged over several measurements taken along the tube length. A sample calculation of the tube preform volume is presented below with sample representative OD, ID, and preform length.

$$V_{\text{Preform}} = \Pi \left[ \left( \frac{\text{OD}_{\text{Average}}}{2} \right)^2 - \left( \frac{\text{ID}_{\text{Average}}}{2} \right)^2 \right] L_{\text{Preform}} \quad (\text{D} - 1)$$

$$V_{\text{Preform}} = \Pi \left[ \left( \frac{6.47 \text{ cm}}{2} \right)^2 - \left( \frac{4.95 \text{ cm}}{2} \right)^2 \right] (30.48 \text{ cm}) = 415.54 \text{ cm}^3$$

where ID = 4.95 cm L<sub>Preform</sub> = 30.48 cm  
OD = 6.47 cm

### Tube Preform Fiber Volume

The determination of the tube preform fiber volume involves the preform mass, preform volume, and fiber density (Equation D-2). A sample calculation of the tube preform fiber volume is presented below with representative preform mass, preform volume, and fiber density.

$$\text{Fiber Volume} = \frac{M_{\text{Preform}}}{\rho_{\text{Fiber}} V_{\text{Preform}}} \cdot 100\% \quad (\text{D} - 2)$$

$$\text{Fiber Volume} = \frac{385.72 \text{ g}}{(2.7 \frac{\text{g}}{\text{cm}^3})(415.54 \text{ cm}^3)} \cdot 100\% = 34.4\%$$

where M<sub>Preform</sub> = 385.72 g  
ρ<sub>Nextel™312</sub> = 2.7 g/cm<sup>3</sup>  
V<sub>Preform</sub> = 415.54 cm<sup>3</sup>

### Tube Theoretical Density

The determination of the tube theoretical density involves the knowledge of the preform mass, composite mass, densities of both fiber and matrix, and the preform volume (Equation D-3). The value for the preform mass is adjusted due to postinfiltration end removal. The final preform mass is figured from the pre-infiltration preform mass assuming a constant mass per unit length. A sample calculation of the tube theoretical density is provided below with representative

preform and composite mass, preform volume, and densities of the Nextel™ 312 fiber and SiC matrix.

$$\text{Theoretical Density} = \frac{V_{\text{Fiber}} + V_{\text{Matrix}}}{V_{\text{Preform}}} = \frac{\frac{M_{\text{Preform}}}{\rho_{\text{Fiber}}} + \frac{(M_{\text{Composite}} - M_{\text{Preform}})}{\rho_{\text{Matrix}}}}{V_{\text{Preform}}} \cdot 100\% \quad (\text{D-3})$$

$$\text{Theoretical Density} = \frac{\frac{385.72 \text{ g}}{2.7 \frac{\text{g}}{\text{cm}^3}} + \frac{(994.62 \text{ g} - 385.72 \text{ g})}{3.21 \frac{\text{g}}{\text{cm}^3}}}{415.54 \text{ cm}^3} \cdot 100\% = 80.0\%$$

where

$$\begin{aligned} M_{\text{Preform}} &= 385.72 \text{ g} \\ M_{\text{Composite}} &= 994.62 \text{ g} \\ \rho_{\text{Nextel}^{\text{TM}} 312} &= 2.7 \text{ g/cm}^3 \\ \rho_{\text{SiC}} &= 3.21 \text{ g/cm}^3 \\ V_{\text{Preform}} &= 415.54 \text{ cm}^3 \end{aligned}$$

### Desired Liquid MTS Feed Rate

The determination of the liquid MTS feed rate,  $F_{\text{MTS}}$ , is necessary to maintain a constant MTS flow rate and a constant hydrogen/MTS feed ratio,  $\alpha$ , during the tube infiltration. For a MTS molar flow of 1 slm, a liquid MTS feed rate of 6.7 g/min is necessary. The calculation involves the total flow rate and  $\alpha$  (Equation D-4).

$$F_{\text{MTS}} = \frac{1}{1 + \alpha} \frac{F_{\text{Total}} P}{R T} MW_{\text{MTS}} \quad (\text{D-4})$$

$$F_{MTS} = \frac{1}{1 + 4.98} \cdot \frac{(6 \text{ slm}) \left( \frac{1000.028 \text{ cm}^3}{\text{l}} \right) (1 \text{ atm})}{\left( \frac{82.05 \text{ cm}^3 \text{ atm}}{\text{mol K}} \right) (273 \text{ K})} \cdot \frac{149.5 \text{ g}}{\text{mol}} = 6.7 \frac{\text{g}}{\text{min}}$$

where

$F_{\text{Total}} = 6 \text{ slm}$	$P = 1 \text{ atm}$
$\alpha = 4.98$	$T = 273 \text{ K}$
$R = 82.05 \text{ cm}^3 \text{ atm/mol K}$	$MW_{\text{MTS}} = 149.5 \text{ g/mol}$

### Total Molar Flux Calculation for Model Input

The calculation of the total molar flux was necessary for the GTCVI model solution. However, the molar flux value that is supplied as a boundary condition to the model must include the injector cross-section area defined in the model input (Equation D-5) and not the injector cross-section area used in experiment.

$$N = \frac{F_{\text{Total}} P}{R T} \cdot \frac{1}{A_{\text{CS}}} \quad (\text{D-5})$$

$$N = \frac{(6 \text{ slm}) \left( \frac{1000.028 \text{ cm}^3}{\text{l}} \right) \left( \frac{\text{min}}{60 \text{ sec}} \right) (1 \text{ atm})}{\left( \frac{82.05 \text{ cm}^3 \text{ atm}}{\text{mol K}} \right) (273 \text{ K})} \cdot \frac{1}{(2.74 \text{ cm}^2)} = 1.63 \cdot 10^{-3} \frac{\text{mol}}{\text{cm}^2 \text{ sec}}$$

where

$F_{\text{Total}} = 6 \text{ slm}$	$P = 1 \text{ atm}$
$\alpha = 4.98$	$T = 273 \text{ K}$
$A_{\text{CS}} = 2.74 \text{ cm}^2$	

## APPENDIX E PERMEABILITY CALCULATION

This appendix contains the Nextel™312/SiC composite specimen pressure-drop and flow rate data needed for the determination of the permeability. The permeability is found by taking the least-squares fit to the data. The experimental data, regression analysis, specimen thickness, and room-temperature nitrogen viscosity are displayed in a Microsoft™ Excel98 spreadsheet (Richmond, WA) seen in Figure E-1. The permeability value is found in the slope, where the specimen thickness and the room temperature-viscosity of the nitrogen are needed to calculate the permeability from the slope value (Equation E-1).

$$F = - \left\{ \frac{\beta A_{CS}}{\mu \tau_{Specimen}} \right\} \Delta P \quad (E - 1)$$

Where

$\beta$  = specimen permeability [ $\text{cm}^2$ ; (Darcies)]

$F$  = gas flow rate [sccm]

$A_{CS}$  = specimen cross-section [ $\text{cm}^2$ ]

$\mu$  = gas viscosity [g/cm sec]

$\tau_{Specimen}$  = specimen thickness [cm]

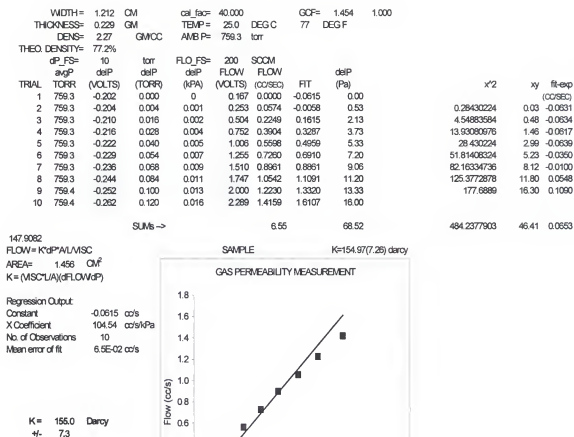
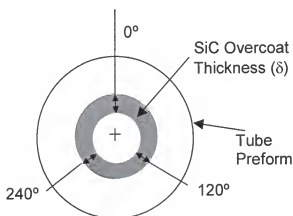


Figure E-1. Microsoft™ Excel98 spreadsheet used to determine the specimen permeability from least-squares regression analysis of the pressure drop and flow rate data.

## APPENDIX F SILICON CARBIDE OVERCOAT MASS CALCULATION

This appendix contains the method used to estimate the SiC overcoat mass on the tube interior after infiltration. The average overcoat mass was determined from analysis of X-ray tomographic images at seven different axial positions along the tube length. The average overcoat thickness,  $\delta$ , for each image was taken from measurements at 0°, 120°, and 240° with 0° located at the 12 o'clock position (Equation F-1). The average SiC overcoat thickness calculated for each of the seven images was used to calculate the estimated overcoat volume. A diagram depicting the circumferential positions used in the overcoat measurement is seen in Figure F-1.



$$\delta_{OC}^{Avg} = \frac{\delta_{OC}^{0^\circ} + \delta_{OC}^{120^\circ} + \delta_{OC}^{240^\circ}}{3} \quad (F - 1)$$

Figure F-1. Diagram demonstrating circumferential positions where the SiC overcoat is measured for each X-ray tomographic image.



The SiC overcoat volume estimate involves a sequence of volume segment calculations. Two adjacent SiC overcoat thickness measurements,  $\delta_i$  and  $\delta_{i+1}$ , are used in the calculation of each volume segment. The calculation of the volume segment is simply the difference between the convoluted volume using the tube preform inside radius (assuming no overcoat) and the convoluted volume of the tube interior gas space (Equation F-2). The overcoat thickness is assumed linear within an overcoat volume segment (Equation F-3). The equation used to calculate the overcoat volume segment in final form is shown in Equation F-4. A diagram of an individual overcoat volume segment and the corresponding series of volume segments that comprise the total overcoat volume are seen in Figure F-2.

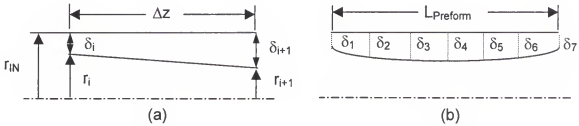


Figure F-2. Diagrams of the SiC overcoat volumes.  
a) volume segment; b) series of measured SiC overcoat thicknesses used to calculate the total overcoat volume.

$$V_{OC}^{Segment} = \Pi r_{IN}^2 \Delta z - \iiint r(z) dr d\theta \cdot dz \quad (F - 2)$$

$$r(z) = r_{IN} - \delta(z) \quad (F - 3)$$

$$V_{OC}^{Segment} = \Pi \Delta z \left[ 2r_{IN} \delta_i + r_{IN} (\Delta \delta) - \frac{(\Delta \delta)^2}{3} - \delta_i (\Delta \delta) - \delta_i^2 \right] \quad (F - 4)$$

The SiC overcoat volume is calculated from the summation of all six volume segments defined by the seven measured SiC overcoat thicknesses. Sample calculations of the average SiC overcoat thickness, SiC overcoat volume segment, and total SiC overcoat volume are shown in Equations F-5 through F-7.

### Average SiC Overcoat Thickness

$$\delta_{OC}^{Average} = \frac{25.4 \mu\text{m} + 28.4 \mu\text{m} + 26.7 \mu\text{m}}{3} = 26.8 \mu\text{m} \quad (\text{F} - 5)$$

where  $\delta_{0^\circ} = 25.4 \mu\text{m}$   $\delta_{120^\circ} = 28.4 \mu\text{m}$   
 $\delta_{240^\circ} = 26.7 \mu\text{m}$

### SiC Overcoat Volume Segment

$$V_{OC}^{Segment} = (3.14)(5 \text{ cm})[2(2.54 \text{ cm})(26.8 \cdot 10^{-4} \text{ cm}) + (2.54 \text{ cm})(10.1 \cdot 10^{-4} \text{ cm}) \\ - \frac{(10.1 \cdot 10^{-4} \text{ cm})^2}{3} - (26.8 \cdot 10^{-4} \text{ cm})(10.1 \cdot 10^{-4} \text{ cm}) - (26.8 \cdot 10^{-4} \text{ cm})^2]$$

$$V_{OC}^{Segment} = 0.254 \text{ cm}^3 \quad (\text{F} - 6)$$

where  $\Delta Z = 5 \text{ cm}$   $\delta_i = 26.8 \mu\text{m}$   
 $r_{IN} = 2.54 \text{ cm}$   $\Delta\delta = 10.1 \mu\text{m}$

### Total SiC Overcoat Volume

$$V_{OC} = (0.254 \text{ cm}) + (1.456 \text{ cm}) + (5.423 \text{ cm}) + (4.968 \text{ cm}) + (1.776 \text{ cm}) + (0.451 \text{ cm})$$

$$V_{OC} = 14.328 \text{ cm} \quad (\text{F} - 7)$$

## APPENDIX G X-RAY COMPUTED TOMOGRAPHY IMAGES

This appendix contains the X-ray computed tomography (CT) images (Figures G-2-6) of the density standards used for system calibration (unfiltered Nextel™312 tube preform and dense Nextel™312/SIC composite specimens) and the tomographic images of tubes CVI 1211, CVI 1223, CVI 1217, and CVI 1218. The linear grayscale/density relationship constructed from the density standards (Table 6-5) was used to define the density for each discretized radial volume element in each of the tomographic images (1 mm thickness; values taken at 0°, 60°, 120°, and 180°).

For each tube, X-ray scans were taken at seven equidistant axial positions (5 cm) (Figure G-1). The axial position presented with each tomographic image is measured from the tube preform inlet end.

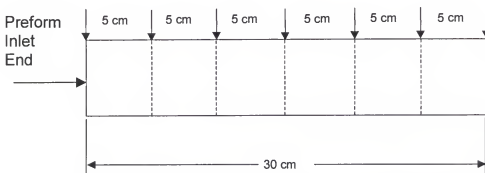
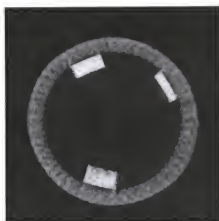


Figure G-1. Diagram of the tube preform indicating the axial positions where the X-ray tomographic images were taken.

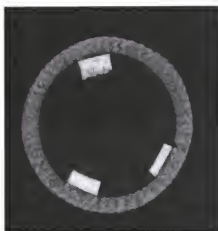
X-Ray Computed Tomography Density Standards  
Nextel™312 Tube Preform and Dense Nextel™312/SiC Composite Specimens  
[40% Theoretical Density and 85% Theoretical Density]



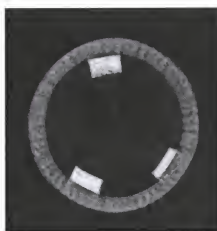
(a)



(b)



(c)



(d)

Figure G-2. X-ray computed tomographic images for the Nextel™ 312 tube preform and the dense Nextel™ 312/SiC composite specimens.

a) 0 cm; b) 5 cm; c) 10 cm; d) 15 cm; e) 20 cm; f) 25 cm; g) 30 cm.



(e)



(f)



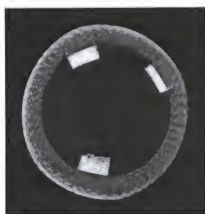
(g)

Figure G-2--continued

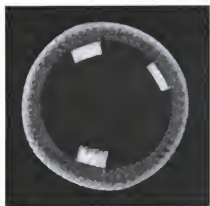
CVI 1211  
Six Hours Infiltration  
[40% Theoretical Density]



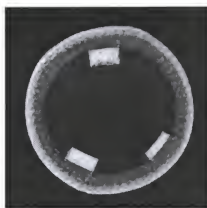
(a)



(b)

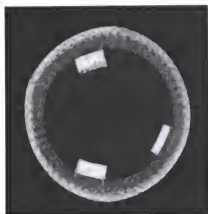


(c)

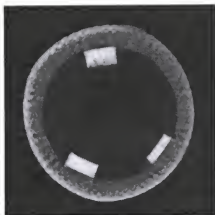


(d)

Figure 6-3. X-ray computed tomographic images for tube CVI 1211.  
a) 0 cm; b) 5 cm; c) 10 cm; d) 15 cm; e) 20 cm; f) 25 cm; g) 30 cm.



(e)



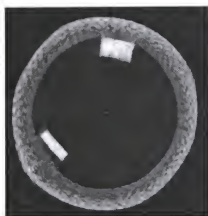
(f)



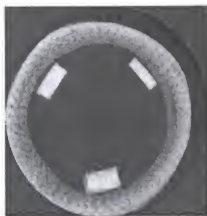
(g)

Figure G-3--continued

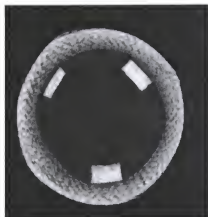
CVI 1223  
12 Hours Infiltration  
[54% Theoretical Density]



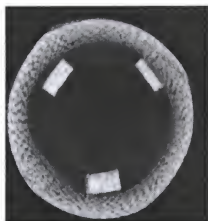
(a)



(b)



(c)



(d)

Figure 6-4. X-ray computed tomographic images for tube CVI 1223.

a) 0 cm; b) 5 cm; c) 10 cm; d) 15 cm; e) 20 cm; f) 25 cm; g) 30 cm.





(e)



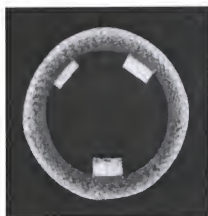
(f)



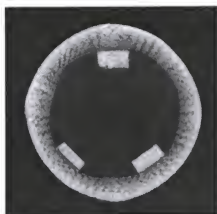
(g)

Figure G-4--continued

CVI 1217  
24 Hours Infiltration  
[70% Theoretical Density]



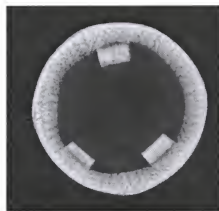
(a)



(b)



(c)

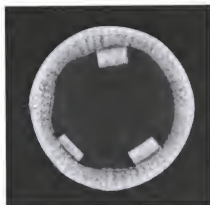


(d)

Figure 6-5. X-ray computed tomographic images for tube CVI 1217.  
a) 0 cm; b) 5 cm; c) 10 cm; d) 15 cm; e) 20 cm; f) 25 cm; g) 30 cm.



(e)



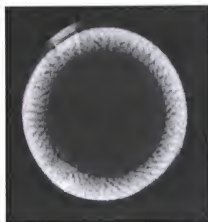
(f)



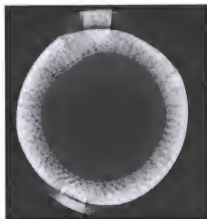
(g)

Figure G-5--continued

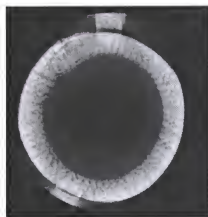
CVI 1218  
32 Hours Infiltration  
[80% Theoretical Density]



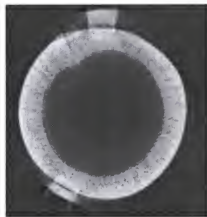
(a)



(b)



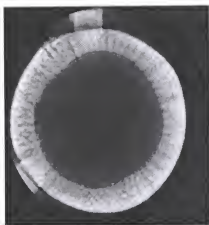
(c)



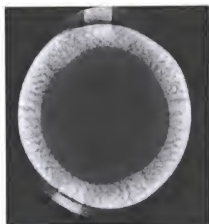
(d)

Figure G-6. X-ray computed tomographic images for tube CVI 1218.

a) 0 cm; b) 5 cm; c) 10 cm; d) 15 cm; e) 20 cm; f) 25 cm; g) 30 cm.



(e)



(f)



(g)

Figure G-6--continued

## APPENDIX H DIGITAL IMAGES

This appendix contains several digital images taken from tubes CVI 1217 and CVI 1218 (24 and 32 hours infiltration) (Figures H-2-3). For each tube, digital images taken from two distinct composite thickness positions at three different tube axial positions are provided along with an overall digital image taken at the middle of the tube length ( $0^\circ$ ). The positions used in the digital images are demonstrated in Figure H-1. The axial positions used in the digital image analysis coincide with those used in the X-ray computed tomography (Appendix G).

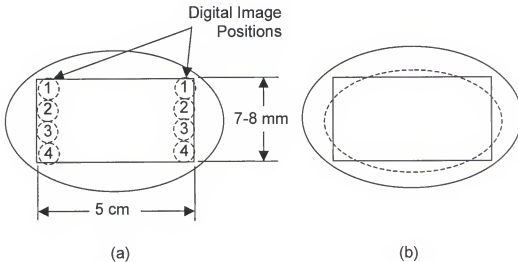
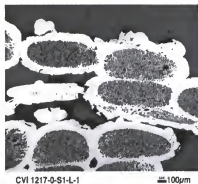


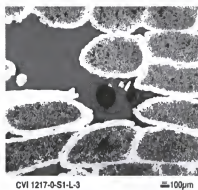
Figure H-1. Digital image locations.

(a) Digital image positions used for the tube fiber volume and theoretical density arrays; (b) Specimen range used for the overall digital images.

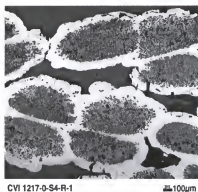
CVI 1217  
24 Hours Infiltration  
[70% Theoretical Density]



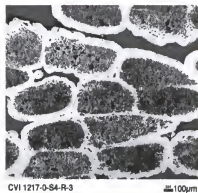
(a)



(b)



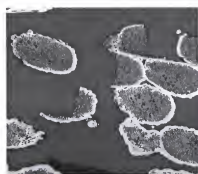
(c)



(d)

Figure H-2. Digital images taken from tube CVI 1217.

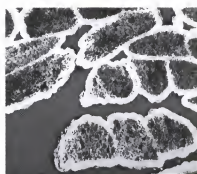
a) 0 cm; Position 1; b) 0 cm; Position 3; c) 20 cm; Position 1; d) 20 cm; Position 3; e) 30 cm; Position 1; f) 30 cm; Position 3; g) Overall digital image taken from CVI 1217.



CVI 1217-Q-S6-R-1

100μm

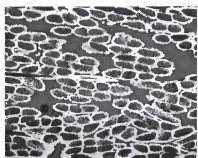
(e)



CVI 1217-Q-S6-R-3

100μm

(f)



CVI 1217-Q-S3-C-OA

300μm

(g)

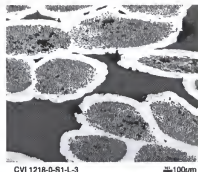
Figure H-2--continued



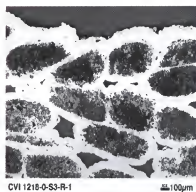
CVI 1218  
32 Hours Infiltration  
[80% Theoretical Density]



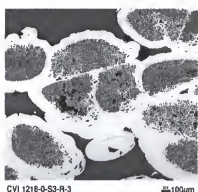
(a)



(b)



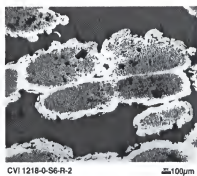
(c)



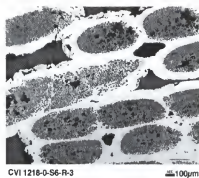
(d)

Figure H-3. Digital images taken from tube CVI 1218.

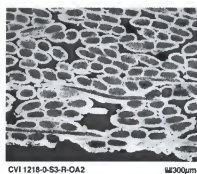
a) 0 cm; Position 1; b) 0 cm; Position 3; c) 20 cm; Position 1; d) 20 cm; Position 3; e) 30 cm; Position 2; f) 30 cm; Position 3; g) Overall digital image taken from CVI 1218.



(e)



(f)



(g)

Figure H-3—continued

## REFERENCES

- Allendorf, M., Osterheld, T., & Melius, C., SAND94-8524, U.S. DOE (1994).
- Avrami, M., J. Chem. Phys., **8**, 212 (1940).
- Barin, I., Thermochemical Data of Pure Substances, American Chemical Society, New York (1989).
- Beatty, R., & Kiplinger, D., Nucl. Appl. Tech., **8**, 488 (1970).
- Besmann, T., Sheldon, B., Moss III, T., & Kaster, M., J. Amer. Cer. Soc., **75** [10], 2899 (1991).
- Bhatia, S., & Perlmutter, D., J. AIChE, **26** [3], 379 (1980).
- Bickerdike, R., Brown, A., Hughes, G., & Ranson, H., Proc. 5<sup>th</sup> Conf. On Carbon, Ed. Mrozowski, S., Studabaker, M., & Walker, P., Pergamon Press, New York, 575 (1962).
- Bird, R., Stewart, W., & Lightfoot, E., Transport Phenomena, John Wiley & Sons, New York (1960).
- Brennfleck, K., Fitzer, E., Schoch, G., & Dietrich, M., Proc. 9<sup>th</sup> Int. Conf. CVD, Ed. Robinson, McD., The Electrochemical Society, Pennington, NJ, 649 (1984).
- Burgess, J., & Lewis, T., Chem and Ind., **19**, 76 (1974).
- Campbell, I. & Sherwood, E., High-Temperature Materials and Technology, John Wiley and Sons, New York (1967).
- Caputo, A., & Lackey, J., Ceram. Eng. Sci. Proc., **5**, 654 (1984).
- Carman, P., Flow of Gases Through Porous Media, Academic Press, New York (1956).

- Carter, R., 24<sup>th</sup> Annual American Ceramic Society Cocoa Beach Conference on Engineering Ceramics and Structures, American Ceramic Society, Cocoa Beach, FL (2000).
- Chase, M., JANAF Thermochemical Tables, 3<sup>rd</sup> Ed., American Chemical Society, New York (1986).
- Chiang, D., Ph.D. Thesis, Georgia Institute of Technology, Atlanta, GA (1999).
- Chung, G., & McCoy, B., J. Amer. Cer. Soc., **74** [4], 746 (1991).
- Currier, R., J. Amer. Cer. Soc., **73** [8], 2274 (1990).
- Coblentz, W., "Firing and Sintering", Engineered Materials Handbook: Ceramics and Glasses, Ed. Schneider, S., ASM Int., Materials Park, OH, **4**, 242 (1991).
- Darcy, H., Les Fontaines Publiques de la Ville de Dijon, Victor Dalmont, Paris (1856).
- Descamps, C., & Vignoles, G., Electrochem. Soc. Proc., **97** [25], 520 (1996).
- Ellingson, W., & Vannier, M., ANL-87-52, U.S. DOE (1988).
- Ezis, A., "Hot Pressing", Engineered Materials Handbook: Ceramics and Glasses, Ed. Scheider, S., ASM Int., Materials Park, OH, **4**, 186 (1991).
- Fischman, G., & Petuskey, W., J. Amer. Cer. Soc., **68** [4], 185 (1985).
- Fitzer, E., & Gadow, R., Amer. Cer. Soc. Bull., **65** [2], 326 (1986).
- Golecki, I., Electrochem. Soc. Proc., **97** [25], 568 (1996).
- Griffiths, S., & Nilson, R., J. Electrochem. Soc., **145** [4], 1263 (1998).
- Gupte, S., & Tsamopolous, J., J. Electrochem. Soc., **137** [5], 1626 (1990).
- Gupta, D., & Evans, J., J. Mater. Res., **6** [4], 810 (1991).
- Interrante, L., Whitmarsh, C., & Sherwood, W., Ceram. Trans., **58**, 111 (1995).
- Iwamoto, N., in Silicon Carbide Ceramics-2: Gas Phase Reactions, Fibers and Whiskers, and Joining, Ed. Somiya, S., & Inomata, Y., Elsevier, New York, 279 (1991).
- Hillig, W., in Fiber Reinforced Ceramic Composites, Ed. Mazdiasni, K., Noyes Publications, Park Ridge, NJ, Ch. 9, 260 (1974).

- Hopfe, V., Mosebach, H., Erhard, M., & Meyer, M., J. Mol. Struct., **347**, 331 (1995).
- Jennings, W., First Course in Numerical Methods, Macmillan, New York (1964).
- Josiek, A., & Langlais, F., J. Cryst. Growth, **160**, 253 (1996).
- Kington, A., Lutz, L., Liaw, P., & Davis, R., J. Amer. Cer. Soc., **66** [1], 558 (1983).
- Klemens, P., Int. J. Thermophys., **11**, 971 (1990).
- Kotlensky, W., in Chemistry and Physics of Carbon, Ed. Walker Jr., P. & Thrower, P., Marcel Dekker, New York, **9**, 173 (1973).
- Lackey, J., in Fiber Reinforced Ceramic Composites, Ed. Mazdiasni, K., Noyes Publications, Park Ridge, NJ, Ch. 14, 440 (1990).
- Lackey, J., Vaidyaraman, S., Beckloff, B., Moss III, T., & Lewis, J., J. Mat. Res., **13** [8], 2251 (1998).
- Lauten, F., 22<sup>nd</sup> Annual American Ceramic Society Cocoa Beach Conference on Engineering Ceramics and Structures, American Ceramic Society, Cocoa Beach, FL (1998).
- Lowden, R., Caputo, A., Stinton, D., Besmann, T., & Morris, M., ORNL/TM-10403, U.S. DOE (1987).
- Mason, E., & Malinauskas, A., Gas Transport in Porous Media: The Dusty Gas Model, Elsevier, New York (1983).
- Matlin, W., M.S. Thesis, University of Tennessee, Knoxville, TN (1995).
- Melkote, R., & Jensen, K., J. AIChE, **35**, 12 (1989).
- Midha, V., & Economou, D., J. Electrochem. Soc., **144** [11], 4062 (1997).
- Mühlratzer, A., Agatonovic, P., Köberle, H., & Wildenrotter, K., Ind. Cer., **16** [2], 507 (1996).
- Naslain, R., Rossingnol, J., Hagenmuller, P., Heraud, L., & Choury, J., Rev. Chimie Minérale, **18**, 544 (1981).
- Naslain, R., in High Temperature Ceramic Matrix Composites III, CSJ Ser., 3, Ed. Niihara, K., Nakano, K., Sekino, T., & Yasuda, E., Ceramic Society of Japan, Tokyo, **3** (1999).

- Ofori, J., & Sotirchos, S., J. Mater. Res., **11** [10], 2541 (1996).
- Ofori, J. & Sotirchos, S., J. Electrochem. Soc., **144** [1], 274 (1997).
- Ohzawa, Y., Sadanaka, A., & Sugiyama, K., Electrochem. Soc. Proc., **97** [25], 552 (1996).
- Papasouliotis, G., & Sotirchos, S., J. Electrochem. Soc., **145** [11], 3908 (1998).
- Patankar, S., Numerical Heat Transfer and Fluid Flow, Hemisphere, New York (1980).
- Perrins, W., McKenzie, D., & McPhedran, R., Proc. R. Soc. Lond. A., **369**, 207 (1979).
- Proceedings of the 12<sup>th</sup> Annual Conference on Fossil Energy Materials, United States Department of Energy, Office of Fossil Energy, Knoxville, TN, (1998).
- Reid, R., Prausnitz, J., & Sherwood, T., The Properties of Liquids and Gases, 3<sup>rd</sup> Ed., McGraw-Hill, New York (1977).
- Roman, Y., Ph.D. Thesis, Delft University, The Netherlands (1995).
- Rossingol, J., Langlais, F., & Naslain, R., Proc. 9<sup>th</sup> Int. Conf. CVD, Cincinnati, Ed. Robinson, McD., The Electrochemical Society, Pennington, NJ, 596 (1984).
- Rudolph, J., Purdy, M., & Bok, L., U.S. Patent No. 5,480,678 (1996).
- Satterfield, C., Sherwood, C., & Kilgore, T., The Role of Diffusion in Catalysis, Addison-Wesley, Reading, Mass (1963).
- Schlichting, J., Powd. Metal Int., **12** [3,4], 171, 196 (1980).
- Sheldon, B., & Besmann, T., J. Amer. Cer. Soc., **73** [9], 3046 (1990).
- Skamser, D., Jennings, H., & Johnson, D., J. Mater. Res., **12** [3], 724 (1997).
- Sotrichos, S., & Burganos, V., J. AIChE., **34** [7], 1106 (1988).
- Sotirchos, S., AIChE J., **37** [9], 1365 (1991).
- Sotrichos, S., & Zarkanitis, S., Chem. Eng. Sci., **48** [8], 1487 (1993).
- Starr, T., Ceram. Eng. Sci. Proc., **9** [7-8], 803 (1988).

- Starr, T., Mat. Res. Soc. Proc., **250**, 202 (1991).
- Stauffer, D., & Aharony, A., Introduction to Percolation Theory, Taylor and Francis, Washington, D.C. (1992).
- Starr, T., & Smith, A., Modeling of Forced-Flow/Thermal Gradient Chemical Vapor Infiltration, ORNL/sub/85-55901/03, U.S. DOE (1992).
- Starr, T., Smith, A., Besmann, T., McLaughlin, J., and Sheldon, B., "Modeling of Chemical Vapor Infiltration for Composite Fabrication", in High Temperature Ceramic Matrix Composites, Ed. Naslain, R., European Association for Composite Materials, Bordeaux, France (1993).
- Starr, T., J. Mat. Res., **10** [9], 2360 (1995).
- Starr, T., & Smith, A., A Finite-Volume Model for Chemical Vapor Infiltration Incorporating Radiant Heat Transfer, ORNL/Sub/85-55901/05, U.S. DOE (1995b).
- Starr, T., & Hablutzel, N., J. Amer. Cer. Soc., **81** [5], 1298 (1998).
- Stinton, D., Caputo, A., & Lowden, R., Amer. Cer. Soc. Bull., **65** [2], 347 (1986).
- Stinton, D., Lowden, R., & Besmann, T., "Fiber-Reinforced Composites for Gas Turbine Applications", Int. Gas Turb. and Aeroeng. Cong. and Expo., Cologne, Germany (1992).
- Streckert, H., Norton, K., & Wong, C., Amer. Cer. Soc. Bull., **75** [12], 61 (1996).
- Tai, N., & Chou, T., J. Amer. Cer. Soc., **72** [3], 414 (1989).
- Tai, N., & Chou, T., in Metal & Ceramic Matrix Composites: Processing, Modeling, and Mechanical Behavior, Ed. Bhagat, R., Clauer, A., Kumar, P., & Ritter, A., The Minerals, Metals, and Materials Society, Warrendale, PA, 303 (1990).
- Tawil, H., Bentsen, L., Baskaran, S., & Hasselman, D., J. Mater. Sci., **20**, 3201 (1985).
- Tomadakis, M., & Sotirchos, S., J. Chem. Phys., **98** [1], 616 (1993).
- Tomadakis, M., & Sotirchos, S., J. AIChE, **39**, 397 (1993).
- Tsai, D., & Streider, W., Chem. Eng. Comm., **40**, 207 (1986).
- Vaidyaraman, S., Lackey, J., Agrawal, P., & Miller, M., Carbon, **34**, 347 (1996).

Van Kemenade, A., & Stemfoort, C., J. Cryst. Grow., **12**, 13 (1972).

Wang, H., Dinwiddie, R., & Gaal, P., "Multiple Station Thermal Diffusivity Instrument", Thermal Conductivity **23**, 119, Ann Arbor, MI (1996).

Weast, R., CRC Handbook of Chemistry and Physics, 76<sup>th</sup> Ed., CRC Press, Boca Raton, FL (1995).

Xu, Y., & Zhang, L., J. Amer. Cer. Soc., **80** [7], 1897 (1997).



## BIOGRAPHICAL SKETCH

Kent Joseph Probst was born on August 7, 1972, in Port Allegany, Pennsylvania, to William and Sandra Probst. At the age of four, Kent and his family moved to Mercer, Pennsylvania. Kent lived in Mercer until completion of high school. During high school, Kent was active in track and field competing in district, state, regional, and national championships in the discus throw. Kent also had a keen interest in mathematics and the physical sciences. In his senior year, Kent was awarded the John S. Patterson Award, which was given to the top math student, and was awarded the United States Army Scholar/Athlete Award, which was given to the student with the most accomplished success in academics and athletics. Kent was also inducted into the National Honor Society in 1989. In June 1990, Kent graduated third in his class at Mercer Junior-Senior High School.

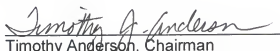
In the fall of 1990, Kent attended the Pennsylvania State University and received a B.S. in Chemical Engineering in May 1994. During his four years at Penn State, Kent worked in the Engineering Library as a library assistant. During his sophomore year, he was an intramural champion in football. At Penn State, Kent was recognized and inducted into both the Tau Beta Pi National Engineering Honor Society and the Omega Chi Epsilon National Chemical Engineering Honor Society. During his senior year at Penn State, he was

elected president of the Omega Chi Epsilon chapter by his classmates and was nominated for president of the Tau Beta Pi chapter this same year.


Kent attended to the University of Florida in August 1994 to pursue a doctoral degree in chemical engineering. He was invited to conduct his doctoral research at Oak Ridge National Laboratory in Tennessee after passing his written doctoral qualifying exams. Kent spent three years at Oak Ridge conducting research in the processing, process modeling, and characterization of fiber-reinforced ceramic composite tubes. During his time at Oak Ridge, he was invited to present his work at annual conferences of the American Ceramic Society and the United States Department of Energy, Office of Fossil Energy.

At the age of ten, Kent acquired juvenile onset-diabetes. He has managed to maintain good health for the past seventeen years. During his time in high school, he managed to have perfect attendance his last three years despite the disease.


I certify that I have read this study and that in my opinion it conforms to acceptable standards of scholarly presentation and is fully adequate, in scope and quality, as a dissertation for the degree of Doctor of Philosophy.

  
Timothy Anderson, Chairman  
Professor of Chemical Engineering

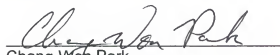
I certify that I have read this study and that in my opinion it conforms to acceptable standards of scholarly presentation and is fully adequate, in scope and quality, as a dissertation for the degree of Doctor of Philosophy.

  
Theodore Besmann  
Head, Surface Processing and  
Mechanics Group  
Metals and Ceramics Division  
Oak Ridge National Laboratory

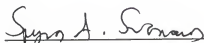
I certify that I have read this study and that in my opinion it conforms to acceptable standards of scholarly presentation and is fully adequate, in scope and quality, as a dissertation for the degree of Doctor of Philosophy.

  
Paul Holloway  
Ellis D. Verink Professor of Materials  
Science and Engineering

I certify that I have read this study and that in my opinion it conforms to acceptable standards of scholarly presentation and is fully adequate, in scope and quality, as a dissertation for the degree of Doctor of Philosophy.

  
Chang-Won Park  
Associate Professor of Chemical  
Engineering

I certify that I have read this study and that in my opinion it conforms to acceptable standards of scholarly presentation and is fully adequate, in scope and quality, as a dissertation for the degree of Doctor of Philosophy.



Spyros Svoronos  
Professor of Chemical Engineering

I certify that I have read this study and that in my opinion it conforms to acceptable standards of scholarly presentation and is fully adequate, in scope and quality, as a dissertation for the degree of Doctor of Philosophy.



Loc Vu-Quoc  
Professor of Aerospace Engineering,  
Mechanics, and Engineering Science

This dissertation was submitted to the Graduate Faculty of the College of Engineering and to the Graduate School and was accepted as partial fulfillment of the requirements for the degree of Doctor of Philosophy.



M. J. Ohanian  
Dean, College of Engineering

May 2000

Winfred M. Phillips  
Dean, Graduate School